NTNU
Norwegian University of
Science and Technology

Master's thesis
2021
Petter Kjønstad Skjesol

Master's thesis

NTNU
Norwegian University of
Science and Technology
Faculty of Natural Sciences
Department of Physics

Petter Kjønstad Skjesol

Active Turbulence of Self-Propelled Particles with Hydrodynamic Interactions

June 2021

NTNU
Norwegian University of
Science and Technology

NTNU
Norwegian University of
Science and Technology

Active Turbulence of Self-Propelled Particles with Hydrodynamic Interactions

Petter Kjønstad Skjesol

Applied Physics
Submission date: June 2021
Supervisor: Paul Gunnar Dommersnes

Norwegian University of Science and Technology
Department of Physics

Abstract

In this thesis we present results from simulations of a 2-dimensional (2D) active system of polar, self-propelled particles with long-range hydrodynamic interactions. This models a system of swimming micro-organisms in a confined fluid, which is an example of active matter. In physics active matter is defined by systems where the constituents are able take some kind of energy from its environment and transform it into systematical movements and thus self-propel. In this thesis we are specifically interested in how turbulent-like behaviour in the collective motion, known as active turbulence, arises in such systems.

We invoke central concepts from inertial turbulence in fluids with high Reynolds numbers, like the $k^{-\beta}$ scaling of the energy spectrum from Kolmogorov theory, where $\beta = 5/3$. Active turbulence describes fundamentally different physics as it occurs at very low Reynolds number, and more importantly because energy is injected locally through the self-propulsion of the particles. As an example Alert et. al. (2020) show that the scaling exponent is $\beta = 1$ for active nematic fluids.

The hydrodynamic interactions between the particles are motivated by the flow field of the surrounding fluid induced by the self-propulsion of the particles. This takes a dipolar form in 2D and the particles reorientate with respect to the field induced by each other. A short-range particle alignment interaction is also introduced, and the system is simulated with periodic boundary conditions using hydrodynamic image dipoles. We emphasize that this model contains no noise, therefore the observed turbulent behaviour will be a result of deterministic chaos.

We present results from a system with given flow alignment coefficients and density. This system displays power law scaling of the energy spectrum with an exponent $\beta = 1.3$ on large scales. In addition it displays a non-Gaussian broadening of the probability density functions for the velocity increments, with an increasing broadening at shorter scales. Thirdly, there is a transition from a ballistic to a diffusive regime in the mean square displacement of the particles in this system. Thus, the system meets the standard criteria of inertial and active turbulence. To the author's knowledge active turbulence has not been demonstrated earlier in a microscopical model of polar swimmers with long-range hydrodynamic interactions. This can be a useful finding for the general understanding of active turbulence. Comparisons with systems with other parameters show that the scaling exponent of the energy spectra increases with density.

We conclude that active turbulence and scaling exponents β in this system results from the balance between the long-range dipolar flow interaction that creates hydrodynamic instabilities and breaks order in the system, and the short-range alignment interaction which favours order. At higher densities the latter becomes more dominant and generates coherent flocks on short scales, which in turn leads to amplified fluctuations on large scales.

Sammendrag

I denne avhandlingen presenter vi simuleringer av et 2-dimensjonelt (2D) aktivt system bestående av polare, selvdrevne partikler med langtrekkende hydrodynamiske vekselvirkninger. Dette er en modell for mikroorganismer som svømmer i et fluid hvor bevegelse i en tredje dimensjon er begrenset. Et slikt system er et eksempel på aktiv materie, som i fysikk er definert som systemer av partikler som tar energi fra omgivelsene og omdanner den til systematisk bevegelse og dermed beveger seg på egenhånd. I denne avhandlingen er vi spesielt interesserte i hvordan kollektiv, turbulentlignende oppførsel oppstår i slike systemer. Dette er kjent som aktiv turbulens.

Vi anvender sentrale konsepter fra studier av inertiell turbulens i fluider med høye Reynoldstall, som Kolmogorovs skaleringslov $k^{-\beta}$ for energispektra, hvor $\beta = 5/3$. Aktiv og inertiell turbulens beskriver fundamentalt forskjellig fysikk siden førstnevnte oppstår ved lave Reynoldstall, og enda viktigere fordi energi tilføres lokalt i aktive systemer som følge av at partiklene er selvdrevne. Eksempelvis viser Alert et. al. (2020) at i aktive nematiske fluider er skaleringseksponenten $\beta = 1$.

De hydrodynamiske vekselvirkningene er motivert gjennom at partiklenes svømming og egenbevegelse skaper et hastighetsfelt i fluidet de beveger seg i. I 2D tar dette feltet en dipolar form, og partiklene innretter seg etter hverandres induserte hastighetsfelt. Vi legger også til en kortrekkende ordningsvekselvirkning mellom partiklene. Systemet blir simulert med periodiske grensebetingelser ved bruk av hydrodynamiske speildipoler. Vi understreker at denne modellen er støyfri og dermed vil observert turbulent oppførsel være et resultat av deterministisk støy.

Vi presenterer resultater fra et system med gitte innrettingskoeffisienter og tetthet. I dette systemet finner vi at energispektrumet følger en skaleringslov med eksponenten $\beta = 1.3$ på stor skala. Vi observer også en ikke-Gaussisk utvidelse av sannsynlighetstetthetsfunksjonene for hastighetsforskjeller på liten skala. En tredje observasjon fra systemet er en overgang fra ballistisk til diffusiv oppførsel for det kvadratiske gjennomsnittet av partiklenes forflytning. Systemet oppfyller dermed tre standardkriterier for inertiell og aktiv turbulens. Forfatteren kjenner ikke til at aktiv turbulens tidligere har blitt demonstrert i en mikroskopisk modell for polare svømmere med langtrekkende hydrodynamiske vekselvirkninger, så dette kan være en nyttig observasjon i den generelle forståelsen av aktiv turbulens. Gjennom sammenligninger med systemer med andre parametre finner vi at spektra skalerer raskere med økt tetthet.

Vi konkluderer med at i dette systemet kommer aktiv turbulens og skaleringseksponenten β som et resultat av balansen mellom den langtrekkende dipolare innrettingsvekselvirkningen som skaper hydrodynamiske ustabiliteter og uorden i systemet, og den kortrekkende ordningsvekselvirkningen som ordner partiklene. Ved høyere tettheter blir sistnevnte mer dominant og skaper koherente flokker på liten skala, noe som igjen fører til forsterkede fluktuasjoner på stor skala.

Preface

This master thesis marks the end of my Master's degree in Applied Physics at the Norwegian University of Science and Technology. It is a direct continuation of my specialisation project *"Collective behaviour of confined self-propelled particles induced by hydrodynamic interactions"*, in which I studied the same system that will be presented here. The aim of this thesis was initially to further investigate the mechanisms behind a transition from order to disorder, which was observed during the specialisation project. However, during the course of the project increasingly more attention was drawn towards a turbulent-like behaviour of the system. The final aim was therefore to see whether active turbulence could be observed.

From my specialisation project I have reused parts of the introduction, the theory on the Vicsek model and hydrodynamic interactions and the simulation methods. However, all these sections are reviewed and contain new content in this report.

During the project much time has been devoted to writing effective code to run simulations and to analyse the resulting data. The simulation code has been written in C++, while data analysis has been performed in both C++ and Python. To speed up the computations, the code has been parallelized using OpenMP. The computations were performed on resources provided by the NTNU IDUN/EPIC computing cluster [1].

I would like to thank my supervisor Paul Gunnar Dommersnes for the opportunity to do this master thesis, and for his guidance, illuminating discussions and creative ideas. Without his commitment, this work would have been far less joyful.

I also want to thank my family for always supporting me and helping me believe in myself.

Finally, I want to thank my fellow students at NTNU for 5 incredible years which I will remember for the rest of my life.

Petter Kjønstad Skjesol
Trondheim
25.06.2021

Contents

List of Figures

1 Introduction

In nature we observe a rich variety of phenomena where animals, bacteria and non-living creatures behave in a collective manner. These ubiquitous collective behaviours occur on all scales, from organisms on the sub-cellular scale in the cytoplasm to large mammals [2]. In Figure 1 we see how flocks of birds, fish and sheep form patterns as a result of their collective behaviour. Typical behaviours are chaotic swirling, vortex formations, orientational order, formation of traffic lanes and more. Common for these phenomena is that they are systems of individuals who themselves move freely, but by mutual interactions form patterns on a large scale compared to the size of the individuals.

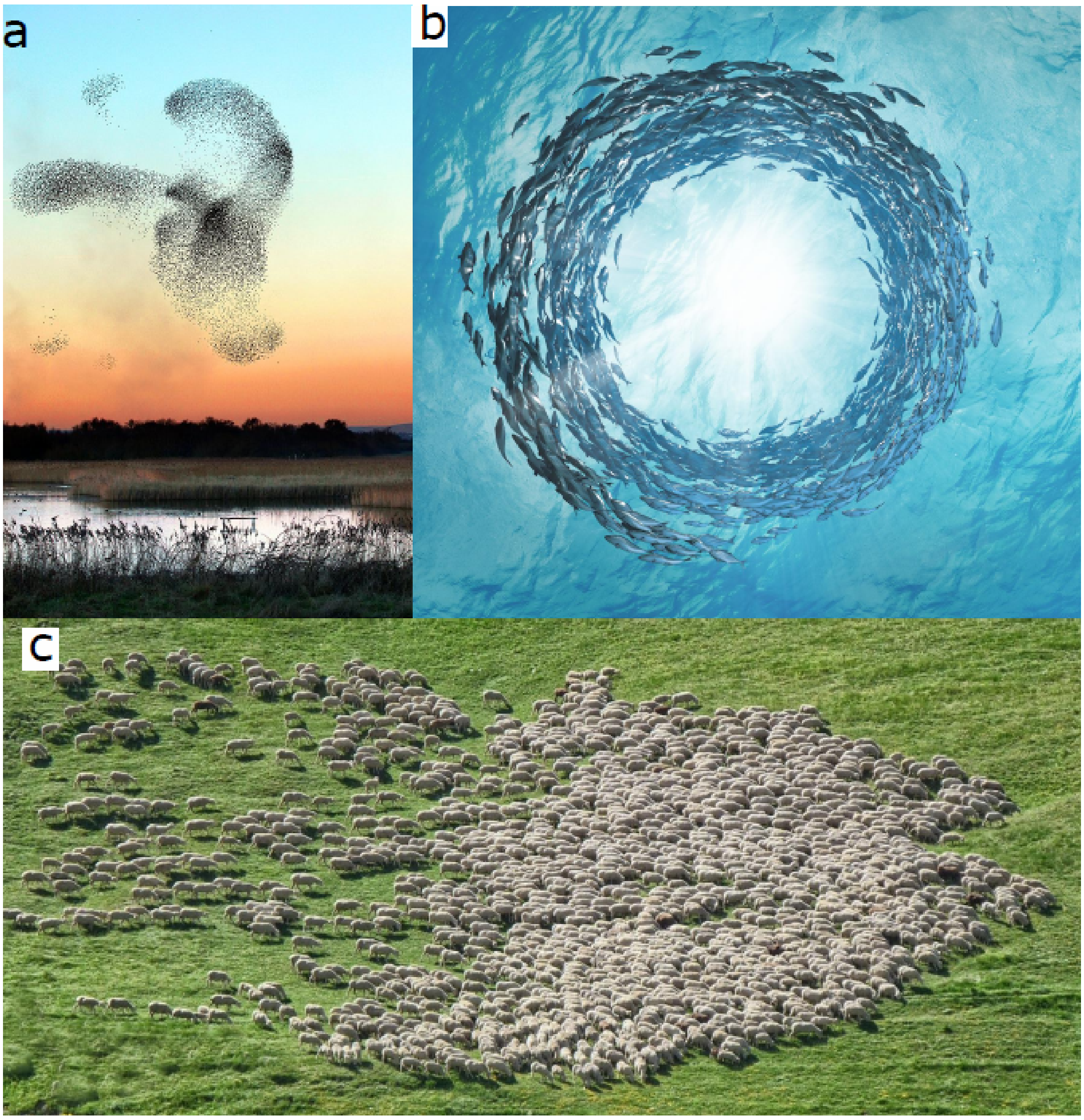

Figure 1: Examples of collective behaviour in nature. *a:* Swarming flock of birds (reused from [3]). *b:* Illustration of fish forming a vortex-alike structure (reused from [4]) *c:* An orientationally ordered herd of sheep (reused from [5]).

The emergence of such collective behaviours can be studied in many ways with different models adapted to how one wants to characterize the system. In biology a common method is to use agent-based modelling to try to reproduce some observed patterns. Then a certain set of rules for the behaviour of the individual agents is defined and tuned to obtain the same collective patterns that has been observed. In physics a more typical approach is to start by treating these agents as particles and define some fundamental interactions which will determine the motion of the particle. From these interactions the aim is to deduce a physical model in which one has limited the characteristics of the system down to a few, fundamental constants. Then the model can be used to simulate the system in search for different regimes of collective behaviour, and from this derive a general theory for such systems.

In physics we group systems that exert behaviour as described into the field of *active matter*. The defining property of active matter systems is that the particles have the ability to transform some kind of internal energy into mechanical motion and by this execute coherent movement [2, 6]. Living matter is regarded as the most important category of active matter, but non-living particles may also have such properties [7, 8]. When studying active matter, it is natural apply techniques from statistical physics. The main difference is however that the systems we study in active matter are out of equilibrium because energy is always introduced into the system by the self-propulsion of the particles. More specifically, these non-equilibrium systems are special because energy is introduced locally, and not by some external fields or boundaries. Another property is that active particles are often elongated or intrinsically polar. This means that their directed motion is a result of their own anisotropy, as opposed to an external field which is typical for other many-particle systems.

Active matter systems are typically divided into "dry" and "wet" systems [9, 10]. In dry systems the active particles exchange moment with a rigid substrate to achieve movement, and their interactions are typically short-range. Thus, the *models* that describe such systems may not take momentum conservation into account. On the other hand, wet system models describe situations where fluid flow is important and momentum is conserved. A typical example is suspensions of swimmers, where long-range hydrodynamic interactions are important. Note that the distinction between "wet" and "dry" applies to the models of the systems and not the systems themselves. Thus, a model of active particles moving in a fluid may well be considered as a dry system if friction forces and short-range interactions are dominant.

In this thesis we will study systems with pure hydrodynamic interactions. By hydrodynamic interactions we mean that the movement of an active particle causes a change in the velocity field of the surrounding fluid which is experienced by other particles. These interactions are interesting because they can be derived on a purely physical basis, without having to introduce any form of communication between the particles. Thus, it is easier to justify these models since such communication mechanisms can be tricky to derive on physical grounds. Furthermore, hydrodynamic interactions are typically long-range. This is an interesting attribute for any physical system, as it is not completely understood how this shapes the resulting behaviour on large scales. We will see later how this makes numerical simulations of bulk systems very challenging as one in principle cannot disregard the influence of particles infinitely far away.

The system we will be studying in this thesis is a 2D microscopical particle model of polar particles with pure hydrodynamic interactions. In particular, we will see if this model produces systems which display active turbulence. In the following an introduction to central concepts of inertial turbulence will be presented, before we look at how active turbulence is distinguished from this. Before the equations of motion for the system are presented, we will motivate them with hydrodynamic theory and present the Vicsek model. Finally, we will present and discuss the results obtained from simulations of the system.

2 Theory

2.1 Turbulence

Understanding turbulence is one of the oldest and greatest challenges in the field of physics. In Figure 2 we see a drawing of turbulent flow by Leonardo da Vinci dating back to the beginning of the 16^{th} century [11]. The fact that this phenomenon was attracting scientific interest this early gives us a sense of how compelling and ubiquitous turbulence is. The fact that it is still not fully understood shows how complex it is. Since da Vinci, many great scientists have tried to understand this phenomenon, and quite a few been quoted on its complexity. Richard Feynman referred to turbulence as "the most important unresolved problem of classical physics", and Sir Horace Lamb once said "I am an old man now, and when I die and go to Heaven there are two matters on which I hope enlightenment. One is quantum electro-dynamics and the other is turbulence of fluids. About the former, I am really rather optimistic" [12–14].

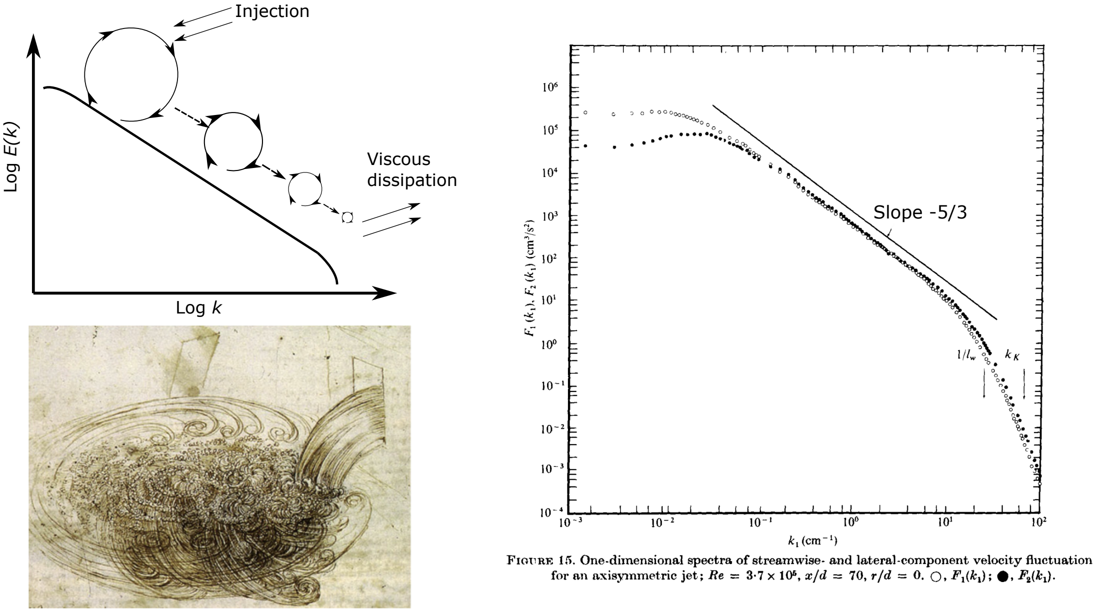

Figure 2: *Upper left:* Schematic illustration of the energy cascade which is characteristic for turbulence. Inspired by Ref. [15] *Lower left:* A sketch by Leonardo da Vinci illustrating turbulent-like behaviour of a fluid. Adapted from Ref. [16] *Right:* Experimental results showing $k^{-5/3}$ scaling of the energy spectrum. Adapted from [17].

Big whirls have little whirls that feed on their velocity,
and little whirls have lesser whirls and so on to viscosity.

- Lewis Fry Richardson [18]

This little poem by Lewis Fry Richardson paints a picture of the physical processes we call turbulence. Richardson was an early pioneer on the subject. A simple definition states that turbulence is the "departure in a fluid from a smooth flow". It is characterized by the appearance of volatile vortices and eddying motions on a wide range of scales. This occurs in fluids with high Reynolds numbers, Re, which defines a ratio of inertial forces to viscous forces. In contrast, smooth laminar flows occur at low Reynolds numbers. A turbulent flow is the result of the kinetic energy being too large to be damped by viscous forces. Thus energy is transported downwards across length scales until it is dissipated by viscous forces. This energy cascade is illustrated in Figure 2 by a typical energy spectrum $E(k)$ of turbulent flows. The energy spectrum is a measure of how much energy that is contained in motions on length scales corresponding to a wavenumber k. A turbulent flow is a chaotic process, meaning that a small change in initial conditions will lead to a large change in future conditions. Thus, we cannot study turbulence by deterministic means, like we e.g. study the velocity of a falling rock. Instead, we are left with studying its statistical properties [19].

A major breakthrough in the study of turbulence came when the mathematician Andrey Kolmogorov published his theory in three papers in 1941 [20–23]. Kolmogorov based his theory on the assumption that for all turbulent flows with high Reynolds number (high-Re flows), the statistics at small scales are universal and uniquely determined by the viscosity ν and energy dissipation rate ϵ. From this a characteristic length scale $\eta = \left(\nu^3/\epsilon\right)^{1/4}$ can be found. If energy is injected on a scale $L \gg \eta$, Kolmogorovs hypothesis was then that the statistics in the inertial range $\eta \ll r \ll L$ are universal and uniquely determined by the scale r and ϵ. From this he derived that the energy spectrum of a fully developed turbulent high-Re flow is given by

$$E(k) = K_0 \epsilon^{\frac{2}{3}} k^{-\frac{5}{3}} \tag{1}$$

as a function of the wavenumber k. K_0 would then be a universal constant. This applies to wavenumbers corresponding to scales r so that $\eta \ll r \ll L$, and is arguably the most famous result on inertial turbulence.

Kolmogorovs results have later been both confirmed experimentally, as the energy spectrum in Figure 2 from Ref. [17], and re-derived by others [24]. Unbeknownst of Kolmogorovs theory, Lars Onsager in 1945 also predicted a $-5/3$ power law scaling of the energy spectrum [25–27]. Onsager also reproduced Kolmogorovs 4/5 law,

$$\langle (\delta u_L(t, \boldsymbol{r}, \boldsymbol{R}))^3 \rangle = -\frac{4}{5}\epsilon R \tag{2}$$

for the third moment of the longitudinal velocity increment $\delta u_L(t, \boldsymbol{r}, \boldsymbol{R})$. δu_L is the difference in velocity along the direction $\boldsymbol{R}$ between point $\boldsymbol{r}$ and point $\boldsymbol{r} + \boldsymbol{R}$. In addition to this, Onsager connected the phenomenon of intermittency, highly irregular dissipation of energy at small scales, to the short-distance scaling of these velocity increments. Inertial turbulence is namely characterized by an increasing exponential broadening of the probability distribution function of the velocity increments $\delta \boldsymbol{u}(R)$ as the separation distance R decreases [28, 29]. The moments of the velocity increments $\langle (\delta \boldsymbol{u}(R))^n \rangle$ for $n = 1, 2, ...$ are known as structure functions. Kolmogorovs theory predicts that in general these structure functions scale as

$$\langle (\delta \boldsymbol{u}(R))^n \rangle = C_n (\epsilon R)^{n/3} \tag{3}$$

where C_n are some universal constants [30]. This has proven to be accurate for low orders only [29]. In particular the theory predicts that if $E(k) \sim k^{-\beta}$, then the second structure function should scale as

$$\langle (\delta \boldsymbol{u}(R))^2 \rangle \sim R^{\beta - 1} \tag{4}$$

if $1 < \beta < 3$. Onsager was also concerned with turbulence in two dimensional flows [25]. This is different from three dimensional turbulence because the reduced dimensionality generates different conservation laws, which leads to an inverse energy cascade from small scales to large scales [31, 32].

As the interest of inertial turbulence has grown and tools to characterize it has been developed, the possibility of studying turbulence in other systems has also been explored. One example of this is the discovery of turbulent-like behaviour in a flow of an elastic polymer solution by A. Groisman and V. Steinberg [33]. This phenomenon has later become known as elastic turbulence, and in contrast to inertial turbulence it is observed on low Reynolds numbers [34]. Another example is the investigation of turbulence in simulations of a quasistatic flow of granular media by F. Radjai and S. Roux [35], whose results are shown in Figure 5. Their characterization of the flow as turbulent-like is justified by three key observations. The first is that they observe a non-Gaussian broadening of the probability distribution function of the velocity increments at short time-scales, which in principle is equivalent to observing the same at short length-scales. Secondly, they find a power-law shape of the energy spectrum, but with an exponent $\beta \approx 5/4$, $E(k) \sim k^{-\beta}$, in contrast to Kolmogorovs 5/3 law. The third key observation is super-diffusion of the particles with respect to the mean background flow. This is expressed by the scaling of the relative root mean square displacement of the particles, which as a function of time evolves with an exponent $> 1/2$.

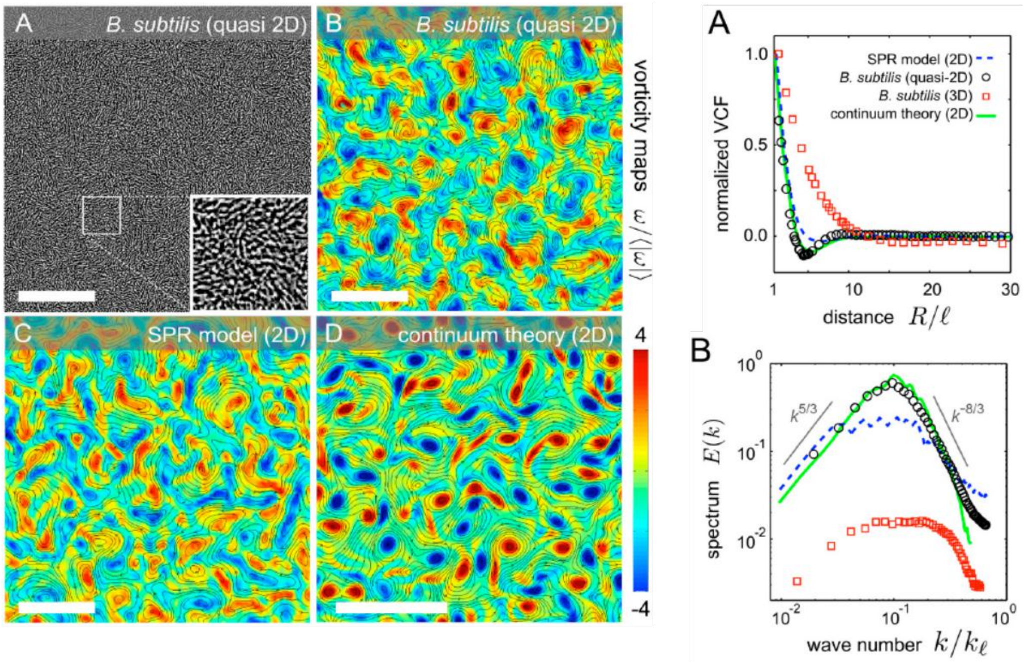

Figure 3: To the left we have an experimental snapshot of a quasi-2D bacterial suspension. We also see a vorticity map with flow streamlines of the same system. In addition we see vorticity maps obtained from simulations of a self-propelled rod (SPR) model and a hydrodynamic continuum model of an incompressible, active flow. To the right we see velocity correlation functions and energy spectra for the different cases. Both quasi-2D experimental results and the continuum model suggest power law behaviour of the energy spectrum. Figures adapted from [41].

2.2 Active Turbulence

The discovery of elastic turbulence [33] and study of turbulent-like behaviour in granular media [35] show that the characterizations of inertial turbulence can also be applied to other systems with entirely different underlying physical mechanisms. Since the turn of the millennium a number of experiments on active fluids have shown indications of mesoscale turbulence [36–43]. This has initiated studies on turbulent-like behaviours in such microbial suspensions and active systems in general, where an objective is to find generic descriptions for these dynamics, from now on termed *active turbulence*. The motion of swimming microorganisms occurs at practically zero Reynolds number, so inertia has no significance in such systems. This gives them an entirely different physical character than the high-Re fluid flows to which the Kolmogorov theory is applied. Inertial turbulence in high-Re flows is a result of energy injection at a scale where viscous dissipation is negligible. The inertial effects then generate energy transport across scales until viscous effects causes dissipation at a much smaller scale. In active systems however, the energy input takes place locally from its constituents and therefore at the scale of the flows. This means that the peaks of energy injection and dissipation are on the same scale. One still may have energy transport across scales in active systems, but there are examples where this is not possible [44]. These systems can however still produce non-trivial energy spectra because they self-organize and produce long-range correlations, leading to energy injection on different scales in the system [45]. Figure 3 shows active turbulence observed in experiments and obtained from simulations of a particle model and a continuum model, reused from Ref. [41]. The particle model is a self-propelled rod model which is a nematic model for dry active matter systems.

In Figure 4 we see another energy spectrum obtained from simulations of a continuum model. This figure is adapted from Ref. [44], which was published in 2020. The energy spectra show universal power law forms at both short and long wavelengths. We also see that there is characteristic length scale at which energy is injected into the system, represented by a local peak in the energy spectra. These properties are independent of system size and a given activity parameter. Based on these results it is concluded that active nematic fluids represents a distinct, low-Re universality class of turbulence. The plot of the stream function to the left shows that large scale flows form

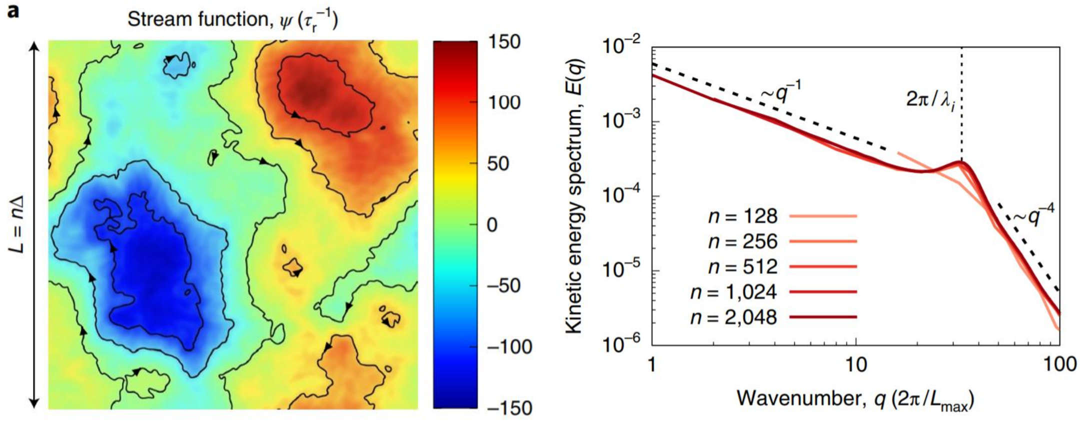

Figure 4: Stream function Ψ and energy spectra $E(q)$ as a function of wavenumber q, obtained from simulations of a continuum model for active nematic fluids. n represents the number of grid points on each axis, so the system size increases with n and thereby an activity number A also increases. The energy spectra show universal scaling laws q^{-1} for small q and q^{-4} for large q. Figure adapted from [44].

in the system, in addition to vortices with a size corresponding to the mentioned characteristic length.

2.2.1 Correlations and energy spectrum

As we have seen, it is common to use characterizations developed for inertial turbulence when studying active turbulence. We will now motivate the use of the energy spectrum and see where it originates. Most experimental results on active turbulence are obtained from 2D or quasi-2D systems, and we will also study a 2D model. The following discussion therefore considers 2D systems, but can easily be adapted to 3D.

The velocity field $\boldsymbol{u}(\boldsymbol{x}, t)$ of a fluid usually consists of a laminar and a turbulent component. The laminar component $\boldsymbol{U} = \langle \boldsymbol{u} \rangle$ is the spatial average of the flow and hence the turbulent component is $\boldsymbol{u}' = \boldsymbol{u} - \boldsymbol{U}$, which contains the properties we are interested in. With this we can define a velocity correlation tensor

$$R_{ij}(r) \equiv \langle u'_i(\boldsymbol{x}) u'_j(\boldsymbol{x} + \boldsymbol{r}) \rangle, \tag{5}$$

where the sub-indices i, j denote velocity components and the average may be both spatial and temporal. Note that the the correlation tensor is not dependent on the position $\boldsymbol{x}$ in this definition, which is only true if we assume the flow to be homogeneous. In addition, by assuming that the flow is isotropic, R_{ij} is only dependent of the distance r between the two points of the flow. The trace of the correlation tensor we call the correlation function $R(r) = R_{ii}(r)$. We observe that in the limit $r \to 0$, $R(r) \to \langle |\boldsymbol{u}'|^2 \rangle$. This correlation function can be used to define a correlation length

$$\lambda \equiv \frac{1}{R(0)} \int_0^\infty \mathrm{d}r \; R(r), \tag{6}$$

which is a rough measure of the largest eddy currents in the turbulent flow [19].

As discussed earlier, one of the characteristics of turbulence is energy transport over different scales. To get information on how much kinetic energy that is contained on these scales it may be preferable to look at the Fourier space rather than real space. The energy spectrum $E(k)$ is a a measure of the accumulation of energy at different wavenumbers k, and formally defined by

$$\frac{\langle \boldsymbol{u}'^2 \rangle}{2} = \int_0^\infty \mathrm{d}k \; E(k). \tag{7}$$

The left hand side is recognized as the total kinetic energy, since mass has no significance in the absence of inertia. Thus the energy spectrum shows how the kinetic energy is distributed on different length scales within a system. Having assumed that the turbulent flow is isotropic and homogeneous, the Wiener-Khinchin theorem states that the energy spectrum can be found by

$$E(k) = \frac{k}{2\pi} \int \mathrm{d}^2 r \; \mathrm{e}^{-\mathrm{i}\boldsymbol{k}\cdot\boldsymbol{r}} R(\boldsymbol{r}) \tag{8}$$

in a 2D system [41, 46]. Note that $E(k)$ contains the same amount of information about the system as $R(r)$, but displays it in a manner that can be more useful. We also note that multiplying the Fourier transform of a function with k in Fourier space is the same as differentiating the function with respect to r in real space. Thus, $E(k)$ illustrates the length scales where there are fluctuations in the velocity correlation function.

The definition of $E(k)$ in Eq. (8) relies on the validity of the assumptions Wiener-Khinchin theorem. As there are distinct phenomenological differences between active matter and systems where this theorem is applied ordinarily, we seek a definition of $E(k)$ with a more direct connection to the raw data. Starting from the simple definition of the mean square velocity

$$\langle \boldsymbol{u}'^2 \rangle = \frac{1}{L^2} \int \mathrm{d}^2 x \; \boldsymbol{u}'^2(\boldsymbol{x}) \tag{9}$$

for a continuum system of size L, we use the Parseval relation stating that

$$\int \mathrm{d}^2 x \; |\boldsymbol{u}'(\boldsymbol{x})|^2 = \int \mathrm{d}^2 k \; |\hat{\boldsymbol{u}}'(\boldsymbol{k})|^2, \tag{10}$$

where $\hat{\boldsymbol{u}}'(\boldsymbol{k})$ is the Fourier transform of $\boldsymbol{u}'(\boldsymbol{x})$ [47]. By assuming that $|\hat{\boldsymbol{u}}'(\boldsymbol{k})|^2$ is isotropic we may now write

$$\langle \boldsymbol{u}'^2 \rangle = \frac{2\pi}{L^2} \int \mathrm{d}k \; k |\hat{\boldsymbol{u}}'(\boldsymbol{k})|^2. \tag{11}$$

From the formal definition of $E(k)$, $\langle \boldsymbol{u}'^2 \rangle = 2 \int E(k) \mathrm{d}k$, we thus get that

$$E(k) = \frac{\pi}{L^2} k |\hat{\boldsymbol{u}}'(k)|^2. \tag{12}$$

We see how this definition allows us to use the Fourier transform of $\boldsymbol{u}$, in contrast to Eq. (8) where the velocity correlation function must be computed first. The Parseval relation is also applicable if we have a discrete velocity field with $\mathcal{N}$ points in each direction, so that

$$\langle \boldsymbol{u}'^2 \rangle = \frac{1}{\mathcal{N}^2} \sum_{i,j} |\boldsymbol{u}'(x_i, x_j)|^2 = \sum_{i,j} |\hat{\boldsymbol{u}}'(k_i, k_j)|^2, \tag{13}$$

where $\hat{\boldsymbol{u}}'(k_i, k_j)$ in this case is a discrete Fourier transform. Thus, we formally write

$$E(k) = \frac{\pi}{L^2} k \langle |\hat{\boldsymbol{u}}'(\boldsymbol{k})|^2 \rangle_k \tag{14}$$

in this case, where the average $\langle ... \rangle_k$ denotes the average over all wave-vectors $\boldsymbol{k}$ of length $k = |\boldsymbol{k}|$. Consequently, two different definitions of the energy spectrum have been obtained. In the literature it appears that use of the definition in Eq. (8) from the Wiener-Khinchin theorem is predominant. An example of this is the energy spectra in Figure 3 adapted from Ref. [41]. Figure 5 shows the energy spectra for the two velocity components in a granular flow, adapted from [35]. These results are obtained by interpolating the particle velocities on a grid and computing the Fourier transform of the turbulent part of the resulting velocity field. Thus, a method involving the definition of $E(k)$ as in Eq. (14) was used. In this work both methods will be applied to obtain the energy spectra.

As we saw in subsection 2.1, a common method in studies in inertial turbulence is to identify probability distribution functions for various velocity parameters. These parameters can for example be spatial derivatives of the velocities like $\partial v_x / \partial x$ or the velocity increment $\delta \boldsymbol{v}(t, \boldsymbol{r}, \boldsymbol{R}) = \boldsymbol{v}(t, \boldsymbol{r} + \boldsymbol{R}) - \boldsymbol{v}(t, \boldsymbol{r})$ [29]. Another possibility is to look at the probability distribution function for the particle displacement velocity $v_y(\tau) = \int_t^{t+\tau} \delta s_y(t') \mathrm{d}t'$ over time, where $\delta \boldsymbol{s}$ is a fluctuation from a mean background flow [35]. Figure 5 shows an example of this. What we observe here is a non-Gaussian broadening of the probability distribution at a short time scale. The occurrence of

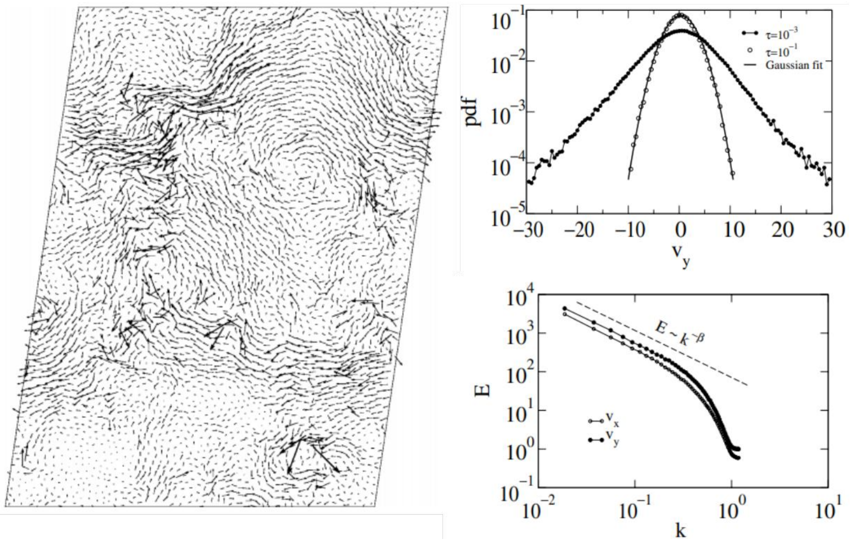

Figure 5: Turbulent-like behaviour in a simulated flow of granular media. To the left we see an instantaneous image of the particles displacements with respect to a mean background flow. The upper right plot shows the probability distribution function for the velocity increment v_y over two different times. The lower right plot to the right shows the energy spectrum for the turbulent part of the flow, showing a power law decay with $\beta = 5/4$. Figures are adapted from [35].

such broadening as time or spatial scales decrease is a hallmark of turbulence in inertia-dominated systems. This illustrates how one can adapt parameters and characteristics of inertial turbulence onto other systems to obtain similar descriptions of turbulent behaviour.

Another characteristic of turbulence is a non-zero vorticity $\boldsymbol{\omega} = \nabla \times \boldsymbol{u}$. For 2D systems we can reduce the vorticity to a scalar $\omega = \partial_x u_y - \partial_y u_x$. In Figure 3 we see examples of vorticity maps for active systems. The vorticity highlights eddying motions at different scales and can also give an impression of a typical vortex size in the system. Note that other behaviours and patterns than vortices may also induce a non-zero vorticity, such as e.g. two antiparallel lanes. Furthermore, one should be aware that a rich vorticity map is no concluding evidence of turbulence, but rather a tool to characterize the motions within a flow.

2.3 Continuum models

There are two main modelling techniques used to theoretically describe active systems. The first is a microscopical description where equations of motion are developed to describe the individual particles positions, velocities, orientations, etc. as functions of time. These models typically consist of a few inter-particle interactions that appear relatively simple on small scales, but can produce rich collective behaviours of particles on large scales. In this thesis we will consider such a particle model. The other alternative is to give a coarse-grained description of the systems by looking at the evolution of "slow", macroscopic variables. These models do not describe the motions of the individual particles, but instead considers the system as continuum. Typical such macroscopic parameters are the velocity field $\boldsymbol{u}$, the pressure p, a polarization field $\boldsymbol{P}$ and the density ρ. These parameters will then be connected by a set of differential equations to describe the dynamics of the system, normally on a form similar to the Navier-Stokes equation from fluid mechanics.

In continuum descriptions an ensemble of particles is often referred to as an active fluid. These active fluids are in most cases assumed to be incompressible, meaning that $\nabla \cdot \boldsymbol{u} = 0$. Thus the resulting models mainly apply to very dense suspensions [48]. With this assumption a general hydrodynamic description of the mobility of dense active suspensions reading

$$\partial_t \boldsymbol{u} + \lambda \boldsymbol{u} \cdot \nabla \boldsymbol{u} = -\nabla p - \Gamma_0 \nabla^2 \boldsymbol{u} - \Gamma_2 \nabla^4 \boldsymbol{u} - \left(\alpha + \beta |\boldsymbol{u}|^2\right) \boldsymbol{u}, \tag{15}$$

has been developed [41, 49]. We emphasize that $\boldsymbol{u}(\boldsymbol{r}, t)$ here describes the velocity of an active particle at position $\boldsymbol{r}$ and time t and not the surrounding, passive fluid. The left hand side and the two first terms on the right we recognize from the conventional Navier-Stokes equation describing an incompressible fluid. Although these equations have similarities, they describe very different physics. In addition the right hand side consists of a higher order gradient in form the Γ_2 term and lastly the α, β term which is similar to Toner-Tu drive [49–51]. The $\Gamma_{0,2}$-terms induce instabilities to the system which lead to quasi-chaotic patterns. With these terms only the equation provides the simplest generic description of meso-scale turbulence in active flows [41]. The α, β term accounts for the self-propulsion of the constituents. α is a parameter describing the activity of the system. $\alpha < 0$ describes high activity and then the α, β-terms describe an effective polar alignment, while $\alpha > 0$ describes friction dominated behaviour leading to damped, disordered states [52].

Continuum models like the one described in Eq. (15) has had great success in describing a wide variety of behaviours in different systems, including active turbulence [2, 45]. We have already shown one example in Figure 3 where this model shows very good agreement with experimental results from a dense bacterial suspension in a quasi-2D system. With their similarity to the Navier-Stokes equation, which is used to describe inertial turbulence, it is natural that continuum models has been the main focus in studies of active turbulence. In contrast there is strikingly little literature on active turbulence in microscopic particle models, especially in the case of wet, polar systems. This is mainly because they are computationally heavy to simulate. These models can account for features like compressibility, which indeed is relevant for many real-world systems, which are not captured by most of the continuum descriptions. It is therefore of interest to see whether these models can produce similar results.

2.4 Vicsek model

One of the most influential models in Active Matter is the Vicsek model [53]. It was initially developed to study the collective motion of birds [7], but proved to describe many more phenomena. The model has been further investigated and expanded to take into account other sorts of effects like attraction/repulsion, a surrounding fluid etc. [54–59]. The Vicsek model is in the category of dry active matter systems.

The original Vicsek model deals with point particles moving with a constant absolute velocity v_0. At every time step, the orientation θ_i of each particle is decided by the average of the orientations of the particles within a radius r from the particle. This is illustrated in Figure 6. In addition there is a rotational diffusion term Ξ, which is a randomly chosen number from a uniform distribution on a given interval $(-\eta/2, \eta/2)$. Therefore, for a particle i in this model at position $\boldsymbol{x}_i(t)$ and with orientation $\theta_i(t)$ at time t, will at time $t + \Delta t$ be at position

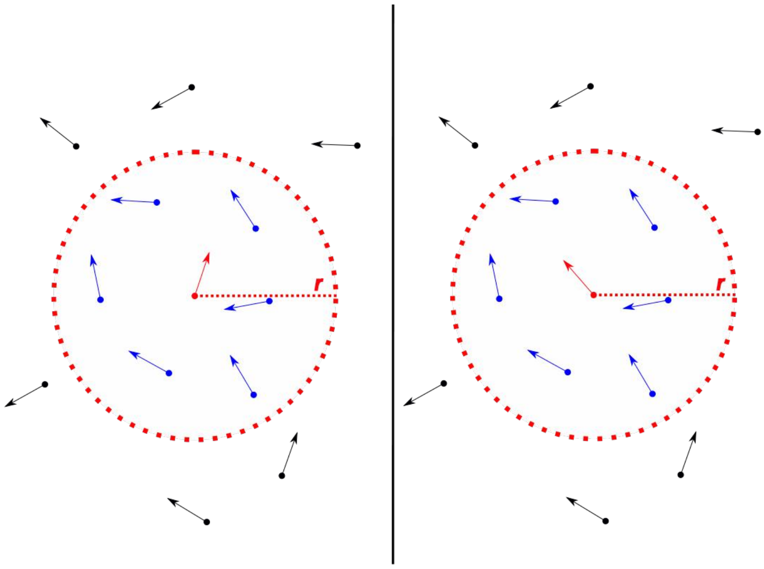

Figure 6: Illustration of the interactions in the Vicsek model. The orientation of each particle is decided by the average orientation of all particles within a distance r from the given particle.

$$\boldsymbol{x}_i(t + \Delta t) = \boldsymbol{x}_i(t) + \boldsymbol{v}_i(t)\Delta t, \tag{16}$$

with orientation

$$\theta_i(t + \Delta t) = \langle \theta(t) \rangle_r + \Xi. \tag{17}$$

$\boldsymbol{v}_i(t)$ is the velocity of the particle, with absolute value v_0 and direction $\theta_i(t)$, while $\langle \theta \rangle_r$ denotes the average velocity direction of particles within a distance r from particle i. This means that a given system can be characterized by only three parameters v_0, η and the density ρ.

A striking property of the Vicsek model is its simple form, and it has a strong analogy in the classical Heisenberg model in statistical physics. The direction of the moving arrows can be thought of as 'spins', while the noise term Ξ induces much of the same effects as temperature does in statistical physics. The two models yield qualitatively similar results with respect to global order of their respective systems. This is far from granted, given that the Vicsek model deals with non-equilibrium systems.

From a physicist's perspective, the Vicsek model is attractive because it consists of few parameters and produces spontaneous symmetry breaking and critical exponents. This is why it has played a central role in the development of the theory around collective motion since it was introduced in the 1990's [54]. However, the Vicsek model is not derived from any physical law but rather from a notion of how the constituents of a flock behave. Thus, it is an example of agent-based modelling that was touched upon in the Introduction.

2.5 Flying XY-model

The Vicsek model can be modified to construct a system in which the particles interact by a pairwise aligning force. The motion of a self-propelled particle i in 2D moving with constant speed v is described by

$$\dot{\boldsymbol{x}}_i(t) = v\boldsymbol{e}_{\theta_i}(t), \tag{18}$$

$$\dot{\theta}_i(t) = \gamma \sum_{j \neq i} F\left(\theta_j(t) - \theta_i(t), \boldsymbol{x}_j(t) - \boldsymbol{x}_i(t)\right) + \Xi(t), \tag{19}$$

where γ is a coefficient describing the strength of the alignment interaction and Ξ is some white noise term with zero mean [60]. By choosing an alignment force F on the form $F(\theta, \boldsymbol{r}) = \sin(\theta) f(|\boldsymbol{r}|)$, where $f(r)$ determines the range of the interaction, we see how this interaction incentivizes particles to orientate in parallel to each other. Both $\theta_i = \theta_j$ and $\theta_i = -\theta_j$ are "equilibrium states" in the sense that these conditions yield 0 contribution to $\dot{\theta}_i$, but in the anti-parallel situation this equilibrium is not stable. This model thus describes a polar system, not a nematic one. In the limit $v = 0$ this model is equivalent to the classical XY-model in statistical mechanics [60]. This is a model for the 2D configuration of fixed spins on a lattice where a translation-invariant interaction J_{ij} analog to $f(r)$ determines the coupling between the sites i and j. The configuration energy $H = -\sum_{i \neq j} J_{ij} \cos(\theta_i - \theta_j)$ determines the state of of the system. For the spin at site i the minimal configuration energy is found by $-\partial H / \partial \theta_i = \sum_{j \neq i} J_{ij} \sin(\theta_j - \theta_i)$ which we see is equivalent to the interaction in Eq. (19). Therefore, with a finite velocity v the model above is termed the Flying XY-model.

As stated above $f(r)$ controls the range of the aligning interaction. A straightforward choice is to simply set a cutoff R so that $f(r) = 1/\pi R^2$ if $r < R$ and 0 otherwise as done in Ref. [60]. There it is also claimed that the physics should not be dramatically affected by the exact shape of this function. Another possibility, which we will investigate further, is to let the range be controlled by an exponent α so that $f(r) \sim r^{-\alpha}$. With this form we also incorporate that the particles are most affected by their closest neighbours. One should however be aware that with $\alpha \leq 2$ the interaction is long-range in 2D systems. Otherwise this is a short-range interaction.

In active systems there are several possible physical origins that can justify the aligning interactions in both the conventional Vicsek model and the flying XY-model. It is easy to imagine how an individual in a flock of birds or in a school of fish simply sees the other individuals and thereby adjusts its own orientation. For microswimmers in 2D systems such an alignment interaction can arise from short-range hydrodynamic interactions [61]. It is also remarkable that an effective Vicsek-like interaction can be present in systems composed of self-propelled particles with only steric interactions. In combination with self-propulsion, the repulsive potential which models the steric interaction induces a Motility-Induced Phase Separation (MIPS) between dense and dilute fluid phases [62]. In the dense phase of a MIPS an alignment of the velocities of the particles can arise, even though no explicit alignment interaction is present [63]. This is illustrates how the Flying XY-model captures features and behaviours that may be present in a variety of systems.

We note that both the Vicsek model and the flying XY-model contain noise terms to incorporate angular diffusion. This is a common feature in microscopic and macroscopic models of active matter to have an order-breaking mechanism in the models. We will however study a model with pure hydrodynamic interactions and no such noise term.

2.6 Hydrodynamic theory

The Vicsek model is a minimal model to describe active systems. After it was introduced many other theories and models have been developed to understand the behaviour of active systems [10, 64]. The focus in this project will be on active systems with hydrodynamic interactions. This is fundamentally different from the Vicsek model in the sense that the interactions will be long-range and the equations of motion will be deterministic. More specifically, we will look at swimming microorganisms confined in a 2D fluid. In Figure 7 we see how such systems can exert different kinds of behaviour.

Figure 7: Different collective behaviours of a dense suspension of the bacterium B. subtilis in a drop

Source: Enkeleida Lushi, Hugo Wioland and Raymond E. Goldstein [65]

As opposed to for example fish, swimming microorganisms live their life in a world with very low Reynolds number. This is simply caused by their size, which has been described in the famous lecture "Life at low Reynolds number" by E. M. Purcell [66]. In this world inertia does not play any role in the motion of a particle, which is entirely dependent on the forces acting on it at this point in time. Purcell also stated that because of time-reversibility, an animal (or anything else) which exhibits reciprocal motion cannot swim at low Reynolds number. This is known as the Scallop theorem.

To see how the low Reynolds number influences the hydrodynamic interactions, we start by introducing the Navier-Stokes equation. It describes the flow $\boldsymbol{u}$ of an incompressible fluid by

$$\rho\left(\frac{\partial \boldsymbol{u}}{\partial t} + (\boldsymbol{u}\cdot\nabla)\boldsymbol{u}\right) = -\nabla p + \eta\nabla^2\boldsymbol{u} \tag{20}$$

where p is the pressure, η is the viscosity and ρ is the density of the fluid. With low Reynolds number, the two inertia terms on the left-hand side can be ignored. We thus get the Stokes equations describing a Newtonian fluid,

$$\begin{aligned} \eta\nabla^2\boldsymbol{u} &= \nabla p \\ \nabla\cdot\boldsymbol{u} &= 0 \end{aligned} \tag{21}$$

where the second equation originates from the incompressibility. Hele-Shaw flow is an example of a situation where inertia forces are negligible. It occurs when two parallel plates are arranged very close together with the space between the plates occupied by fluid.

We now look at a swimmer in a fluid confined by two rigid walls separated by a distance h comparable to the size of the swimmer as illustrated in Figure 8. This is a relevant situation for bacteria in nature and is also a common case in experiments [61, 67, 68]. When studying swimming microorganisms in an experimental setup with e.g. a microscope, the swimmers will typically be confined between two glass plates. In nature we can think of situations like bacteria moving along surfaces, in porous media or through narrow passages in the body. Thus, confinement between two plates will at least be a minimal model for such situations. The swimmers we treat are polar, meaning that they are asymmetric along the elongation axis and thus have a "head" and a tail.

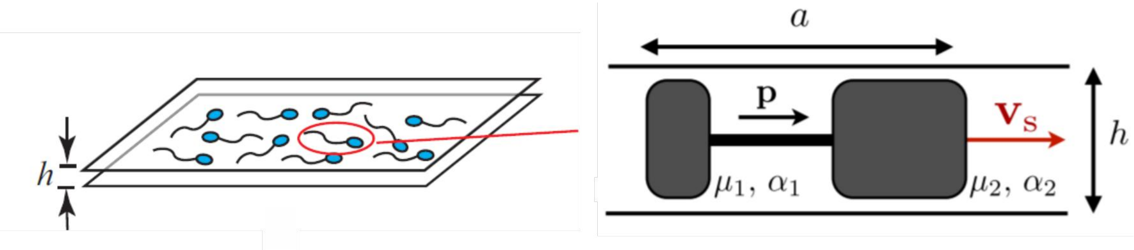

Figure 8: A suspension of swimming microorganisms in a fluid confined between two parallel plates separated by a distance h comparable to the size of the swimmers. The swimmers are modelled by an asymmetric dumbbell moving with an absolute velocity v_s and with orientaion $\boldsymbol{p}$ in the plane parallel to the plates.

Source: Alan Cheng Hou Tsang and Eva Kanso [69] and Tommaso Brotto *et. al.* [9]

With no-slip condition on the walls, the flow field induced by a swimmer can then be reduced to two dimensions (x, y) in the far-field [69–72]. From the Eqs. (21) one can then derive that the flow will be parallel to the plates and the velocity field $\boldsymbol{u}$ is described by

$$\begin{aligned} \boldsymbol{u}\left(\boldsymbol{r}\right) &= -\frac{h^2}{12\eta}\nabla p(\boldsymbol{r}) \\ \nabla\cdot\boldsymbol{u}\left(\boldsymbol{r}\right) &= -\boldsymbol{\sigma}\cdot\nabla\delta\left[\boldsymbol{r}-\boldsymbol{R}(t)\right] \end{aligned} \tag{22}$$

where $\boldsymbol{R}$ is the position of the swimmer and $\boldsymbol{\sigma} = \sigma\left[\dot{\boldsymbol{R}}(t) - \boldsymbol{u}^{(0)}(\boldsymbol{R}(t))\right]$ [9]. These equations describe what is known as Hele-Shaw flow. σ is a measure of the "dipole strength", and for a circular particle it is twice the particle area. $\boldsymbol{u}^{(0)}(\boldsymbol{R}(t))$ would be the fluid flow at $\boldsymbol{R}(t)$ in absence of the swimmer. The equations in (22) have a dipolar solution

$$\boldsymbol{u}^d(\boldsymbol{r}|\boldsymbol{0},\boldsymbol{\sigma}) = \frac{1}{2\pi|\boldsymbol{r}|^2}\left(\hat{\boldsymbol{r}}\hat{\boldsymbol{r}} - \boldsymbol{I}\right)\cdot\boldsymbol{\sigma} \tag{23}$$

for a particle located at the origin $\boldsymbol{R} = \boldsymbol{0}$ [72]. $\boldsymbol{I}$ is the unity tensor and $\hat{\boldsymbol{r}}\hat{\boldsymbol{r}}$ is the outer product of $\hat{\boldsymbol{r}} = \boldsymbol{r}/|\boldsymbol{r}|$ with itself, i.e. $(\hat{\boldsymbol{r}}\hat{\boldsymbol{r}})_{i,j} = \hat{r}_i\hat{r}_j$. In fact, this far-field solution is independent of the propulsion mechanism that drives the motion of the particle, because the physics of the surrounding fluid is described by Hele-Shaw flow [69, 73]. Figure 9 illustrates the dipolar field in Eq. (23) when the particle moves to the right and no other fluid flows are present. This *source* dipole that we obtain for swimmers confined in 2 dimensions is qualitatively different from the resulting velocity field that is obtained when the swimmers are free to move in 3 dimensions. In 3D one has to distinguish between "pushers" and "pullers" and so the resulting fluid flow is no longer independent of the swimming mechanism [69, 74].

Brotto *et. al.* [9] describes a model that treats the swimmer as a rigid dumbbell, illustrated in Figure 8, and this has been adopted by Kanso and Tsang [69, 75] and Saintillan and Lefauve [71]. The dumbbell is composed of two discs with radii R_{tail} and R_{head} connected by a rigid rod of length a. Note that the dumbbell here moves with a velocity v_s, so this is not a model for the swimming mechanism of the swimmer, but for the velocity field created by the motion of the swimmer. A dumbbell would by the Scallop theorem not be able to self-propel. It has however been showed that collective motion of pulsating dumbbells also can occur purely due to hydrodynamic interactions [76].

The "tail disc" is a simple model to describe the effects the beating flagella has on the fluid flow. Kanso and Tsang established that R_{tail} indeed depends on the flagellar activity of the swimmer [69].

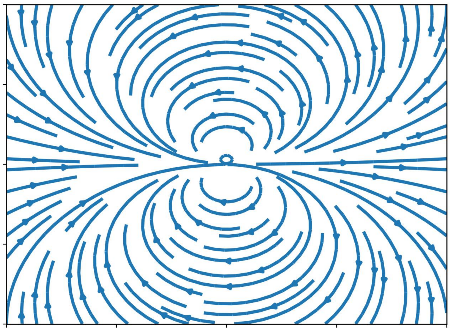

Figure 9: A stream plot of the dipolar velocity field described in Eq. (23). This demonstrates the far-field fluid flow induced by a particle moving to the right with no other flows present.

This was done by prescribing the gap-averaged motion of the flagellum as $y(x,t) = A\cos{(kx - t)}$ with $x \in [-1, 1]$ and assuming that it induces a constant swimming velocity U. A and k are the amplitude and wave number of the beating motion, respectively. By doing numerical simulations and fitting the obtained time time-averaged flow field over one beating cycle to a dipolar field, they found that R_{tail} increases with A and k.

3 Equations of Motion for Confined Polar Swimmers

3.1 Hydrodynamic interactions

In this section we will mainly follow Brotto et. al. [9] and use the dipolar velocity field in Eq. (23) to express the hydrodynamic interactions between the particles. The generic form of the equations of motion for a polar swimmer with absolute velocity v_s in a flow field $\boldsymbol{u}$ is

$$\dot{R}_\alpha = v_s p_\alpha + \mu_\perp \left(\delta_{\alpha\beta} - p_\alpha p_\beta\right) u_\beta + \mu_\parallel \left(p_\alpha p_\beta\right) u_\beta \tag{24a}$$

$$\dot{p}_\alpha = \nu_1 \left(\delta_{\alpha\beta} - p_\alpha p_\beta\right) \left(\partial_\gamma u_\beta\right) p_\gamma + \nu_2 \left(\delta_{\alpha\beta} - p_\alpha p_\beta\right) u_\beta \tag{24b}$$

to leading order of $|\nabla \boldsymbol{u}|$, on component form with indices $\alpha,\ \beta \in (x, y)$ and with the Einstein summation convention [9, 71]. The orientation vector $\boldsymbol{p} = (\cos\alpha, \sin\alpha)$ is given with respect to the x-axis. (The angle α must not be confused with the index.) $\mu_\perp$ and $\mu_\parallel$ are the transverse and longitudinal mobility coefficients, respectively, and ν_1 and ν_2 we will denote as flow alignment coefficients. Note that the factor $(\delta_{\alpha\beta} - p_\alpha p_\beta)$ is a projection operator. By multiplying Eq. (24b) with p_α we get that $p_\alpha \dot{p_\alpha} = 0$. Therefore $\dot{\boldsymbol{p}}$ is always perpendicular to $\boldsymbol{p}$ and it depends only on the components of $(\nabla \boldsymbol{u}) \cdot \boldsymbol{p}$ and $\boldsymbol{u}$ that are perpendicular to $\boldsymbol{p}$.

To get a feeling for the interpretation of the coefficients ν_1 and ν_2, it is instructive to have look at how the two terms in Eq. (24b) contribute to $\dot{\boldsymbol{p}}$, or more specifically when they do not contribute. The first term is hard to interpret, but can be shown to be zero if $\boldsymbol{p} \parallel \nabla(\boldsymbol{u}^2)$. A special case of this is if $\nabla u_x = \nabla u_y = C\boldsymbol{p}$, where C is a constant. Written out on vector form the gradient term then is

$$C \begin{pmatrix} 1 - p_x^2 & -p_x p_y \\ -p_x p_y & 1 - p_y^2 \end{pmatrix} \begin{pmatrix} p_x & p_x \\ p_y & p_y \end{pmatrix} \begin{pmatrix} p_x \\ p_y \end{pmatrix} = C \begin{pmatrix} (1 - p_x^2)(p_x^2 + p_x p_y) - p_x p_y (p_y^2 + p_x p_y) \\ (1 - p_y^2)(p_y^2 + p_x p_y) - p_x p_y (p_x^2 + p_x p_y) \end{pmatrix} \tag{25}$$

which is zero by using that $p_x^2 + p_y^2 = 1$. This tells us that ν_1 is a measure of how strong the particle tends to reorient by the flow gradient [71]. In fact, if $\nu_2 = 0$ Eq. (24b) corresponds to what is known as Jefferey's equation which describes how passive, anisotropic particles respond to fluid flow [9, 77]. This was introduced in 1922, and the resulting Jeffery orbits are well-studied.

The second term in Eq. (24b) is a bit more "transparent". By setting $\boldsymbol{p} = C\boldsymbol{u}$ it is quite straightforward to see that this term becomes 0. This means that by the ν_2-term, the particle reorients in response to the flow field itself, not its gradient. This behaviour is not as well-studied as the gradient response.

Now, we return to the dumbbell model described in the section Hydrodynamic theory and Figure 8. We consider the two disks of radii $\{R_\text{tail}, R_\text{head}\}$ to be fixed together by a rod such that the length of the dumbbell is a. We assume $a \gg R_\text{tail}, R_\text{head}$. Because of the geometric confinement of our system, the disks can experience a lubrication force from the walls at $z = 0, h$, and vice versa. This will slow down the disk velocity $\dot{\boldsymbol{R}}_i$ compared to the fluid velocity $\boldsymbol{u}(\boldsymbol{R}_i)$. Following Brotto *et. al.* [9] we therefore introduce a mobility coefficient $\mu_i \in [0, 1]$ so that $\dot{\boldsymbol{R}}_i(t) = \mu_i \boldsymbol{u}(\boldsymbol{R}_i)$, to take this effect into account. $\mu_i = 0$ means that a passive disk would be fixed, while for $\mu_i = 1$ it would be a passive tracer of the fluid. Here $i = 1, 2$ represents the tail and the head, respectively. To account for the drag from the surrounding fluid they also introduce a drag coefficient α_i. The interpretation of this is that if a disk is pulled by an external force $\boldsymbol{F}$ in a quiescent fluid, i.e. a fluid that is otherwise at rest, its velocity will be $\dot{\boldsymbol{R}}_i(t) = \alpha_i \boldsymbol{F}$.

We are now in a position to look at the motion of this rigid dumbbell, assuming that both disks move with a velocity $v_s^{(0)}\boldsymbol{p}$. The equations of motion for the tail (1) and head disc (2) are then

$$\begin{aligned} \dot{\boldsymbol{R}}_1 &= v_s^{(0)}\boldsymbol{p} + \mu_1 \left[\boldsymbol{u}^{(0)}(\boldsymbol{R}_1) + \boldsymbol{u}^d(\boldsymbol{R}_1 | \boldsymbol{R}_2, \boldsymbol{\sigma}_2)\right] + \alpha_1 \boldsymbol{T}, \\ \dot{\boldsymbol{R}}_2 &= v_s^{(0)}\boldsymbol{p} + \mu_2 \left[\boldsymbol{u}^{(0)}(\boldsymbol{R}_2) + \boldsymbol{u}^d(\boldsymbol{R}_2 | \boldsymbol{R}_1, \boldsymbol{\sigma}_1)\right] - \alpha_2 \boldsymbol{T}, \end{aligned} \tag{26}$$

respectively, where $\boldsymbol{T}$ is a tension that ensures that the distance between the disks is constant. We see that there are four terms determining the motion of each disk. $v_s^{(0)}\boldsymbol{p}$ is the self-propulsion term and moves both disks in the direction of $\boldsymbol{p}$, which is parallel to the axis between the two disks. The impact from the fluid is expressed by the term $\mu_i[...]$, with $\boldsymbol{u}^{(0)}$ being the velocity field if the dumbbell was not present. $\boldsymbol{u}^d(\boldsymbol{R}_1|\boldsymbol{R}_2,\boldsymbol{\sigma}_2)$ is the dipolar velocity field of the fluid at $\boldsymbol{R}_1$ given that there is particle with dipole strength $\boldsymbol{\sigma}_2$ located at $\boldsymbol{R}_2$, and vice versa for $\boldsymbol{u}^d(\boldsymbol{R}_2|\boldsymbol{R}_1,\boldsymbol{\sigma}_1)$, given by Eq. (23). If the other forces leads to a extraction/contraction Δa of the dumbbell, $\pm\alpha_i\boldsymbol{T}$ will move disk i directly towards/away from the other by a distance $\Delta a\alpha_i/(\alpha_1+\alpha_2)$. Thus, for a discrete time step δt we have $\boldsymbol{T}(t)\parallel\boldsymbol{p}(t+\delta t)$.

Again, following of Brotto *et. al.*, we can now define the center of drag of the dumbbell as $\boldsymbol{R}\equiv(\alpha_1\boldsymbol{R}_2+\alpha_2\boldsymbol{R}_1)/(\alpha_1+\alpha_2)$. Then the equations in (26) can be rewritten to the form of Eqs. (24a) and (24b) with velocity $v_s=v_s^{(0)}+\mathcal{O}\left((R_i/a)^2\right)$, $i=(\text{tail, head})$. The transverse and longitudinal mobility coefficient for this swimmer will then be

$$\mu\equiv\mu_\perp=\mu_\parallel=\alpha_2\mu_1+\alpha_1\mu_2 \tag{27a}$$

and the flow alignment coefficients

$$\nu_1\sim(\mu_1+\mu_2),\ \text{and} \tag{27b}$$

$$\nu_2=\frac{1}{a}(\mu_2-\mu_1). \tag{27c}$$

to leading order of R_i/a. With $\mu\equiv\mu_\perp=\mu_\parallel$ Eq. (24a) now becomes significantly simplified, $\dot{R}_\alpha=v_sp_\alpha+\mu u_\alpha$.

From Eq. (27c) it is clear that $\nu_2\neq0$ is a result of the geometrical confinement ($\mu_1,\mu_2\neq1$) and the polarity of the swimmer ($\mu_1\neq\mu_2$). A reasonable assumption is that μ_i decreases with R_i, meaning that larger particles experience more friction from the walls than smaller ones. For a specific swimmer we can take R_head to be a constant. R_tail will however vary with the flagellar activity, as mentioned earlier. This will then also be the case for the mobility coefficient μ_1. Swimmers with high flagellar activity will therefore align them-self along with the velocity field due to the ν_2 term in Eq. (24a) and $\nu_2>0$ in this case. On the other hand, swimmers with weakly (or slowly) beating flagella can yield $\mu_1>\mu_2$ and therefore $\nu_2<0$. In this case they will orient against the flow and swim upstream.

To simplify the equations of motion we will assume that $\boldsymbol{\sigma}=\sigma\left[\dot{\boldsymbol{R}}(t)-\boldsymbol{u}^{(0)}(\boldsymbol{R}(t))\right]\approx\sigma v_s\boldsymbol{p}$, i.e. that the swimmers velocity is constant and large compared to the fluid velocity and that the direction of its movement follows its swimming direction $\boldsymbol{p}$. This is justified by the $1/r^2$ decay of the dipolar flow field induced by the swimmer. It should however be noted that systems of this kind may end up in a clustering state where the particles velocities are close to zero [69]. In such an event one should take a closer look at the implications this assumption. We can now rewrite the dipole velocity field in Eq. (23) as

$$\boldsymbol{u}^d(\boldsymbol{r}|\boldsymbol{0},\boldsymbol{\sigma})=\frac{v_s\sigma}{2\pi|\boldsymbol{r}|^2}(\hat{\boldsymbol{r}}\hat{\boldsymbol{r}}-\boldsymbol{I})\cdot\boldsymbol{p}=\frac{v_s\sigma}{2\pi|\boldsymbol{r}|^2}\begin{pmatrix}\left(\hat{r}_x^2-\hat{r}_y^2\right)\cos\alpha+2\hat{r}_x\hat{r}_y\sin\alpha\\ \left(\hat{r}_y^2-\hat{r}_x^2\right)\sin\alpha+2\hat{r}_x\hat{r}_y\cos\alpha\end{pmatrix} \tag{28}$$

where $\hat{r}_x=x/|\boldsymbol{r}|$, $\hat{r}_y=y/|\boldsymbol{r}|$ and thus $\hat{r}_x^2+\hat{r}_y^2=1$. Remember that $\boldsymbol{p}=(\cos\alpha,\sin\alpha)$ is the orientation of the swimmer producing the flow field.

For the following discussion it is advantageous to look at the derivative of the angle α instead of the orientation $\boldsymbol{p}$ as in Eq. (24b). They both contain the same amount of information, but the notation changes slightly. By the use of a few trigonometric identities and that $\dot{\boldsymbol{p}}=\dot{\alpha}(-\sin\alpha,\cos\alpha)$ we obtain that

$$\dot{\alpha}=\nu_1\boldsymbol{p}^\perp\cdot(\nabla\boldsymbol{u})\cdot\boldsymbol{p}+\nu_2\boldsymbol{u}\cdot\boldsymbol{p}^\perp, \tag{29}$$

where $\boldsymbol{p}^\perp=(-\sin\alpha,\cos\alpha)$ is a vector perpendicular to $\boldsymbol{p}$.

3.2 Alignment interaction

We now want to incorporate the alignment interaction from the flying XY-model. As discussed in subsection 2.5, this interaction has a generic form and may originate from several physical phenomena, including hydrodynamic interactions [60, 61]. Another motivation for including this interaction is that the model we are studying is unreservedly 2-dimensional. This is seldom the case in real systems, who are rather quasi-2D in the sense that the both fluid flow and particle movement in a third dimension is quite restricted. When these systems are modelled as 2D, it may be done by coarse-graining so that one simulated particle in reality represents a group of particles. It has experimentally been discovered active fluids which exhibit coherent motion with global order in 3D, but as one of the dimensions is diminished to be much smaller than the others, the active flow turns turbulent [78]. One can thus envision a 2D model of such a system where an alignment interaction as in the flying XY-model effectively compensates for the lack of a third dimension. Inspired by Ref. [61], we introduce an effective angular potential H_{eff} so that the rotation of a self-propelled particle i in a system of N particles is given by

$$\dot{\alpha}_i = \sum_{j\neq i}^{N} \frac{\partial}{\partial \alpha_i} H_{\text{eff}}(\alpha_i, \alpha_j, \boldsymbol{r}_i - \boldsymbol{r}_j). \tag{30}$$

This effective potential takes the generic form

$$H_{\text{eff}}(\alpha_i, \alpha_j, \boldsymbol{r}) = A(r)\boldsymbol{p}_j \cdot \boldsymbol{p}_i + B(r)\hat{\boldsymbol{r}} \cdot \boldsymbol{p}_i + C(r)\boldsymbol{p}_j \cdot (2\hat{\boldsymbol{r}}\hat{\boldsymbol{r}} - \boldsymbol{I}) \cdot \boldsymbol{p}_i \tag{31}$$

which is expected whenever particles move with constant velocity and experience short-range polar alignment. In systems with global rotational invariance, no other low-order moments are allowed due to symmetry considerations [79]. We see that the only dependence of α_i in H_{eff} comes with $\boldsymbol{p}_i$, whose derivative is $\boldsymbol{p}_i^{\perp}$, so that

$$\frac{\partial}{\partial \alpha_i} H_{\text{eff}}(\alpha_i, \alpha_j, \boldsymbol{r}) = A(r)\boldsymbol{p}_j \cdot \boldsymbol{p}_i^{\perp} + B(r)\hat{\boldsymbol{r}} \cdot \boldsymbol{p}_i^{\perp} + C(r)\boldsymbol{p}_j \cdot (2\hat{\boldsymbol{r}}\hat{\boldsymbol{r}} - \boldsymbol{I}) \cdot \boldsymbol{p}_i^{\perp}. \tag{32}$$

We now see that the first term takes the form of the alignment interaction from the flying XY-model in subsection 2.5. Such an interaction originating from hydrodynamic effects is short-range in 2D flow [61, 72]. If rooted in other effects, like e.g. collisions, this term is also typically of short range. We therefore choose $A(r) = \gamma r^{-\zeta}$ where $\zeta \geq 3$ when including this interaction in our model. γ is a flow alignment parameter in line with ν_1 and ν_2, indicating the strength of the alignment.

The second term in Eq. (32) is a collision avoidance term which orientates the swimmers towards the axis of separation $\hat{\boldsymbol{r}}$. This interaction is typically short-range as well, but it is not included in our model. Finally, the third term is on the same form as the dipole term $\nu_2 \boldsymbol{u} \cdot \boldsymbol{p}^{\perp}$ in Eq. (29). This is easily seen by inserting the definition of the velocity field $\boldsymbol{u}^d(\boldsymbol{r}, \boldsymbol{\sigma}_j)$ from Eq. (28) so that

$$\nu_2 \boldsymbol{p}_i^{\perp} \cdot \boldsymbol{u}^d(\boldsymbol{r}, \boldsymbol{p}_j) = \frac{\nu_2 v_s \sigma}{2\pi |\boldsymbol{r}|^2} \boldsymbol{p}_i^{\perp} \cdot (2\hat{\boldsymbol{r}}\hat{\boldsymbol{r}} - \boldsymbol{I}) \cdot \boldsymbol{p}_j. \tag{33}$$

$\boldsymbol{p}_i^{\perp}$ and $\boldsymbol{p}_j$ can be interchanged since $(2\hat{\boldsymbol{r}}\hat{\boldsymbol{r}} - \boldsymbol{I})$ is symmetric. Thus we get that $C(r) = \nu_2 v_s \sigma / 2\pi |\boldsymbol{r}|^2$.

We note that the gradient term $\nu_1 \boldsymbol{p}^{\perp} \cdot (\nabla \boldsymbol{u}) \cdot \boldsymbol{p}$ in Eq. (29) does not fit with any of the terms in Eq. (32). This is due to the fact that this term of a higher-order moment than what was included in Eq. (31). By using that $\partial_i \hat{r}_j = \partial_j \hat{r}_i$ it is however quite straightforward to see that $\nabla \boldsymbol{u}^d$ is symmetrical. Consequently, we can write

$$\frac{\partial}{\partial \alpha_i} \left[\frac{\nu_1}{2} \boldsymbol{p}_i \cdot (\nabla \boldsymbol{u}(\boldsymbol{r}, \boldsymbol{p}_j)) \cdot \boldsymbol{p}_i \right] = \nu_1 \boldsymbol{p}_i^{\perp} \cdot (\nabla \boldsymbol{u}(\boldsymbol{r}, \boldsymbol{p}_j)) \cdot \boldsymbol{p}_i, \tag{34}$$

meaning that the expression within the brackets [ ] can be added to H_{eff}. We do not bother writing out the expression for $\nabla \boldsymbol{u}$ here, but it is clear that this term is of one order higher than the dipole-term in Eq. (33).

3.3 Complex notation

With all alignment interactions included equations of motion now read

$$\dot{\boldsymbol{r}}_i = v_s \boldsymbol{p}_i + \mu \sum_{j\neq i} \boldsymbol{u}^d(\boldsymbol{r}_i - \boldsymbol{r}_j, \boldsymbol{p}_j), \tag{35a}$$

$$\dot{\alpha}_i = \sum_{j\neq i} \left[\frac{\gamma}{|\boldsymbol{r}_i - \boldsymbol{r}_j|^{\zeta}} \boldsymbol{p}_i^{\perp} \cdot \boldsymbol{p}_j + \nu_1 \boldsymbol{p}_i^{\perp} \cdot (\nabla \boldsymbol{u}^d) \cdot \boldsymbol{p}_i + \nu_2 \boldsymbol{p}_i^{\perp} \cdot \boldsymbol{u}^d \right] \tag{35b}$$

for a particle at position $\boldsymbol{r}_i$ and with orientation $\boldsymbol{p}_i$, where $\boldsymbol{u}^d(\boldsymbol{r}, \boldsymbol{p}_j)$ is defined in Eq. (28). Inspired by Tsang and Kanso [69] we will now rewrite these equations in complex notation, introducing $z = x + \mathrm{i}y$ with the imaginary unit $\mathrm{i} = \sqrt{-1}$. We start by constructing the complex velocity field

$$\overline{w}^d(z|z_0, \alpha) = u_x^d(\boldsymbol{r}|\boldsymbol{r}_0, \boldsymbol{p}) - \mathrm{i}u_y^d(\boldsymbol{r}|\boldsymbol{r}_0, \boldsymbol{p}) = \frac{v_s\sigma}{2\pi}\frac{\mathrm{e}^{i\alpha}}{(z - z_0)^2}, \tag{36}$$

with $\overline{w}^d$ denoting the complex conjugate of w^d. This is in accordance with the general complex stream function $\phi(z) = m\mathrm{e}^{\mathrm{i}\alpha}/(z - z_0)$ for a dipole of strength m [80]. Thus, we see that $\dot{\overline{z}}_i = v_s\mathrm{e}^{-\mathrm{i}\alpha_i} + \mu\sum\overline{w}^d(z_i - z_j, \alpha_j)$.

Doing the alignment interactions in Eq. (35b) term by term, we first see that $\gamma|\boldsymbol{r}_i - \boldsymbol{r}_j|^{-\zeta}\boldsymbol{p}_i\perp\cdot\boldsymbol{p}_j$ is equal to $\gamma|z_i - z_j|^{-\zeta}\mathrm{Re}[\mathrm{i}\mathrm{e}^{\mathrm{i}(\alpha_i - \alpha_j)}]$. Re[...] denotes the real part of the expression within the brackets. The gradient term can be written out as

$$\nu_1\frac{v_s\sigma}{2\pi|\boldsymbol{r}|^3}\left[2\hat{r}_x\left(\hat{r}_x^2 - 3\hat{r}_y^2\right)\sin(2\alpha_i + \alpha_j) + 2\hat{r}_y\left(\hat{r}_y^2 - 3\hat{r}_x^2\right)\cos(2\alpha_i + \alpha_j)\right] \tag{37}$$

which in complex notation becomes

$$\nu_1\mathrm{Re}\left[\frac{\mathrm{d}\overline{w}^d}{\mathrm{d}z_i}(z_i - z_j, \alpha_j)\mathrm{i}\mathrm{e}^{2\mathrm{i}\alpha_i}\right]. \tag{38}$$

Similar to this we can show that the dipole term gives a contribution $\nu_2\mathrm{Re}\left[\overline{w}^d(z_i - z_j, \alpha_j)\mathrm{i}\mathrm{e}^{\mathrm{i}\alpha_i}\right]$ to $\dot{\alpha}_i$. We can now give the equations of motion as

$$\dot{\overline{z}}_i = v_s\mathrm{e}^{-\mathrm{i}\alpha_i} + \mu\overline{w}(z_i) + V_i, \tag{39a}$$

$$\dot{\alpha}_i = \mathrm{Re}\left[\nu_1\frac{\mathrm{d}\overline{w}(z_i)}{\mathrm{d}z_i}\mathrm{i}\mathrm{e}^{2\mathrm{i}\alpha_i} + \nu_2\overline{w}(z_i)\mathrm{i}\mathrm{e}^{\mathrm{i}\alpha_i} + \sum_{j\neq i}^{N}\frac{\gamma\mathrm{i}\mathrm{e}^{i(\alpha_i - \alpha_j)}}{|z_i - z_j|^\zeta}\right], \tag{39b}$$

where $\overline{w}(z_i) = \sum_{j\neq i}^{N}\overline{w}^d(z_i - z_j, \alpha_j)$ is the sum of the $N - 1$ dipolar fields created by the other swimmers. V_i is a repulsive force that accounts for steric interactions and prevents overlapping of particles.

3.4 Periodic boundary conditions

So far we have not considered the boundary conditions of our system, which naturally will influence the collective behaviour of the swimmers. We know that a circular domain with the model described exhibits some interesting collective behaviours [75], but we will focus on a system with doubly periodic boundary conditions. However, in Appendix A the equations of motion for a circular domain and a few resulting behaviours are presented. The periodic boundary conditions can effectively be seen as particles moving on a torus, but this also leads to changes in the velocity field of the fluid surrounding the particles. To account for this we introduce "image particles", copies of the real particles with the same orientation but placed outside of the domain. To do this Kanso and Tsang introduce the Weierstrass elliptic function $\rho(z|\omega_1, \omega_2)$ into the expression for the fluid velocity field so that $\overline{w}(z_i) = \sum_{j\neq i} v_s\sigma\mathrm{e}^{\mathrm{i}\alpha_j}\rho(z_i - z_j|\omega_1, \omega_2)/2\pi$. The elliptic Weierstrass function reads

$$\rho(z; \omega_1, \omega_2) = \frac{1}{z^2} + \sum_{k,l}\left(\frac{1}{(z - \Omega_{k,l})^2} - \frac{1}{\Omega_{k,l}^2}\right) \tag{40}$$

for a domain of lengths ω_1 and ω_2, with $\Omega_{k,l} \equiv \omega_1 k + \mathrm{i}l\omega_2$. In our case we choose a quadratic domain of length L so that $\omega_1 = \omega_2 = L$. It can then be shown that if the sum is symmetric over k and l, i.e. both k and l sum from $-N_d$ to N_d for some integer N_d, the second term in the sum will add up to 0. Thus we can write the velocity field experienced by a swimmer at z_i as

$$\overline{w}(z_i) = \sum_{j\neq i}^{N}\frac{v_s\sigma\mathrm{e}^{\mathrm{i}\alpha_j}}{2\pi}\sum_{k,l}\frac{1}{(z_i - z_j - \Omega_{k,l})^2}, \tag{41}$$

where the summing indices $k, l \in \mathbb{Z}$ in principle sum from $-\infty$ to ∞. We can now explicitly write the equations of motion for a swimmer i,

$$\dot{z}_i = v_s \mathrm{e}^{-\mathrm{i}\alpha_i} + \mu \frac{v_s \sigma}{2\pi} \sum_{j \neq i}^{N} \sum_{k,l} \frac{\mathrm{e}^{\mathrm{i}\alpha_j}}{(z_i - z_j - \Omega_{k,l})^2} + V_i, \tag{42a}$$

$$\dot{\alpha}_i = \sum_{j \neq i}^{N} \sum_{k,l} \mathrm{Re} \left[\nu_1 \frac{v_s \sigma}{2\pi} \frac{-2\mathrm{i}\mathrm{e}^{2\mathrm{i}\alpha_i} \mathrm{e}^{\mathrm{i}\alpha_j}}{(z_i - z_j - \Omega_{k,l})^3} + \nu_2 \frac{v_s \sigma}{2\pi} \frac{\mathrm{i}\mathrm{e}^{\mathrm{i}\alpha_i} \mathrm{e}^{\mathrm{i}\alpha_j}}{(z_i - z_j - \Omega_{k,l})^2} + \frac{\gamma \mathrm{i}\mathrm{e}^{i(\alpha_i - \alpha_j)}}{|z_i - z_j - \Omega_{k,l}|^{\zeta}} \right] \tag{42b}$$

in a population of N identical swimmers in a Hele-Shaw cell with doubly periodic boundary conditions.

4 Simulation Methods

Before doing numerical simulations of any physical system, it is natural to express the relevant variables in terms of some characteristic parameters of the system. On one hand this is done to avoid very large or very small numbers during calculations, which can decrease the accuracy of the results. On the other, it makes the results more general as there will be fewer parameters to vary when investigating the properties of the system. This makes it easier to compare results obtained by different methods.

To express Eqs. (42a) and (42b) in reduced units we want to find a characteristic length and time. As we know, σ is twice the particle area for circular particles. $r_0 = \sqrt{\sigma/2\pi}$ therefore appears as the logical characteristic length, with $2r_0$ describing the size of a swimmer. With this we can now define $\tau = r_0/v_s$, the time it takes an unaffected swimmer to swim half its body length, as the characteristic time.

Now if we let $z \to z' = z/r_0$ and $t \to t' = t/\tau$ in Eqs. (42a) and (42b) we obtain

$$\frac{\mathrm{d}\overline{z'_i}}{\mathrm{d}t'} = \mathrm{e}^{-\mathrm{i}\alpha_i} + \mu \sum_{j\neq i}^{N} \sum_{k,l} \frac{\mathrm{e}^{\mathrm{i}\alpha_j}}{(z'_i - z'_j - \Omega'_{k,l})^2} + V'(z'_i), \tag{43a}$$

$$\frac{\mathrm{d}\alpha_n}{\mathrm{d}t'} = \sum_{i\neq n}^{N} \sum_{k,l} \mathrm{Re}\left[\nu_1 \frac{-2\mathrm{i}\mathrm{e}^{2\mathrm{i}\alpha_n}\mathrm{e}^{\mathrm{i}\alpha_i}}{(z'_n - z'_i - \Omega'_{k,l})^3} + \nu_2 \frac{\mathrm{i}\mathrm{e}^{\mathrm{i}\alpha_n}\mathrm{e}^{\mathrm{i}\alpha_i}}{(z'_n - z'_i - \Omega'_{k,l})^2} + \gamma \frac{\mathrm{i}\mathrm{e}^{i(\alpha_i - \alpha_j)}}{|z'_i - z'_j - \Omega'_{k,l}|^{\zeta}}\right] \tag{43b}$$

with only non-dimensional variables and parameters. It should be pointed out that the flow alignment coefficient ν_2 is now modified by a factor r_0 compared to what is used in Eq. (42b). It is now unitless and defined as $\nu_2 = (r_0/a)(\mu_2 - \mu_1)$ as opposed to Eq. (27c), and thus it also accounts for the anisotropy of the swimmers. γ is also redefined, $\gamma \to r_0^{1+\zeta}\gamma/v_s$, to keep the dimensions straight. We now see that the parameters σ and v_s have been normalized out of the equations of motion.

Eqs. (43a) and (43b) leaves us with only 5 parameters to vary for a system of given size N, namely the mobility coefficient μ, the flow alignment coefficients ν_1, ν_2, the Lennard-Jones strength ϵ/v_s and the density $\rho = N/L^2$.

4.1 Repulsive force

We are yet to describe the repulsive force $V(z_i)$ responsible for the collision mechanisms between the particles. When introduced it gives the particles a finite 2D volume. A typical model for this purpose is the Lennard-Jones potential

$$U_{LJ}(r) = 4\epsilon\left[\left(\frac{\xi}{r}\right)^{12} - \left(\frac{\xi}{r}\right)^{6}\right], \tag{44}$$

where ϵ expresses the strength of the potential and ξ the distance where the potential is zero. For our systems we are not interested in the attractive part of this potential. Thus, one possibility is to simply construct a force from particle j on i

$$V_{\text{LJ, rep}} = 4\epsilon\left(\frac{\xi}{|z_i - z_j|}\right)^{13} \frac{\overline{z}_i - \overline{z}_j}{|z_i - z_j|} \tag{45}$$

from the repulsive part of the potential. The second fraction in the sum is there to give the force the appropriate direction, and it is conjugated since we are looking at $\dot{\overline{z}}_i$ in Eq. (39a). This is the approach of Tsang and Kanso [69, 75]. We see that the range of this interaction is very short, which ensures that the hydrodynamic interactions in far-field are not affected. Because of this short range, it is natural to apply a cut off for this interaction, meaning that we truncate the interactions above a certain distance Δz. This is an effective way of reducing computation time.

The truncation of the Lennard-Jones force will lead to a discontinuity in the force. This is unphysical and may create fortuitous effects, in addition to adding an instability to the numerics. A common method to overcome this issue is by the Weeks-Chandler-Andersen potential and the related force [81]. Here the attractive part of the potential is not removed, instead a cutoff the distance $r_c = 2^{1/6}\xi$ where the Lennard-Jones force is zero, i.e. $\mathrm{d}U_{LJ}(r_c)/\mathrm{d}r = 0$, is applied. This makes the force continuous, but its derivative is still discontinuous at $r = r_c$. Following Ref. [82], we therefore introduce a final linear term to the potential

$$U_{\text{rep}}(r) = \begin{cases} 4\epsilon\left[\left(\dfrac{\xi}{r}\right)^{12} - \left(\dfrac{\xi}{r}\right)^{6}\right] - f_s r + \epsilon_s, & r \leq r_c \\ 0, & r > r_c \end{cases}, \tag{46}$$

where the force shift is $f_s = \frac{252}{169}2^{5/6}(7/13)^{1/6}\epsilon/\xi \approx 2.40\epsilon/\xi$ and the potential shift is $\epsilon_s = 49/13\epsilon$. We have now redefined $r_c = (26/7)^{1/6}\xi$ so that $\frac{\mathrm{d}}{\mathrm{d}r}U_{\text{rep}}(r_c) = \frac{\mathrm{d}^2}{\mathrm{d}r^2}U_{\text{rep}}(r_c) = 0$.

Having defined the repulsive potential, we can now write the complex force as

$$V_{\text{rep}}(z_{ij}) = \left(4\epsilon\left[\frac{12}{|z_{ij}|}\left(\frac{\xi}{|z_{ij}|}\right)^{12} - \frac{6}{|z_{ij}|}\left(\frac{\xi}{|z_{ij}|}\right)^{6}\right] + f_s\right)\frac{\overline{z_{ij}}}{|z_{ij}|} \tag{47}$$

for $|z_{ij}| = |z_i - z_j| \leq r_c$. To fit this force into Eq. (43a) it is natural to choose ϵ and ξ in units of v_s and r_0 respectively. If we were using the repulsive Lennard-Jones force in Eq. (45) it would be natural to choose $\xi = 2r_0$ and $\epsilon = v_s$. This would give an effective particle diameter of $2r_0$ and a force comparable to the velocity v_s. However, this would give an effective diameter larger than $2r_0$ with V_{rep}, due to the force shift f_s. This is also illustrated in Figure 10. We therefore want to choose ϵ and ξ so that $V_{\text{rep}}(|z_{ij}| = 2, \epsilon, \xi) = V_{\text{LJ, rep}}(|z_{ij}| = 2, \epsilon = 1, \xi = 2)$. Two possible alternatives are $\epsilon = 1, \xi \approx 1.871$ and $\epsilon \approx 0.303, \xi = 2.0$. In Figure 10 we see the force V_{rep} with these parameter sets as a function of the separation $r = |z_{ij}|$ compared to the conventional Lennard-Jones force $V_{LJ} = -\mathrm{d}U_{LJ}/\mathrm{d}r$ and the pure repulsive force $V_{\text{LJ,rep}}$. At $r = 2$ we see that $V_{\text{LJ,rep}}$ equals V_{rep} with the parameter sets given above. However, we also see that $V_{\text{rep}}(r, \epsilon \approx 0.303, \xi \approx 1.871)$ behaves quite similar to $V_{LJ}(r, \epsilon = 1, \xi = 2)$ for $r < 2.0$. Thus we choose $\epsilon = 0.303, \xi = 1.871$ in our model. Thus, the force term in Eq. (43a) is given by

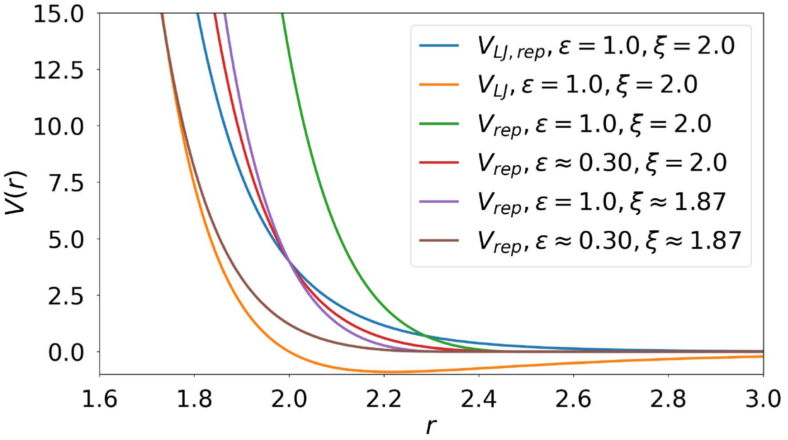

Figure 10: A comparison of the conventional Lennard-Jones force V_{LJ}, the repulsive part part of this force, $V_{\text{LJ,rep}}$, and a modified Weeks-Chandler-Andersen force V_{rep} given in Eq. (47). V_{rep} is plotted with different values for the potential strength ϵ and characteristic length ξ.

$$V'(z_i') = \sum_{j\neq i}^{N} V_{\text{rep}}(z_i - z_j, \epsilon = 0.303, \xi = 1.870), \tag{48}$$

with V_{rep} defined in Eq. (47).

It should be noted that we used the term ”force” in this discussion, while physically this is a velocity since we are looking at $\mathrm{d}z/\mathrm{d}t$ and not $\mathrm{d}^2z/\mathrm{d}t^2$. However, including an equation for $\mathrm{d}^2z/\mathrm{d}t^2$ would increase the numerical complexity and computation time. As the main purpose of this interaction is to prevent overlapping of particles we are therefore satisfied with including the term in $\mathrm{d}z/\mathrm{d}t$. Another possibility would be to introduce a parameter ε that scales with the size of the swimmer so that $\overline{w}^d$ scales as $(z - z_0 + \varepsilon)^{-2}$ instead of $(z - z_0)^{-2}$ [71, 83]. While being a computationally simpler and less demanding approach, this can also introduce a weak, artificial "fluid compressibility" near the swimmers.

4.2 Numerical integrator

Initially the numerical simulations were done with the Euler method. Given a set of positions and angles at time t, the positions and angles at time $t+\delta t$ are approximated by $z(t+\delta t) \approx z(t)+z'(t)\delta t$ and $\alpha(t+\delta t) \approx \alpha(t) + \alpha'(t)\delta t$. The Euler method was chosen because it is easy to implement and computationally fast in the sense that one only needs to calculate $z'(t)$ once for each timestep. The drawback of the Euler method is of course the errors it produces compared to more refined methods. The local truncation error of the method is of order δt^2. How this error proceeds over time is hard to estimate, as our system is chaotic and we lack an analytical solution to compare with.

To improve the numerical precision and stability, the Euler method was replaced by the Runge-Kutta method of fourth order. We now define the derivatives as $\dot{z}_i = f_i(\{z_j\}_{j=1}^N, \{\alpha_j\}_{j=1}^N)$ and $\dot{\alpha}_i = g_i(\{z_j\}_{j=1}^N, \{\alpha_j\}_{j=1}^N)$. The Runge-Kutta approximation is then

$$z_i(t+\delta t) \approx z_i(t) + \frac{1}{6}\delta t(k_{i,1} + 2k_{i,2} + 2k_{i,3} + k_{i,4}), \tag{49}$$

$$\alpha_i(t+\delta t) \approx \alpha_i(t) + \frac{1}{6}\delta t(l_{i,1} + 2l_{i,2} + 2l_{i,3} + l_{i,4}) \tag{50}$$

where

$$\begin{aligned}
k_{j,1} &= f_j\left(\{z_j(t)\}, \{\alpha_j(t)\}\right), & l_{j,1} &= g_j\left(\{z_j(t)\}, \{\alpha_j(t)\}\right), \\
k_{j,2} &= f_j\left(\{z_j(t) + \delta t\frac{k_{j,1}}{2}\}, \{\alpha_j(t) + \delta t\frac{l_{j,1}}{2}\}\right), & l_{j,2} &= g_j\left(\{z_j(t) + \delta t\frac{k_{j,1}}{2}\}, \{\alpha_j(t) + \delta t\frac{l_{j,1}}{2}\}\right), \\
k_{j,3} &= f_j\left(\{z_j(t) + \delta t\frac{k_{j,2}}{2}\}, \{\alpha_j(t) + \delta t\frac{l_{j,2}}{2}\}\right), & l_{j,3} &= g_j\left(\{z_j(t) + \delta t\frac{k_{j,2}}{2}\}, \{\alpha_j(t) + \delta t\frac{l_{j,2}}{2}\}\right), \\
k_{j,4} &= f_j\left(\{z_j(t) + \delta t k_{j,3}\}, \{\alpha_j(t) + \delta t l_{j,3}\}\right), & l_{j,4} &= g_j\left(\{z_j(t) + \delta t k_{j,3}\}, \{\alpha_j(t) + \delta t l_{j,3}\}\right).
\end{aligned}$$

Thus this method takes four different slopes into account for each timestep. This gives a local truncation error of order δt^5, i.e. three orders higher than the Euler method. With the Euler method we found that $\delta t = 0.005\tau$ gave a sufficient precision, but with the fourth order Runge-Kutta method we can now increase this to $\delta t = 0.02$. This will give approximately the same computational cost, but the local truncation error will be $\sim 10^{-4}$ smaller than what we had for the Euler method.

4.3 Considerations on periodic boundary conditions

As one may see from Eqs. (43a) and (43b), the main computational challenge for this system is the summation over k and l accounting for the periodic boundary conditions. In principle these sums should run from $-\infty$ to ∞ to ensure that we are looking at a bulk system with no boundary effects. This is obviously not possible when doing numerical calculations. Instead we have to choose a finite integer N_{img} so that k, l run from $-N_{\text{img}}$ to N_{img}. In practice this means that when we compute the force from particle j on particle i, we also need to compute the force from $(2N_{\text{img}} + 1)^2 - 1$ images of j. Since the hydrodynamic interactions in our model scale as $\sim 1/r^2$ we say that they are weakly long ranged. We can approximate the sum of contributions from all swimmers within a distance r as $\int r^{-2}\mathrm{d}r^2 \sim \log r$ meaning that the sum is not convergent. Because of this one should avoid setting a cut-off distance and truncate contributions above this. It also means that we should take good care when choosing N_{img}.

So far the alignment interaction involving γ has also been integrated into the summation over k, l. However, as this interaction will only be considered as short-range it will not be affected to any significant degree by the periodic boundary conditions. The only modification it leads to is that when computing the contribution from particle j to $\dot{\alpha}_i$ this will be done only with the $\Omega_{k,l}$ that minimizes the distance $|z_i - z_{j\Omega k,l}|$. Thus, we find the image of particle j closest to i and compute the interaction therefrom, as illustrated in Figure 12. Furthermore, a cutoff will be applied on this interaction, truncating contributions from particles at a certain distance.

Figure 11 displays the relative change in amplitude and direction of the force on a particle as a function of N_{img}. The "force" here is the second term in Eq. (43a). We see that the change decays linearly in the log-log plot, and by comparison it can be showed that it goes as $\sim 0.01 N_{\text{img}}^{-4}$. For $N_{\text{img}} = 200$ we get that both $\Delta|\boldsymbol{F}|, \Delta\theta < 10^{-10}$ which should be satisfactory, so this is used in all simulations that follows. Since we know the decay in the relative change in this area we can estimate the additional contributions that would come from $N_{\text{img}} > 200$ as $0.01 \sum_{n=200}^{\infty} n^{-4} \approx 10^{-10}$. This is close to the unavoidable error that occurs when doing calculations and storing data digitally with finite memory. We therefore accept this truncation error of the hydrodynamic interactions.

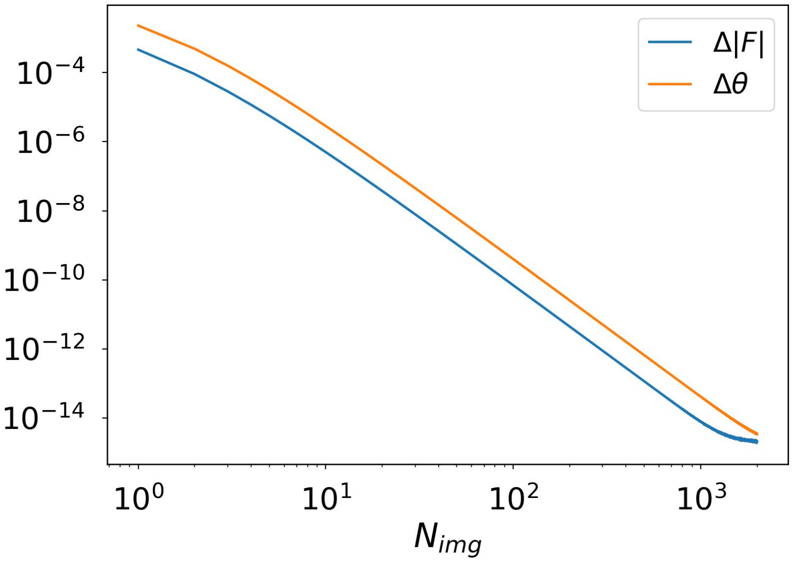

Figure 11: Log-log plot of the relative change in force $\boldsymbol{F}$ on a swimmer in a system of 1000 swimmers with density $\rho = 0.1$, as a function of N_{img}. The change in the absolute value of the force is computed as $\Delta|\boldsymbol{F}|(N_{\text{img}}) = |\boldsymbol{F}(N_{\text{img}}) - \boldsymbol{F}(N_{\text{img}}+1)| / |\boldsymbol{F}(N_{\text{img}}+1)|$ and similarly for the change in the direction $\Delta\theta(N_{\text{img}})$ of the force. The plot is an average over 500 simulations where positions and angles are randomly chosen from uniform distributions.

4.4 Accelerated algorithm

We have now seen how our model is computationally challenging compared to for example the Vicsek model, which only considers interactions over a finite distance r. With periodic boundary conditions a finite number of copies of the system is therefore enough to simulate the bulk system without truncation error. In addition, the finite interactions make it easier to increase the system size. Say that we have N particles in a system. Then the hydrodynamic interactions would require $\sim N^2$ calculations, while the Vicsek model only would require $\sim N$. Lastly, the actual computation of the interaction forces is more requiring in our case, but this is of minor importance. Consequently, a system with hydrodynamic interactions is more challenging to simulate on large scales than what is the case for the Vicsek model.

Having shown that it is reasonable to set $N_{\text{img}} = 200$, it is still a formidable task to sum both k and l from -200 to 200, $N(N-1)$ times for each time step. To reduce the number of computations needed an accelerated algorithm is introduced, inspired by Lefauve and Saintillan [83]. The algorithm constructed here will describe the computation of the second term in Eq. (43a), but is also used for the two terms in Eq. (43b). We start by observing that when we are to compute the force from particle i and its images on particle n, there are 9 candidate images of i to be closest to n. This this minimum distance is denoted $\boldsymbol{R}_{n,i}^{\text{min}}$, and illustrated in Figure 12. Observe that $\boldsymbol{R}_{n,i}^{\text{min}}$ must be within a square of length L centered at 0, $\boldsymbol{R}_{n,i}^{\text{min}} \in ([-L/2, L/2] \times [-L/2, L/2])$.

Thus, the force can be split as

$$\begin{aligned}\sum_{i\neq n}^{N} \mathrm{e}^{\mathrm{i}\alpha_i} \sum_{k,l} (z_n - z_i - \Omega_{k,l})^{-2} &= \sum_{i\neq n}^{N} \mathrm{e}^{\mathrm{i}\alpha_i} \left[F(z_{n,i}^{\min}) + \sum_{\substack{k=-N_{\mathrm{img}} \\ (k,l)\neq(0,0)}}^{N_{\mathrm{img}}} \sum_{l=-N_{\mathrm{img}}}^{N_{\mathrm{img}}} F(z_{n,i}^{\min} + \Omega_{k,l}) \right] \\ &= \sum_{i\neq n}^{N} \mathrm{e}^{\mathrm{i}\alpha_i} \left[F(z_{n,i}^{\min}) + F^{\mathrm{far}}(z_{n,i}^{\min}) \right]\end{aligned} \tag{51}$$

with $F(z) = z^{-2}$ and $z_{n,i}^{\min}$ being the complex analog of $\boldsymbol{R}_{n,i}^{\min}$. $F^{\mathrm{far}}(z_{n,i}^{\min})$ is defined as the double sum on the right hand side of the upper equation. Note that one should in principle calculate $F^{\mathrm{far}}(z_{n,i}^{\min})$ for $i = n$ as well, as particle n also interacts with its images, but these contributions add up to 0.

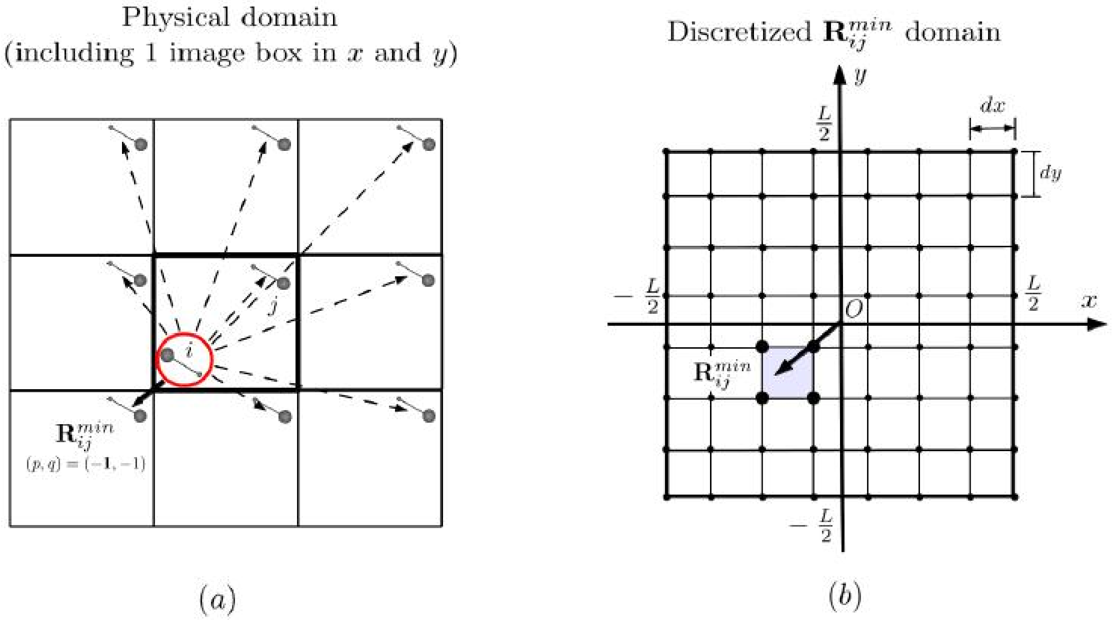

Figure 12: When computing the force acting on particle i from particle j, one must also consider the images of j due to periodic boundary conditions. The idea behind the accelerated algorithm is to compute the force $\boldsymbol{F}(\boldsymbol{R}_{ij}^{\min})$ from the image of j closest to i directly. Then the smaller force $\boldsymbol{F}^{\mathrm{far}}(\boldsymbol{R}_{ij}^{\min})$ from the other images of j is approximated by precalculated values on a discretized domain. *a)* shows that there are 9 candidate images of j to be closest to i, and that the closest one is positioned at $\boldsymbol{R}_{ij}^{\min}$ with respect to i. *b)* $\boldsymbol{R}_{ij}^{\min}$ will be in the domain $([-L/2, L/2] \times [-L/2, L/2])$ which can be discretized to compute $\boldsymbol{F}^{\mathrm{far}}(\boldsymbol{R}_{ij}^{\min})$ on points separated by $\mathrm{d}x = \mathrm{d}y$. During simulations $\boldsymbol{F}^{\mathrm{far}}(\boldsymbol{R}_{ij}^{\min})$ will approximated by interpolation between these points.

Source: Adrien Lefauve and David Saintillan [83]

By the same calculations as in Figure 11 we find that adding contributions from the first 8 images, i.e. when $N_{\mathrm{img}} = 1$, gives a mean change of about 2.2% to the force computed with only 1 image ($N_{\mathrm{img}} = 0$). Then it is not even taken into consideration that this image may not be the closest one. This illustrates the importance of getting accurate values for $F(z_{n,i}^{\min})$ compared to $F^{\mathrm{far}}(z_{n,i}^{\min})$.

Since $F(z_{n,i}^{\min}) \gg F^{\mathrm{far}}(z_{n,i}^{\min})$ we will approximate $F^{\mathrm{far}}(z_{n,i}^{\min})$ by values on a precalculated grid rather than calculate it exactly at each timestep. Since $\boldsymbol{R}_{n,i}^{\min} \in ([-L/2, L/2] \times [-L/2, L/2])$ we can set up a finite number of grid points within this square, as displayed in Figure 12. Having N_{grid} points in both x- and y direction, the points are separated by distance $\delta r = L/N_{\mathrm{grid}}$. $F^{\mathrm{far}}(z_{n,i}^{\min})$

is thus calculated on these points before the simulation starts. Hence, to compute a term i in the sum in Eq. (51) there are 4 steps to be made: (i) Find the image of i closest to n and thereby $z^{\text{min}}_{n,i}$. (ii) Compute $F(z^{\text{min}}_{n,i})$ directly. (iii) Approximate $F^{\text{far}}(z^{\text{min}}_{n,i})$ by bilinear interpolation of the four grid points closest to $z^{\text{min}}_{n,i}$. (iv) Multiply with $\mathrm{e}^{\mathrm{i}\alpha_i}$.

This algorithm reduces a sum over $(2N_{\text{img}} + 1)^2 - 1$ interactions to a simple bilinear interpolation. With $N_{\text{img}} = 200$ this implies that the computation time is reduced by a factor $1.6 \cdot 10^5$. The error induced by the bilinear approximation can be estimated as $\delta r^2 |\partial^2 F^{\text{far}}/\partial z^2| \leq \delta r^2 \sum_n^\infty (Ln)^{-4} \approx (N_{\text{grid}} L)^{-2}$ where L is given in units of r_0 as discussed earlier. This is the error in $F^{\text{far}}(z^{\text{min}}_{n,i})$, which only contributes a few percent to the total velocity induced by the other particles. Thus, this approximation is considered to be good in the sense that it produces relatively small errors and the time reduction is significant.

4.5 Steady state

When searching for general characteristics of the system, we want to ensure that we are looking at a steady state. This applies to all studies of dynamical systems. In the steady state the system should be independent of its initial configuration and not display any net development in its macroscopic properties.

From the effective angular potential in Eq. (31) we may define an elastic potential

$$H_{\text{el}} = -\sum_{i=1}^{N} \sum_{j \neq i}^{N} \frac{\gamma \boldsymbol{p}_j \cdot \boldsymbol{p}_i}{|\boldsymbol{r}_i - \boldsymbol{r}_j|^5} \tag{52}$$

indicating how aligned the particles of a system are with its neighbors. Here we have set $\zeta = 5$, which is also the case for the results we will present. In Figure 13 we have plotted the time development of this potential per particle for two systems which we will discuss in section 5. The potential is computed by dimensionless variables and the time is given in units of the characteristic time τ. We see that both curves quickly develops towards a mean value which they then fluctuate around. By further inspection we find that at $t = 100\tau$ both curves have reached their mean values.

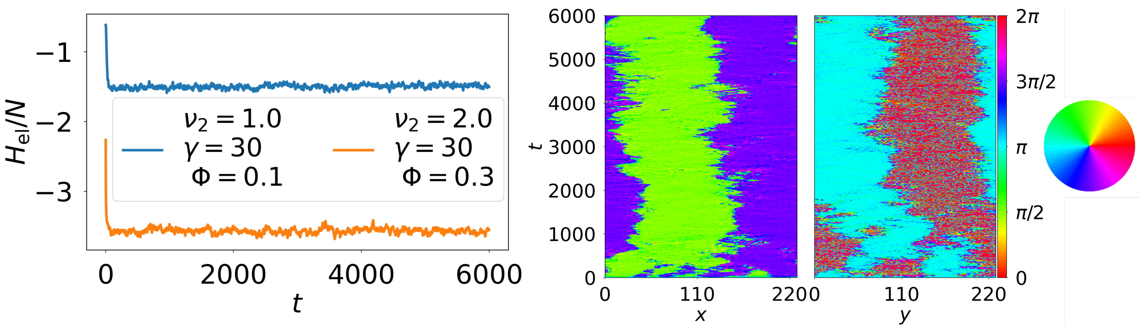

Figure 13: *Left:* Elastic potential H_{el} per particle for two systems with $N = 5000$ particles and different flow alignment coefficients γ, ν_2 and area fractions Φ. Plotted as functions of time t. *Left:* Time development of the average orientation of line segments along the x and y axis respectively, for the system represented by the orange curve in the left plot. The colors indicate the orientation with respect to the x axis, as illustrated by the circle.

The plots to the right show the time development of the average orientation within line segments at the x and y axis respectively. In contrast to the elastic potential which depends on the microscopical behaviour, this gives an indication of the global development of the system. We see that after 2000 time units the configuration is relatively stable. We also note that the system appears to favor orientation in the x and y directions, or along the diagonals. This is confirmed by multiple simulations and is a typical artifact of the periodic boundary conditions [84].

Finally, we inspect the development of the energy spectra $E(k)$ for a system with $N = 1500$ particles and otherwise equivalent to that represented by the orange curve in Figure 13. In Figure 14 we show plots of $E(k)$ at four different times for two different initial configurations. We will come back to the computation of these spectra in the next section. We see that the two configurations initially display quite different spectra, but from $t = 100\tau$ they are very similar. We see that there are some variations at small k, i.e. long length scales. Fluctuations on large scales are typically more long-lived so we expect that averages over longer time-periods are needed for these to vanish.

Based on these results and numerous other simulations which we do not fit in here, we expect all systems to be in a steady state after a couple of thousand time units. Unless stated otherwise, the results we will present are based on simulations over 6000τ, where only the last 3000τ are used to compute the relevant sizes.

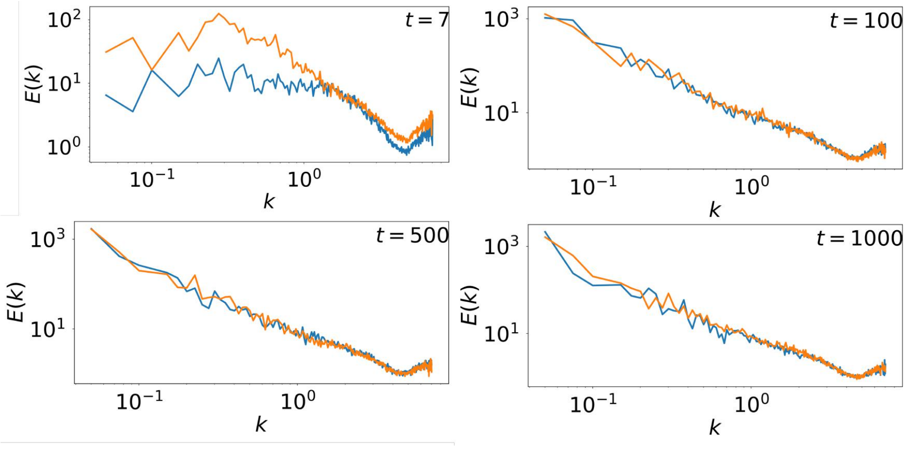

Figure 14: The computed energy spectra $E(k)$ of two systems with equal parameters but different initial configurations. To see the time development the spectra are plotted at four different times t.

4.6 Computation of energy spectra

In subsection 2.2 we saw that we may define the energy spectrum $E(k)$ by two different means. One by use of the Wiener-Khinchin theorem in Eq. (8) where the Fourier transform of the 2D velocity correlation function $R(\boldsymbol{r})$ is computed, and the other by direct computation of the Fourier transform the turbulent velocity field $\boldsymbol{u}' = \boldsymbol{u} - \langle \boldsymbol{u} \rangle$ in Eq. (14). In both cases we first interpolate the particle velocities onto a fine grid to obtain the velocity field $\boldsymbol{u}$. A comparison of the two methods for two systems is shown in Figure 14. For small k we see that the behaviour of the is very similar, but as k increases we see that the Wiener-Khinchin method collapses. Thus it fails to capture the small-scale behaviours of the system. We know that this method is based on continuum theory for infinite systems, and this may explain why it collapses in a discrete, finite system with periodic boundary conditions. We will therefore use the direct Fourier transform method to present results from the system. This is done by using a fast Fourier transform algorithm to find the 2D functions $\hat{u}'_x(k_x, k_y)$ and $\hat{u}'_y(k_x, k_y)$. The square absolute values of these are then added. To obtain the energy spectra we then compute the angular average of this 2D spectra for given wavenumbers $k = |\boldsymbol{k}|$, and multiply by k. This gives an energy spectrum as defined in Eq. (14).

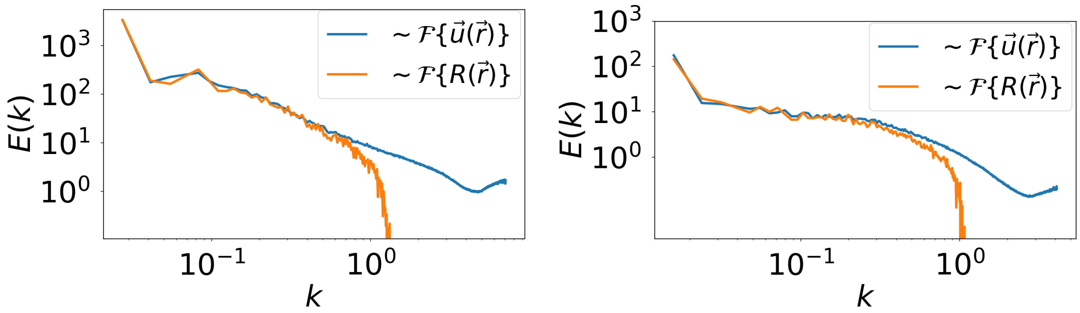

Figure 15: Comparison of the two methods to calculate the energy spectra. One using a direct Fourier transform $\mathcal{F}$ of the turbulent velocity field $\boldsymbol{u}'$, and the other via the 2D velocity correlation function $R(\boldsymbol{r})$. The two plots indicate the two systems to the left in Figure 13.

5 Results and Discussion

From the reduced equations of motion in Eq. (43) we see that there are 5 possible parameters that can be varied: The mobility coefficient μ, the three flow alignment coefficients ν_1, ν_2 and γ and the exponent ζ. In addition we have the density ρ and the number of particles N. Instead of using the density ρ we will refer to the area fraction, which is $\Phi = \pi\rho$ for circular particles of radius 1. Bear in mind that all lengths in this section will be given in units of r_0, all times in τ and all velocities in v_s.

We have not observed any distinct impact on the global dynamics from the mobility coefficient μ. As in Ref. [69], we will therefore only operate with $\mu = 1/2$. Unless stated otherwise, we have also chosen the exponent $\zeta = 5$. This value is somewhat arbitrary, but it ensures that the alignment interaction without introducing numerical instabilities. We are mainly interested in the competition between the deordering ν_2-term and the ordering γ-term at different area fractions. Thus we will present results where $\nu_1 = 0$, and vary γ, ν_2 and the area fraction Φ. For clarity, we restate the dimensionless equations of motion,

$$\begin{aligned}\frac{\mathrm{d}\overline{z_i'}}{\mathrm{d}t} =& \mathrm{e}^{-\mathrm{i}\alpha_i} + \frac{1}{2}\overline{\omega}'(z_i') + V'(z_i'),\\ \frac{\mathrm{d}\alpha_n}{\mathrm{d}t'} =& \mathrm{Re}\left[\nu_2\overline{\omega}'(z_i') + \gamma\frac{\mathrm{i}\mathrm{e}^{i(\alpha_i-\alpha_j)}}{|z_i'-z_j'|^5}\right]\end{aligned}$$

which we will be studying. To give an intuition on the system we are looking at, Figure 16 shows a snapshot of $N = 5000$ particles with flow alignment coefficients $\nu_2 = 2.0, \gamma = 30.0$ and area fraction $\Phi = 0.3$. The colors indicate the orientation α of the particles, while the arrows indicate their velocity $\boldsymbol{v}$. In most cases the velocity is almost parallel to the orientation vector. We see that there are large-scale unicolored areas indicating a polar order. In the zoom-in we observe that in the most dense areas the particles seem to form structures reminiscent of an hexagonal lattice.

In Figure 16 the stream function ψ of the system is also plotted. ψ is defined by $u_x = \partial\psi/\partial y$ and $u_y = -\partial\psi/\partial x$. To compute ψ the particle velocities are first interpolated onto a fine grid and averaged over 10 time steps τ to obtain a velocity field $\boldsymbol{u}$. By approximating the derivatives by finite differences we obtain an iteration scheme for ψ. While the snapshot in Figure 16 pleasingly illustrates long-range order in the system, the stream function gives a more intuitive picture of the particle motions. The system actually seems to consist of two large-scale, counter-rotating vortices. One positioned near the center of the system and the other close to the upper left corner. We also see that there are a few small-scale circulations. This pattern is very similar to the observations of Alert et. al. for an active nematic system, as shown in Figure 4.

5.1 System displaying active turbulence, $\nu_2 = 2.0$, $\gamma = 30.0$, $\Phi = 0.3$

The main result we can report from this work is the discovery of active turbulence in a system of confined, self-propelled microswimmers with hydrodynamic interactions. This is legitimized on the grounds of non-Gaussian broadening of the probability distribution functions for velocity increments, power law behaviour of energy spectra and superdiffusive behaviour of the particles within a given range of scales. We emphasize that our model contains no noise term, in contrast to many microscopic models of active polar systems [53, 60, 63, 71, 85, 86]. This is of interest because when a characteristic length scale takes place in a system it is due to a competition between ordering and disordering mechanisms. In our case the disordering mechanism is the hydrodynamic interactions that lead to non-linear effects. Similarly for high-Re flows the chaotic behaviour is explained by the non-linear terms in the Navier-Stokes equation.

A typical example of a system displaying active turbulence is the one plotted in Figure 16 where $\nu_2 = 2.0, \gamma = 30.0$ and $\Phi = 0.3$. In Figure 17 we see the trajectories of three representative particles with respect to the background flow $\langle\boldsymbol{v}\rangle(t)$ from this system. From these trajectories it is clear that we have a characteristic length scale in form of a vortex size in our system, which we also recognize from the stream function ψ in Figure 16. These trajectories are reminiscent of Lévy walks, which are characterized by short-range movement over time interrupted by irregular long-range motions in some direction [87]. This behaviour is super-diffusive and thus in contrast to for example Brownian motion. Lévy walks are observed in a wide range of biological systems

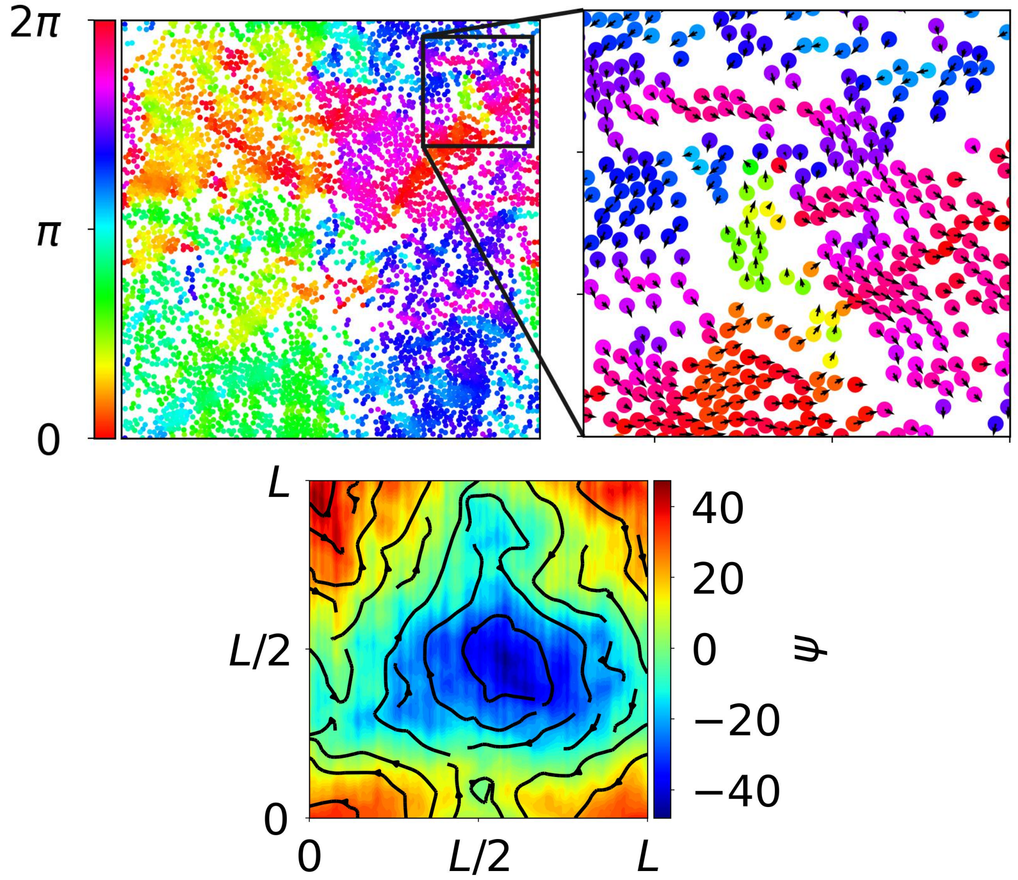

Figure 16: Snapshot of a system with $N = 5000$ particles, flow alignement coefficients $\nu_2 = 2.0$ and $\gamma = 30.0$, and area fraction $\Phi = 0.3$. In the upper plot both the positions of the particles and their radii are plotted in units of r_0, so that interparticle distances are comparable to the particle size. The color of each particle represents its orientation α with respect to the horizontal axis. In the zoomed area the arrows indicate the strength and direction of the velocities of the particles. In the lower plot the stream function ψ is plotted. The lines with arrows indicate some of the large scale streamlines of the system. The system size is $L \approx 229 r_0$.

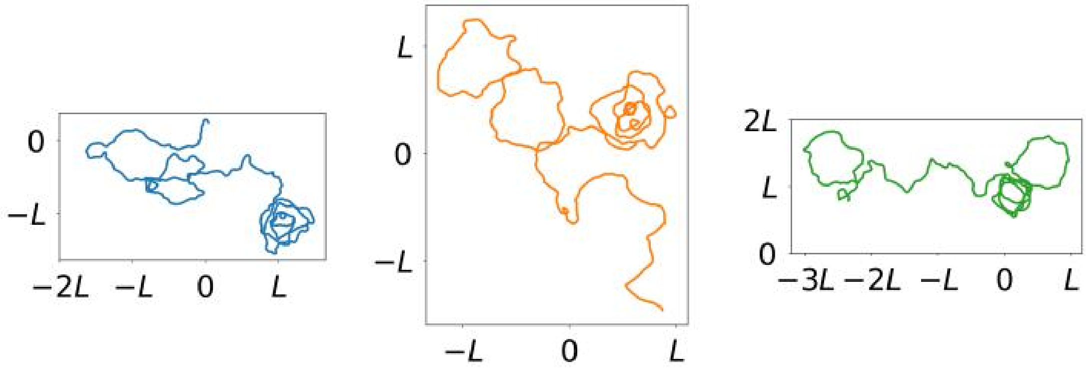

Figure 17: The trajectories of three particles with respect the background flow, in the system with $N = 5000$ particles where $\gamma = 30.0, \nu_2 = 2.0$ and $\Phi = 0.3$. This is found by subtracting the average displacement $\langle v \rangle \delta t$ at each timestep. The particles are tracked over 3000 time units τ. If the particles leave the domain $[0, L] \times [0, L]$, the trajectories are plotted so that we see their further movement instead of reappearing on the other side of the domain. We see that the particles alternate between moving relatively straight and being caught in a vortex-like structure.

[88–90]. The system is further presented in Figure 18. In the streamline plot of the system we can spot the appearance of transient vortices and directional correlations on different length scales. The center vortex we observed from the stream function is clearly visible here. We can also see the formation of more or less unidirectional flocks of different sizes within the system. This is also illustrated in the plot of the vorticity field $\omega = \partial_x u_y - \partial_y u_x$, where $\boldsymbol{u}$ is the velocity field. We see sharp, unicolored areas of different sizes indicating spatial fluctuations in velocity strength and direction. Furthermore the directional plot of $\boldsymbol{u}$ shows that there are global scale correlations and fluctuations in the direction of the velocity field. Note that we use $\boldsymbol{u}$ when we talk about the velocity field that is interpolated onto a grid, while $\boldsymbol{v}_i$ are the velocities of the individual particles.

In Figure 18 we also find a plot of the velocity correlation function

$$C_v(R) = \frac{\langle \boldsymbol{v}_i \cdot \boldsymbol{v}_j \delta(|\boldsymbol{r}_i - \boldsymbol{r}_j| - R)\rangle}{\langle \boldsymbol{v}_i \cdot \boldsymbol{v}_i\rangle}$$

where $\delta(x)$ is the Dirac δ-function. Effectively the expression above the fraction line is the average of $\boldsymbol{v}_i \cdot \boldsymbol{v}_j$ for particles i and j whose interparticle separation is R. In the plot we see that there are two peaks in C_v at $R \approx 2.2$ and $R \approx 4.4$. From Figure 16 we recognize these separations as typical nearest neighbor and next nearest neighbor distances, whose velocities are often aligned. The particles that come this close and are aligned will also be accelerated by each others induced velocity fields. Thus their velocity becomes higher than the average velocity of the system, which is reflected by the peak at $R \approx 2.2$ where $C_v > 1$.

Looking at the macroscopic details of C_v, we see that there is a global minimum at $R \approx 135$, where $C_v \approx -0.25$. This can typically be a measure of a vortex size or the width of lanes in the system. In the orientational snapshot in Figure 16 we see that there are areas of the same order with quite distinct orientation. We also observe that the circular patterns in the trajectories in Figure 17 are of the same order. We finally note when C_v takes values above 0 for R close to the system size L, this is at least partially an effect of the periodic boundary conditions.

From subsection 2.2 we remember that the energy spectrum $E(k)$ should contain the same amount of information as the velocity correlation $C_v(R)$. In Figure 18 **d** we compare the energy spectra of the system described with $N = 1500$, $N = 5000$ and $N = 15000$ particles respectively. Based on the discussion in subsection 4.6 they are computed by a discrete 2D Fourier transform of the turbulent part of the velocity field $\boldsymbol{u}(\boldsymbol{r}, t) - \langle \boldsymbol{u}\rangle$. To get the velocity field on a grid the system is split into in $\mathcal{N} \times \mathcal{N}$ boxes and the average velocity of the particles within each box is computed. To avoid too many boxes being left empty, the field is averaged over 10τ. For the systems with $N = 1500$ and $N = 5000$ particles we choose $\mathcal{N} = 200$ and $\mathcal{N} = 365 \approx 200\sqrt{5000/1500}$ respectively, so the separation between the grid points are approximately equal for the two systems. Similarly, we choose $\mathcal{N} = 632$ in the case of $N = 15000$. For the two smallest systems the energy spectra shown here are averaged over time in a steady state and of two different initial configurations. The results with $N = 15000$ are obtained from one simulation and the averaging is done over a shorter time period in this case.

The energy spectra peak at $k_L = 2\pi/L$, where the system size $L = \sqrt{\pi N/\Phi}$ depends on the number of particles. This is in line with the global oscillation we observe in the velocity correlation C_v, which indeed is the major fluctuation of C_v. Again we also recognize this in Figure 16. Both in the stream function and in the orientational snapshot we see that there are patterns corresponding to wavelengths up to the system size. Remembering that the nearest neighbor distance is $R \approx 2.2$, there is little interest in $E(k)$ for wavenumbers $k > 2\pi/2.2 = k_l$ which is marked in the plot. Above this value finite size and numerical effects will dominate the results. By comparing 1500 and 5000 we see that they are very similar at all k except for the 2-3 smallest k-values. An explanation to this is that the fluctuations on large length scales also are large in time. Thus it would be necessary to either simulate the systems over longer times or over more initial configurations to see whether the energy spectrum actually deviates from the power law form on these scales or if it is just due to lack of data. We also note that there are very few data points in this region, making deviations very visible. As the smallest k-values corresponds to wavelengths comparable to the system size L, we cannot exclude the possibility that deviations in this area are artificial effects from the periodic boundary conditions.

The energy spectrum for the system with $N = 15000$ particles deviates from the two others as it takes lower values for all $k < k_l$ and higher values above k_l. This could be caused by the

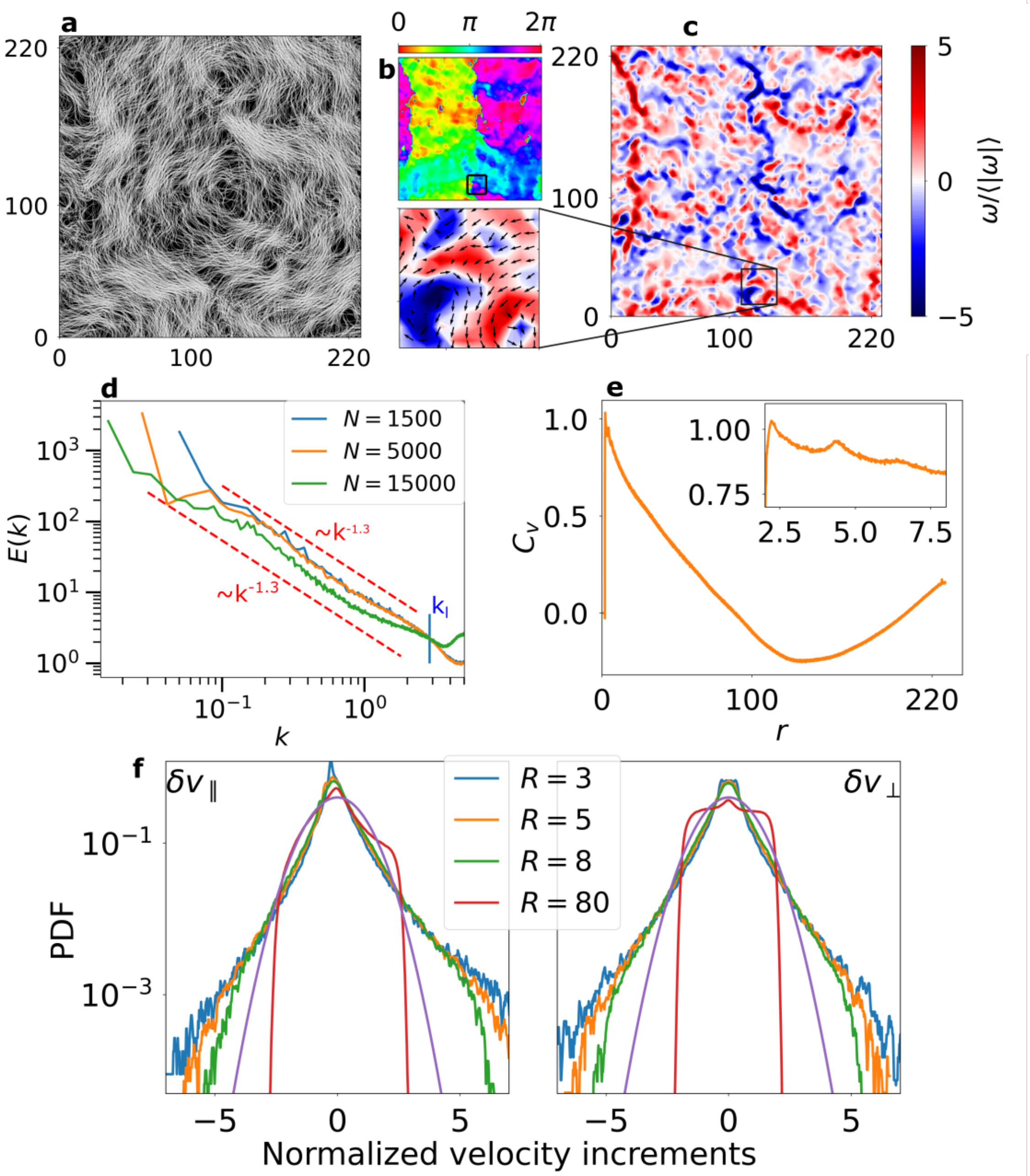

Figure 18: An example of active turbulence in a system with $N = 5000$ self-propelled particles. The flow alignment coefficients are $\gamma = 30.0$ and $\nu_2 = 2.0$ and the area fraction is $\Phi = 0.3$. **a:** A streamline plot of the system at time $t = 6000\tau$, obtained by plotting each particles position over 40 time units τ. **b:** The direction of the velocity field $\boldsymbol{u}$ at the same time and averaged over 10τ on an 80×80 grid. The colors indicate the orientation relative to the x axis. **c:** The vorticity field ω computed from the same velocity field $\boldsymbol{u}$. Blue and red areas indicate clockwise and counter-clockwise rotation respectively. The inset shows $\boldsymbol{u}$ in addition to ω for the region $[110, 140] \times [10, 40]$, which is also marked in **b**. **d:** Log-log plots of the energy spectra $E(k)$ in the cases of $N = 1500, 5000$ and 15000 particles, respectively. For comparison straight lines indicating $\sim k^{-1.3}$-scaling are shown. The maxima of all graphs are located at $k = 2\pi/L$, where L is the system size. **e:** The velocity correlation function C_v as a function of the distance r between the particles. **f:** The probability distribution function for the longitudinal and transverse velocity increments $\delta v_{\parallel,\perp}$, normalized so that the expectation value is 0 and the standard deviation is 1. The plot shows the case of four different separations R, compared with the Gaussian $\mathrm{e}^{-v^2/2}/\sqrt{2\pi}$. Both **e** and **f** are obtained from the system with $N = 5000$.

shorter averaging, but results indicate that the spectra are quite stable over a period of 2000τ. It is also possible that some numerical artifact has affected the result, since it behaves so different at large k. It should be noted that increasing the number of particles is a challenging exercise for the given system. We know that due to the long-range interactions the computation time scales as $\sim N^2$. In addition to this it is estimated that the time needed for the system to reach steady state scales linearly with the system area $L^2 \sim N$. Thus, the computation time needed increases with the number of particles as at least $\sim N^3$.

The most interesting property of the energy spectrum is the scaling in the region $k \in [0.08, 2.8]$ corresponding to wavelengths $\sim [2.2, 78.5]$ for the two smallest systems. For $N = 15000$ a similar scaling occurs at larger k. The straight lines in the plot indicate scaling $\sim k^{-\beta}$ with $\beta = 1.3$. Thus the energy spectrum takes a clear power law shape over more than one decade on both the x- and y-axis. By linear regression of $\log(E)$ as a function of $\log(k)$ in the region $[0.08, 2.8]$ for $N = 5000$, we confirm that the best fitting exponent is $\beta = 1.3 \approx 4/3$ compared to Kolmogorovs $5/3$-law in Eq. (1). The length scales at which we observe this behaviour are most visible in the vorticity and streamline plots in Figure 18. We see how the streamlines are curved on wide range of scales, which shows in the vorticity field by areas of different sizes with high vorticity. Further investigations show that the scaling of the system with $N = 15000$ is very similar to the two others in the region $k \in [0.08, 1.0]$ and that it exhibits the same scaling for even smaller k.

Comparing with the energy spectrum obtained from simulations of an active nematic fluid by Alert et. al. in Ref. [44] and Figure 4 we see that the form is quite similar to our the spectra we observe. There is a difference in the exponent of the power law, with our system showing a more rapid decay of kinetic energy as the length scales decrease. However, in both cases the spectra seem to follow the power law behaviour up to the length scales of the respective systems, even though there are some small-k deviations in our case. This indicates that the observed scaling properties are universal, in the sense that one can coarse-grain and simulate bigger systems and observe the same behaviour. In the active nematic fluid there is a distinct peak in the energy spectra which is attributed to a characteristic wavelength at which there is maximal energy injection. The spectrum produced by our model does not display any such definite peak, but we do see that there is a small protuberance near the wavenumbers corresponding to the nearest neighbor distance. This would at least be a natural wavelength for maximal energy injection. Finally, we observe that the k^{-1} scaling regime extends over a little more than one decade on both the horizontal and vertical axis in Figure 4. Alert et. al. assert that this conclusively confirms this scaling regime [44], and the regime where we observe $E(k) \sim k^{-1.3}$ is not inferior to this. The energy spectrum observed by Radjai and Roux [35] in Figure 5 also show scaling over similar regime sizes.

The final plot in Figure 18 shows the probability distribution functions for the longitudinal and transverse components of the velocity increment $\delta\boldsymbol{v}$ for different separation distances R. The distributions are normalized so that the expectation value is 0 and the standard deviation is 1 and compared to the Gaussian distribution $\mathrm{e}^{-v^2/2}/\sqrt{2\pi}$ (purple curve). The data for the distributions are collected every 25th time unit τ over a time period of 1500τ. The velocity increment $\delta\boldsymbol{v}(t, \boldsymbol{r}, \boldsymbol{R}) = \boldsymbol{v}(t, \boldsymbol{r}+\boldsymbol{R}) - \boldsymbol{v}(t, \boldsymbol{r})$ is defined by the positions of the particles. Following Ref. [41], we divide its statistics into a longitudinal and a transverse projection $\delta v_\parallel = \hat{\boldsymbol{R}} \cdot \delta\boldsymbol{v}$ and $\delta v_\perp = \hat{\boldsymbol{T}} \cdot \delta\boldsymbol{v}$, respectively. $\hat{\boldsymbol{R}} = \boldsymbol{R}/|\boldsymbol{R}|$ is the unit vector along the separation axis, while $(\hat{\boldsymbol{T}})_i = \epsilon_{ij}\hat{R}_j$ is a unit vector perpendicular to $\hat{\boldsymbol{R}}$. For $R = 3, 5, 8$ we observe a distinct non-Gaussian broadening of the probability distribution functions for both the longitudinal and transverse components. These exponential tails grow as R decreases, and for $R = 80$ there is no such broadening.

From the velocity increments $\delta v_{\parallel,\perp}$ we may define the velocity structure functions $S^n_{\parallel,\perp}(R) \equiv \langle(\delta v_{\parallel,\perp})^n\rangle$ for $n = 1, 2, \ldots$. $\langle\cdot\rangle$ denotes a spatiotemporal average over $\boldsymbol{r}$ and t, but for isotropic turbulence in a steady state the directional dependence vanishes and thus $S^n_{\parallel,\perp}$ is simply a function of the separation distance $R = |\boldsymbol{R}|$. These structure functions are common features in studies of turbulence in high-Re fluids [29, 91], as for example Kolmogorovs 4/5 law in Eq. (2).

In Figure 19 we see loglog plots of the normalized structure functions $S^{2,3,4}_{\parallel,\perp}$ as functions of the separation distance R. We remember from Eq. (4) that if $E(k) \sim k^{-\beta}$ theory of inertial turbulence predicts that $S^2(R) \sim R^{\beta-1}$. We observed a power law form of $E(k)$ with $\beta \approx 1.3$ in the range of k corresponding to wavelengths $\sim [2.2, 78.5]$. Thus it is natural to check if $S^2_{\parallel,\perp}(R) \sim R^{0.3}$ in this range. This is clearly not the case. By comparison with the red, dashed lines we see that $S^2_{\parallel,\perp}$ scale as R^{p_2} with an exponent p_2 in the region $p_2 \in (0.75, 1.0)$. Similarly we find that $S^4_{\parallel,\perp}$ scale with an exponent $p_4 \in (1.2, 1.45)$. For $S^3_\perp$ we see that the data do not show any characteristic behaviour, but we see no obvious explanation to this. However, $S^3_\parallel$ seems to scale with an exponent $p_3 \in [0.65, 0.8]$, i.e. $p_3 < p_2$.

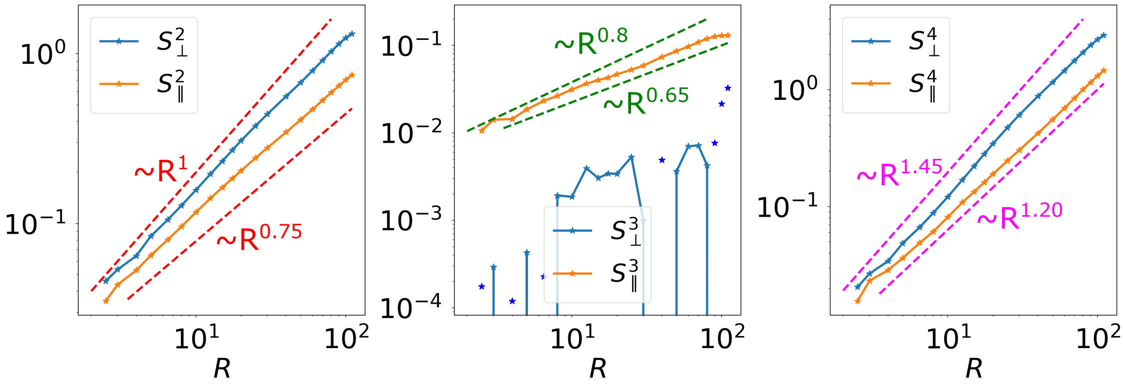

Figure 19: Log-log plots of the structure functions $S^{2,3,4}_{\parallel,\perp}$ as a function of separation distance R for the system with $N = 5000$ particles, flow alignment coefficients $\nu_2 = 2.0, \gamma = 30.0$ and area fraction $\Phi = 0.3$. The structure functions are normalized by $\langle \boldsymbol{v}^2 \rangle^{n/2}$ for $n = 2, 3$ and 4 respectively. For comparison the straight dotted lines show functions on the form $\sim R^\alpha$, where the exponents are indicated in the plots. The blue stars without connected lines in the center plot indicate absolute values of $S^3_\perp$ when it takes negative values.

Comparing our observations on the structure functions with theory on inertial turbulence we indeed find that $S^n_{\parallel,\perp}(R) \sim R^{p_n}$ in general, with an exception in $S^3_\perp$. However, in our case p_n is not linear in n even at low orders, which is the case in inertial systems, ref Eq. (3). Kolmogorovs 5/4-law does not apply and we have $p_2 \neq \beta - 1$. Nevertheless, we do not expect these specifics to be equivalent to turbulent high-Re flows, given the fundamental differences between the systems. The main point is that the statistical parameters of the systems display comparable behaviours.

In Ref. [41] distinct maxima of $S^2_\perp$ and $S^4_\perp$ at distances smaller than the system size are observed. These results are obtained from experimental observations of high-density bacterial suspensions in quasi-2D and 3D, simulations of a continuum model assuming incompressibility and simulations of an SPR-model. Vorticity maps and power spectra from this study are shown in Figure 3. The SPR-model is a model for dry active matter systems, in contrast to ours which models wet systems [92]. The peaks they observe in these structure functions are attributed to a characteristic vortex size in the system. Comparing both velocity correlation functions and energy spectra with our observations, it is clear that the corresponding vortex size in our case is at the scale of the system size. Therefore it is also natural that we observe strictly increasing structure functions $S^{2,4}_{\parallel,\perp}$.

Following the study of turbulence in granular media in Ref. [35], we introduce a measure of the 'flatness' $F_{\parallel,\perp}(R) = S^{*4}_{\parallel,\perp}/S^{*2}_{\parallel,\perp} - 3$ of the probability distribution functions. To measure the flatness of the distributions that are plotted in Figure 18, we compute the structure functions $S^{*2,4}_{\parallel,\perp}$ from renormalized distributions where the standard deviation is 1 and the expectation value is 0. If not we would see very sharp distributions for small R that broadens as R increases. This would not be any new information as we can easily see from e.g. Figure 16 that particles close to each other have similar velocities. We are interested in the fluctuations in the velocity differences relative to the scale. The flatness F is zero for a Gaussian distribution and 3 for a purely exponential distribution. Note that by 'flatness' in this sense might as well be interpreted as the width of the distributions. A simple example to illustrate this is that a uniform distribution with width $2b$ will have a flatness $F = 3b^2/5 - 3$.

In Figure 20 we see the flatness of the distributions as functions of the separation distance R. Here we show a comparison with another system where the area fraction is $\Phi = 0.1$ and the flow alignment coefficients are $\nu_2 = 1.0$ and $\gamma = 30.0$, which is further presented in Figure 23. For now, we will however focus on the system we have studied so far where $\Phi = 0.3$, $\nu_2 = 2.0$ and $\gamma = 30.0$. Coherent with the observations from Figure 18, we see that F is large at small separation distances

R, but decays quite rapidly as R increases. This is very similar to the observations in Ref. [35]. Both curves $F_{\|,\perp}$ rise above 3, meaning that the distributions are 'flatter' or broader than a purely exponential distribution for small R. For large R the curves go below zero, i.e. these distributions are sharper than a Gaussian. An interpretation of this is that at scales comparable to the system size $L \approx 229$ the velocities of the particles are more coherent than in a comparable ideal gas system, whose distribution is Gaussian [93]. This is no surprise when we look at the snapshot of the system in Figure 16, which clearly demonstrates the large scale coherence in the velocity directions. In addition to this the self-propulsion of the particles make collisions and external forces relatively less important to the absolute velocity, compared to an ideal gas.

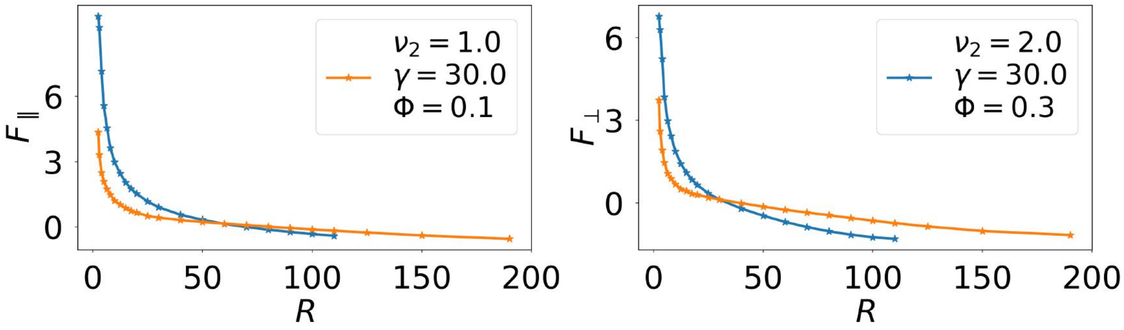

Figure 20: The flatness $F_{\|,\perp}$ of the probability distribution functions for the velocity increments $\delta v_{\|,\perp}$ as a function of the separation distance R. Two systems with different flow alignment coefficients γ, ν_2 and area fraction Φ, further described in Figure 18 and 23 respectively, are compared. A Gaussian distribution has flatness $F = 0$, while for a purely exponential distribution $F = 3$.

As mentioned earlier, an increasing broadening of exponential "tails" at progressively smaller scales is a hallmark of fully developed turbulence [29, 35]. An interpretation of this broadening is that at small scales there are fluctuations in the velocities that vanish when you average over larger scales. In studies of inertial turbulence, this behaviour is attributed to a phenomenon called intermittency, which is basically a highly irregular dissipation of energy at small scales [28].

In Figure 21 the root mean square (RMS) displacements $\lambda_i = \sqrt{(\boldsymbol{r}_i(t) - \boldsymbol{r}_{0,i} - \langle \boldsymbol{v} \rangle t)^2}$ from a starting point $\boldsymbol{r}_{0,i}$ of the three trajectories in Figure 17 are plotted. At the starting point $t = 0$ the system is already in steady state. We also see a plot of the time derivatives

$$\frac{\partial \lambda_i}{\partial t} = \operatorname{sgn}\left[(r_{i,x} - r_{0,i,x} - \langle v_x \rangle t)\right](v_{i,x} - \langle v_x \rangle) + \operatorname{sgn}\left[(r_{i,y} - r_{0,i,y} - \langle v_y \rangle t)\right](v_{i,y} - \langle v_y \rangle)$$

which effectively sums the particles deviation from the average velocity in x and y direction. $\operatorname{sgn}(x)$ is the sign of x. We see that even though the RMS displacements seem to evolve quite smoothly over global times ($t \sim L$), there are constant fluctuations in velocity on short timescales. This is typical behaviour for systems where Lévy walks occur. These short-scale fluctuations are also evident in Figure 22 where see three probability distributions for $\sqrt{\boldsymbol{v}^2}$ averaged over the same time interval. As the time Δt over which we evaluate each particles velocity decreases, we observe more noise on the distribution, even though it is averaged over 3000τ. This illustrates why there is a broadening of the probability distribution functions at small scales in Figure 18 and why it vanishes at larger scales.

To investigate the large-scale evolution of the RMS displacements further we have plotted the average displacement $\langle \lambda \rangle$ of all particles as a function of time in Figure 22. The log-log plot shows that there are two distinct time-domains with different behaviours. For $t \lesssim 10^2$ we see superdiffusive behaviour where $\langle \lambda \rangle$ is almost linear in t, while for larger t the behaviour seems to be less diffusive with $\langle \lambda \rangle \sim t^{\vartheta}$ where $\vartheta \approx 0.5$. This is confirmed by doing linear regression on $\log(\langle \lambda \rangle)$ as a function of $\log(t)$. For $t \in [0, 70]$ we find that $\vartheta = 0.94$, while for $t \in [550, 3000]$ the corresponding result is $\vartheta = 0.53$. Such a cross-over from a ballistic regime to a diffusive regime is consistent with other results in active turbulence [49, 94], and has been observed experimentally for swimming bacteria in a quasi-2D system [95]. The particles can thus move more or less straight for about 70τ on average before we observe any large scale alternations to travelling direction. With a small-scale RMS velocity $v_{\mathrm{RMS}} = 1.19$ this means a local path length of about $80 r_0$. We recognize

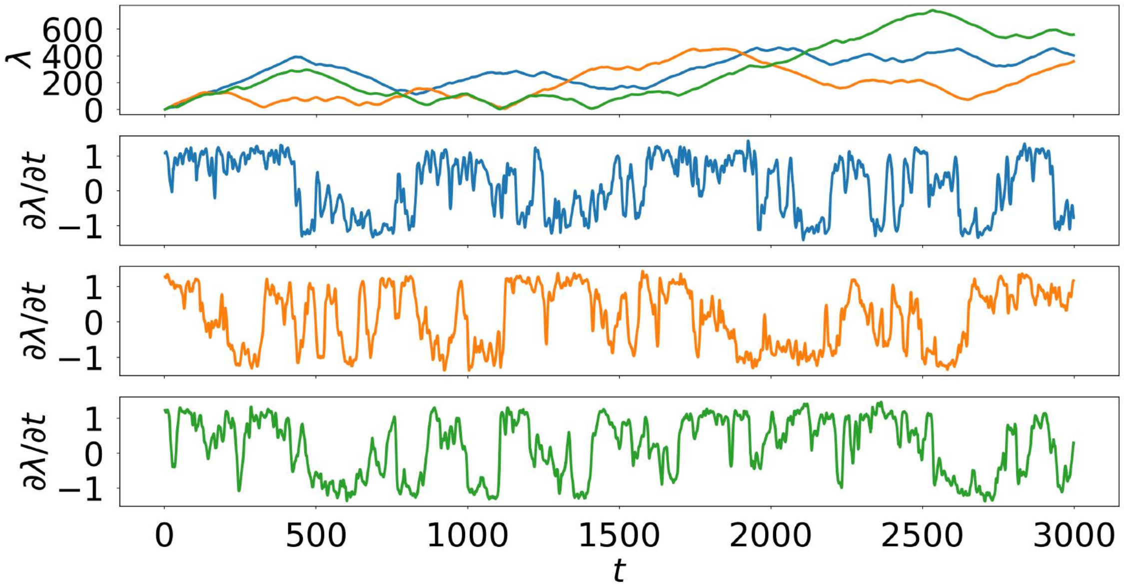

Figure 21: *Top:* The root mean square displacements $\lambda_i = \sqrt{(\boldsymbol{r}_i(t) - \boldsymbol{r}_{0,i} - \langle \boldsymbol{v} \rangle t)^2}$ from a starting point $\boldsymbol{r}_{0,i}$ of the three trajectories plotted in Figure 17 as a function of time t. *Bottom:* The time derivatives of the root mean square displacements, effectively showing the deviation of the particle velocity $\boldsymbol{v}_i$ from the average velocity $\langle \boldsymbol{v} \rangle$, summed over x and y components. Interpolating the derivatives over 1, 2, 4 and 8 timesteps δt all produce equivalent results. The colors of the graphs are consistent with Figure 17.

these scales as the inverse of the wavenumbers k at which we observe a power law form of the energy spectrum $E(k)$. We are aware that the self-propulsion of the particles make super-diffusive behaviour more obtainable, but this is still no assurance for such rapid scaling [96].

We can now try to connect the picture given by the obtained results. On the scale from a few particle sizes up to $\sim 50 - 80 r_0$ we have seen (i) a power law behaviour of the energy spectrum $E(k)$, (ii) a non-Gaussian broadening of probability distribution functions of the velocity increments $\delta \boldsymbol{v}$ and (iii) close to linear scaling $\langle \lambda \rangle$ with respect to t. From (iii) we deduce that at lengths in this range the particles may move quite independently of the global dynamics, and with fluctuations that become more and more independent of the global dynamics the smaller they are. The occurrence of these fluctuations is confirmed by (ii). We know that by self-propulsion, each particle injects energy into the system. When the particles exhibit the smallest scale fluctuations, close to the particle size r_0, the part of the injected energy responsible for these fluctuations leads to no further larger scale movement. Thus there is no further accumulation of kinetic energy at this scale, reflected by $E(k)$ going to zero for large k. However, as the scale of these fluctuations increases, more and more particles have coherent fluctuations. We see this by the decrease of the flatness F with increasing R. Thus movements on larger scales appear and the injected kinetic energy of responsible for these fluctuations from different particles add up more constructively. This is consistent with (i) as k is the inverse of the length. As the length scale increases more and more particles have coherent fluctuations and the kinetic energy increases with the scales. This goes on up to lengths at which the aligning mechanisms no longer yield non-zero correlations. In our cases these lengths seem to be limited by the system size.

The three statements (i-iii) above are equivalent to the three main arguments Radjai and Roux base their conclusion on in the discovery of turbulence in granular media [35]. Based on these three observations, the comparison with the results of Alert et. al. [44] and the further investigation we have done above, we claim that the descried system exhibits active turbulence. To the authors knowledge, this has not been reported in polar particle models with hydrodynamic interactions before. The two active systems we have compared with, the dry active system by Wensink et. al. in Figure 3 and the one by Alert et. al. in Figure 4, are both nematic systems. Carenza et. al. [97] observe scaling regimes in a polar system from simulations of incompressible continuum equations describing emulsion dynamics. Looking at Figure 16 and 18a we see that an assumption of

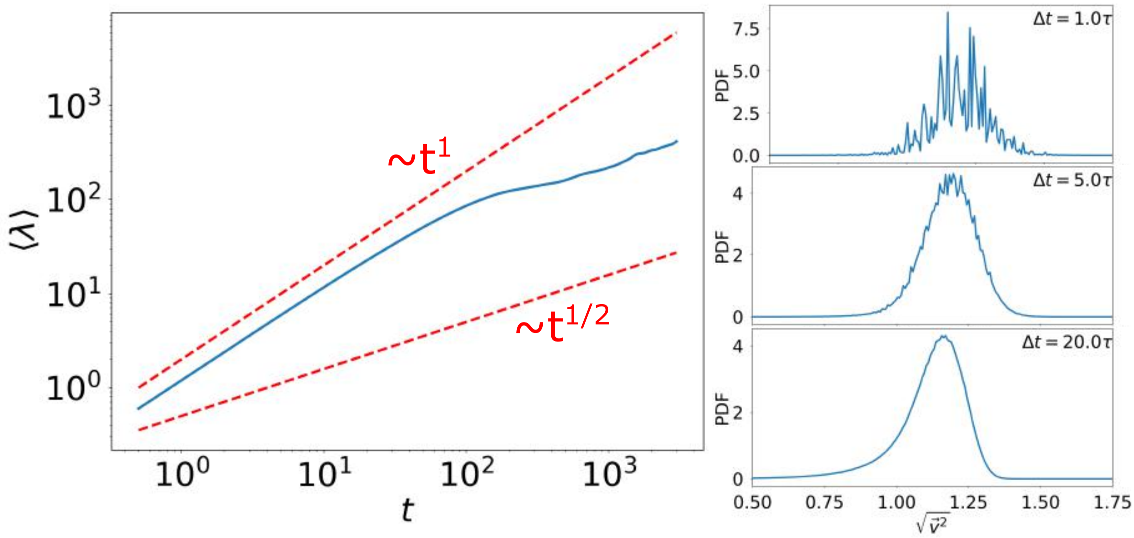

Figure 22: *Left:* Log-log plot of the average root mean square displacement λ for all $N = 5000$ particles as a function of time t. The flow alignment coefficients of the system are $\nu_2 = 2.0$ and $\gamma = 30.0$ and the area fraction is $\Phi = 0.3$. *Right:* Probability density functions of the absolute value of the velocity $\sqrt{\boldsymbol{v}^2}$ from the same system. The velocities are computed by $(\boldsymbol{r}_i(t+n\tau) - \boldsymbol{r}_i(t))/n\tau$ with $n = 1, 5$ and 20 respectively. The computed RMS velocities in the three cases are $v_{\text{RMS}} = 1.19$, $v_{\text{RMS}} = 1.18$ and $v_{\text{RMS}} = 1.12$. The distributions and RMS-velocities are computed over the same time 3000 as the RMS displacement to the left.

incompressibility would be cruel to describe our system. A comparable particle model is presented by Großmann et. al. in Ref. [85]. Their model contains no hydrodynamic interactions, but a short-range alignment interaction similar to ours and an anti-alignment interaction over larger scales. The latter is however not long-range like our hydrodynamic interactions in the sense that it has a finite cutoff, thus this is also a dry active matter model. They have also included an angular noise term. The energy spectrum is similar to the what we see in Figure 3 with a distinct peak.

In a very recent preprint of a review [45], Alert et. al. summarize the status of active turbulence. In the section concerning polar, wet active systems it is clear that the main focus in this field has been on macroscopic models with continuum theories. We find no examples of microscopical particle models. To the authors knowledge, the results obtained from our simulations represent novel findings within studies of polar, wet active matter.

During the introduction of the model in earlier sections we have taken inspiration of Tsang and Kanso [69] and Lefauve and Saintillan [71] and it is therefore natural to compare with their results. However, neither of those have incorporated the alignment term from the flying XY-model. Tsang and Kanso observe a state with turbulent-like behaviour at high ν_2, but as they simulated systems with only $N = 100$ particles this is can only be regarded as an initial detection of interesting behaviour. Lefauve and Saintillan on the other hand simulate $N = 5000$ particles. Their model consists of the ν_2 term as well as rotational diffusion by statistical noise. They observe a state consisting of two large-scale vortices, which is reminiscent of what we have observed in our system. However, no further investigation on whether the system is turbulent or not was performed.

5.2 Comparison with another system, $\nu_2 = 1.0$, $\gamma = 30.0$, $\Phi = 0.1$

Having seen that a system with flow alignments coefficients $\nu_2 = 2.0, \gamma = 30.0$ and area fraction $\Phi = 0.3$ exhibits active turbulence, we will now compare it to a system where $\nu_2 = 1.0$, $\gamma = 30.0$ and $\Phi = 0.1$. These parameters are chosen because we want to investigate lower densities. However, at lower densities we expect the γ-term to become less dominant, so we also reduce ν_2 from 2 to 1. The area fraction is reduced by increasing the system size L so that we are still looking at $N = 5000$ particles. In Figure 23 we see plots equivalent to Figure 18 for the new system. Comparing the two streamline plots it is clear that we observe less global scale patterns in the new system. As the interparticle distances increase we expect the short-range alignment interaction to become less dominant. Thus the large-scale flocks we observe in Figure 18 seems to be a result of the particles being packed close enough to make the alignment interaction dominant over scales larger than its own range. This can be viewed as inducing a form of elasticity to the system. The alignment interaction creates large-scale coherent flocks while the hydrodynamic dipole interaction curves them. When the area fraction is reduced to 0.1 we see that this effect largely disappears and the streamlines appear more chaotic on the global scale.

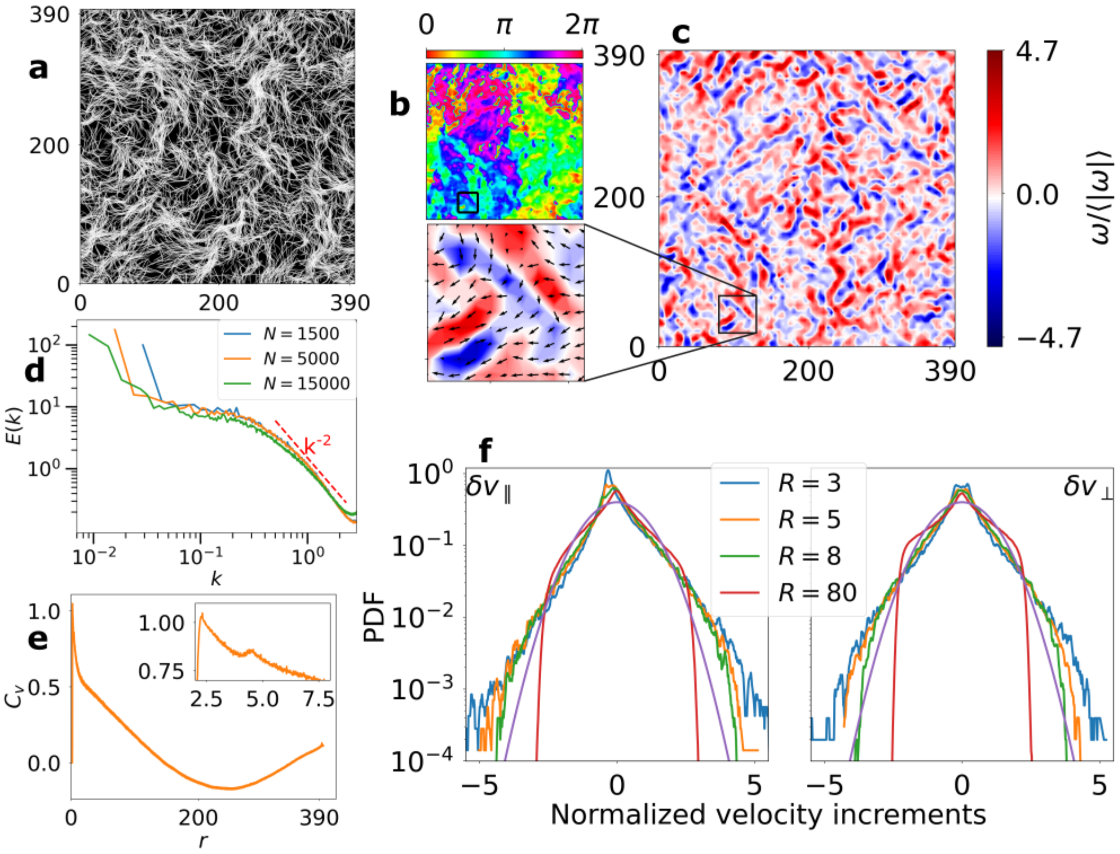

Figure 23: Turbulent characteristics of a system with $N = 5000$ self-propelled particles, flow alignment coefficients $\nu_2 = 1.0, \gamma = 30.$ and area fraction $\Phi = 0.1$. **a** shows a streamline plot of the system, **b** the direction of the velocity field $\boldsymbol{u}$ and **c** the vorticity field ω computed from $\boldsymbol{u}$ with the region $[80, 130] \times [18, 68]$ magnified. In **d** the power spectrum is plotted and compared to the cases of $N = 1500$ and 15000 particles, and the dotted line indicates a scaling k^{-2}. **e** shows the velocity correlation function C_v and **f** the normalized probability distribution functions for the velocity increments $\delta v_{\perp,\parallel}$ at different separation distances R.

In subsection 4.5 we introduced a measure $H_{\text{el}} = \sum_i H_{\text{el},i}$ of the total elasticity of the system, based on the first term of the effective angular potential in Eq. (31). The elastic potential

$$H_{\text{el},i} = -\gamma \sum_{j \neq i}^{N} \frac{\boldsymbol{p}_i \cdot \boldsymbol{p}_j}{|\boldsymbol{r}_i - \boldsymbol{r}_j|^5}$$

indicates how aligned the particle i is with its neighbors, weighted by the inverse interparticle distances. If $H_{\text{el},i} > 0$ the particle i is orientated opposed to its nearest neighbors, while a negative value indicates that it is aligned with them. The more aligned neighbors the particle has, the more negative will $H_{\text{el},i}$ be. As an example, with $\gamma = 30.0$ a completely aligned particle at a distance $2.2r_0$ from particle i will contribute about -0.58 to $H_{\text{el},i}$.

In Figure 24 we have plotted all particles with colors indicating their elastic potential for the high- and low density systems. These snapshots clearly illustrate the presence of coherent flocks up to relative large scales in the high-density systems that are more or less absent the low-density case.

Knowing that we have a higher flow alignment coefficient ν_2 in the former system which should contribute to breaking up order, the formation of these flocks is indeed a result of the alignment interaction being more dominant at higher densities. We do take into account that the different scales of the two plots can give a slightly misleading comparison of the systems, but a check of this yielded no alternation of the impression of the two. If we compare this snapshot with the stream function in Figure 16 it appears that the density of the flocks is lower near the extrema of the stream function. Together with the directional snapshot in Figure 16 this gives a macroscopic picture of a system where coherent flocks of different sizes travel around two large-scale, counter-rotating vortices.

We also note that in the high-density system particles within the flocks take values of $H_{\text{el},i} \lesssim -3$. Knowing that an aligned particle at nearest neighbor distance contributes with about -0.58, this supports the impression from Figure 16 that particles within the flocks form hexagonal structures.

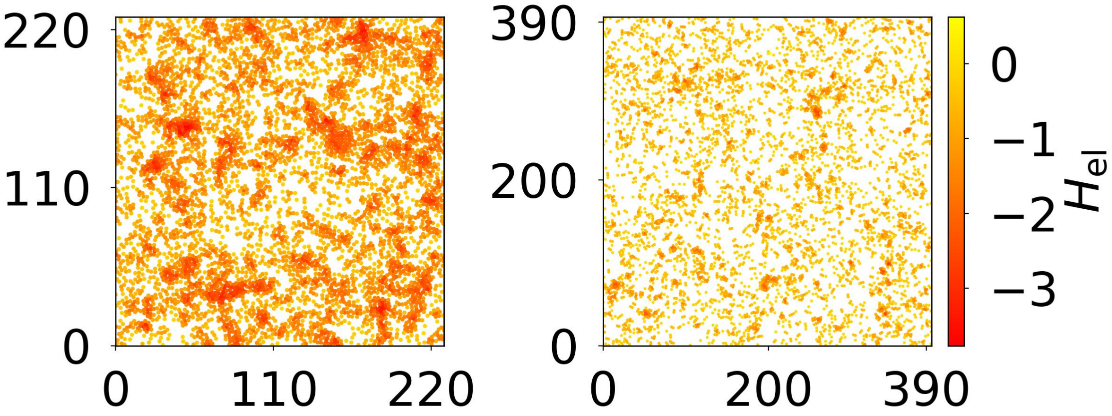

Figure 24: Snapshots showing the elastic potential $H_{\text{el},i}$ of all particles. To the left we see the system with flow alignment coefficients $\nu_2 = 2.0$ and $\gamma = 30.0$ and area fraction $\Phi = 0.3$. On the right side the corresponding parameters are $\nu_2 = 1.0$, $\gamma = 30.0$ and $\Phi = 0.1$. The sizes of the particles are proportional to the system sizes. The left plot shows large areas with low potential indicating coherent flocks of particles. This is almost absent to the right.

To get an impression of how the average particle observes its surroundings, we have plotted the pair polarization $\boldsymbol{P}(\boldsymbol{R})$ for the two systems in Figure 25. The pair polarization for a particle i is defined as

$$\boldsymbol{P}_i(\boldsymbol{R}) = \langle \boldsymbol{p}_j(\alpha_j - (\alpha_i - \pi/2))\delta(\boldsymbol{R} - \boldsymbol{A}_{\text{rot}} \cdot \boldsymbol{R}_{i,j})\rangle_j, \tag{53}$$

where $\boldsymbol{R}_{i,j}$ is the separation vector between the particles i and j and $\boldsymbol{A}_{\text{rot}}$ is a rotation matrix that rotates $\boldsymbol{R}_{i,j}$ an angle $\pi - \alpha_i$ counterclockwise. The brackets $\langle ... \rangle_j$ indicates the average over all particles $j \neq i$. $\boldsymbol{P}_i(\boldsymbol{R})$ then denotes the orientation of a particle positioned at $\boldsymbol{R}$ in a reference system where particle i is positioned in origin and oriented along the y-axis. $\boldsymbol{P}$ is the average $\boldsymbol{P}(\boldsymbol{R}) = \langle \boldsymbol{P}_i \rangle_i$ over all particles in the system.

We see that in both systems the pair polarization has the symmetry of a dipolar flow, as plotted in Figure 9. This is clearly a result of the dipole alignment interaction, and the fact that we see this symmetry even on global scale reflects its long range. The effect of the alignment interaction is apparent by the fact that there is a strong polarization pointing upwards even when moving along the horizontal axis from the center. This effect is clearer in the left plot and substantiates that the alignment interaction becomes more dominant at higher density. In addition to the higher density it is of course also a factor that the flow alignment coefficient ν_2 is higher in the high-density case, which we expect to make the dipole symmetry more pronounced.

As we see by the symmetry, the the dipole alignment interaction does not only break order. By looking at the plot of the dipolar velocity flow in Figure 9, we see that for a particle positioned straight ahead or behind another particle an orientation along this field contributes to order between the two. Thus, along the elongation axis of the particles orientational order is favored on all scales. It is also evident that even though the interaction appears to create chaos in the dynamics of the system, Figure 25 shows that there are predictable patterns in these dynamics. This is an important

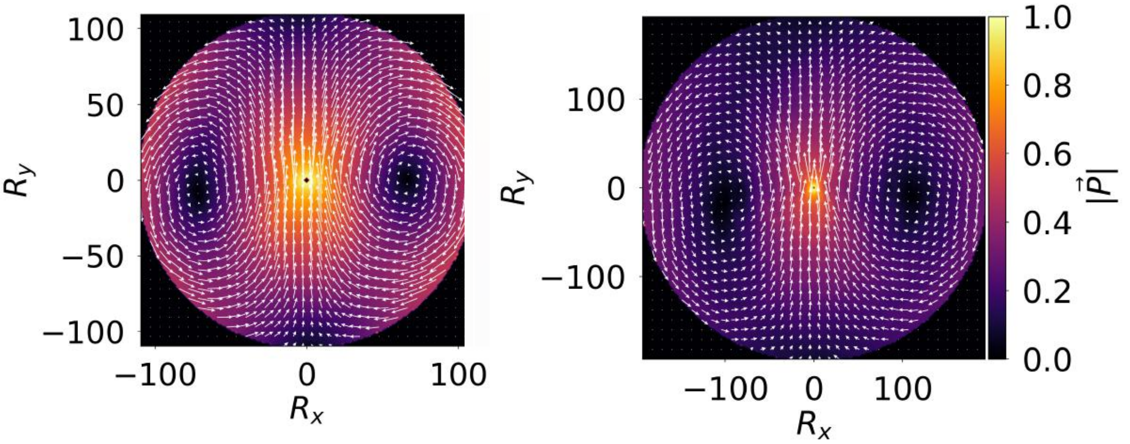

Figure 25: These plots show the pair polarizations $\boldsymbol{P}(\boldsymbol{R})$ for the two systems with parameters $\nu_2 = 2.0, \gamma = 30.0, \Phi = 0.3$ (left) and $\nu_2 = 1.0, \gamma = 30.0, \Phi = 0.1$ (right) respectively. $\boldsymbol{P}(\boldsymbol{R})$ shows the average polarization in the surroundings of a particle, shifted so that the given particle is centred in origin and pointing in positive y-direction. The colors indicate the strength $|\boldsymbol{P}|$ of the polarization, while the arrows indicate both strength and direction. The plots show the polarization up to a distance $|\boldsymbol{R}| = L/2$, where L is the size of the respective systems. Both systems exhibit a distinct dipolar symmetry in $\boldsymbol{P}$, which is most pronounced in the high-density case to the left.

distinction from models where noise is the order-breaking mechanism. From the comparison it can also be argued that the increased local order caused by the alignment interaction leads to a more effective dipole interaction on long scales. This is sensible because the dipolar fields induced by the individuals within a coherent flock will be very similar and thus add up effectively on large scales. As the a higher density leads to more order on short lengths it is expected that this leads to relatively less small-scale fluctuations compared to other scales. With the local order leading to a more effective dipole alignment interaction on large scales this could produce relatively more long-range fluctuations. A comparison of the energy spectra in Figure 18 and 23 it is evident that fluctuations on large scales are relatively more dominant at $\Phi = 0.3$ than at $\Phi = 0.1$.

A comparison of the velocity correlation functions in Figure 18 where $\Phi = 0.3$ and 23 where $\Phi = 0.1$ supports the impression of increased flocking at higher densities. In the low-density system we see that $C_v(R)$ decays rapidly at small distances, and the relative correlations between next-nearest neighbors are indeed smaller than what we see at high densities. We do however note that the peaks in C_v indicating typical distances to the nearest and next-nearest neighbors are quite similar, with $2.2r_0$ and $4.4r_0$ at $\Phi = 0.3$ and $2.3r_0$ and $4.5r_0$ at $\Phi = 0.1$ respectively. This suggests that up to a certain area fraction the nearest neighbor distances is a microscopical detail determined by the dipolar field, the steric interactions and perhaps also the mobility coefficient μ. We see that the macroscopic shapes of the velocity correlations are similar, with minima at about $0.6L$ in both systems. As we discussed earlier this global shape is likely to be an artifact of the periodic boundary conditions in combination with the dipole alignment interaction. However, as we discussed the anti-correlation on large distances is also an implicit consequence of the short-scale alignment because it leads to more aligned dipolar flows. Thus it makes sense that we observe a stronger anti-alignment in the high-density system, where $\min(C_v) \approx -0.25$, than in the low-density counterpart where $\min(C_v) \approx -0.17$.

As observed earlier the less pronounced global patterns in the streamline plot in Figure 23 also manifest in the energy spectrum. First we note that $E(k)$ takes lower values for all k in the low-density system compared to the high-density system in Figure 18. From the definition in Eq. (14) we remember that $E(k) \sim 1/L^2$, meaning that as the system becomes smaller the kinetic energy is distributed over a shorter range of wavelengths. But even when we account for this by looking at $L^2E(k)$ we observe higher values overall in the high-density system. A consequence of the flocking is that the velocities of the particles increase, as each particle is accelerated by the velocity fields induced by the neighboring particles. The RMS velocities of the high- and low-density systems are $\sqrt{\boldsymbol{v}^2} \approx 1.19$ and $\sqrt{\boldsymbol{v}^2} \approx 1.10$ respectively. Thus, it is sensible that we observe higher kinetic energies in general for the high-density system.

More interesting than the exact values are the shapes of the energy spectra in the two systems. In Figure 18 we saw a clear power law form over at least one decade when the area fraction is $\Phi = 0.3$. The energy spectrum in the lower density system in Figure 23 is qualitatively different. For k corresponding to wavelengths comparable to the nearest neighbor distance and up to about $15r_0$ the spectrum is compared to a straight line indicating $\sim k^{-2}$. For the range as a whole this comparison is not too far off, but there is indeed a curvature on $E(k)$ in this area. It is however interesting that below $k \approx 0.2 \approx 2\pi/30$ the spectrum is almost flat for all system sizes $N = 1500$, $N = 5000$ and $N = 15000$, except for the peak corresponding to the system size. This is in line with the lack of global patterns in the streamline plot. Looking at the vorticity plot in Figure 23 it is arguable that this scale is comparable to the most standout size of unicolored areas. This vorticity field appears to display at least as much distinct areas and sharp contrasts as what we saw in the other system, asserting that the activity on short scales is at least as high in this system. We also recognize the behaviour of the system with $N = 15000$ from what we saw in Figure 18, namely that it takes higher values than the two other at high k and lower values otherwise.

In Figure 20 we showed a comparison of the flatness of the probability distribution functions for the velocity increments $\delta v_{\perp,\parallel}$ of the two systems. This clearly shows the exponential tails of the distributions at small scales are more distinct in the high-density system and that they are more persistent as R increases. However, we observe that there is a non-Gaussian broadening at small scales in the the low-density system as well, visualized in Figure 18. This is in line with the findings we have made so far, indicating that on small scales the system exhibits turbulent-like behaviour, but this behaviour does not seem to persist on larger scales.

The comparison of these two systems have shown that the relatively high density is a key factor for the universal scaling of the active turbulence we observe in Figure 18. With $\Phi = 0.3$ the particles appear to be connected in a large-scale, coherent motion to a larger degree than the case of $\Phi = 0.1$. This is illustrated by the streamline plots and energy spectra in Figure 18 and 23, and by the pair polarizations in Figure 25. At the higher density the angular alignment interaction becomes more dominant and produces particle alignments on larger scales. This seems to induce an effective elasticity in the system that facilitates large-scale fluctuations. At low density on the other hand, there is less short-range correlation and the particle motions seem less connected. This in turn make each particle move more freely but large scale fluctuations less feasible.

5.3 Relation between energy spectrum and system parameters

Having seen how the decrease in density changed the behaviour of the system, we now want to investigate how the different parameters affect the energy spectra. In Figure 26 we have plotted various energy spectra to see the effects of the flow alignment coefficients γ, ν_2 and the area fraction Φ. The overall picture is that the shapes of the energy spectra are mainly decided by the area fraction Φ.

In the upper left plot of Figure 26 we take the system that we have seen to exhibit active turbulence as a starting point by setting $\gamma = 30.0$, $\Phi = 0.3$ and vary ν_2 from 0.2 to 3.0. It is clear that within this range the variation of ν_2 does not lead to any significant change in the power spectra. What we observe is that increasing ν_2 leads more fluctuations on short scales and hence less fluctuations on the largest scales. As ν_2 is the strength of the dipolar alignment interaction that breaks order in the system, this is not unexpected. The decreased order is an obstacle for the energy cascade from particle scale up to the global scale as large-scale coherent fluctuations become less frequent. Thus, the exponent β in the power-law $k^{-\beta}$ decreases somewhat as ν_2 increases.

For the smallest values of ν_2 we also see that a peak becomes visible for $k \in [1.5, 2.5]$. This peak is not a local maxima but rather a protuberance from the otherwise flat spectrum. With smaller ν_2 we expect more local ordering, and as we have seen coherent flocks appear. Thus, up to a characteristic flock size these particles fluctuate relatively more as group than as individuals within the group. Thus, there is relatively more energy transfer up to the scale of the flock size than in what would be the case without flocking, producing a steeper energy spectrum in this area. Above this flocking scale however, the fluctuations will be less affected and the spectrum flattens out. To further illustrate this we have plotted the derivatives of the velocity correlation functions for the same systems in Figure 27. We see that at small separation distances R, $\mathrm{d}C_v/\mathrm{d}R$ take the least negative values for small ν_2, meaning that correlations are more persistent in these systems. However, as R increases we see that these velocity correlations will decrease faster than the systems

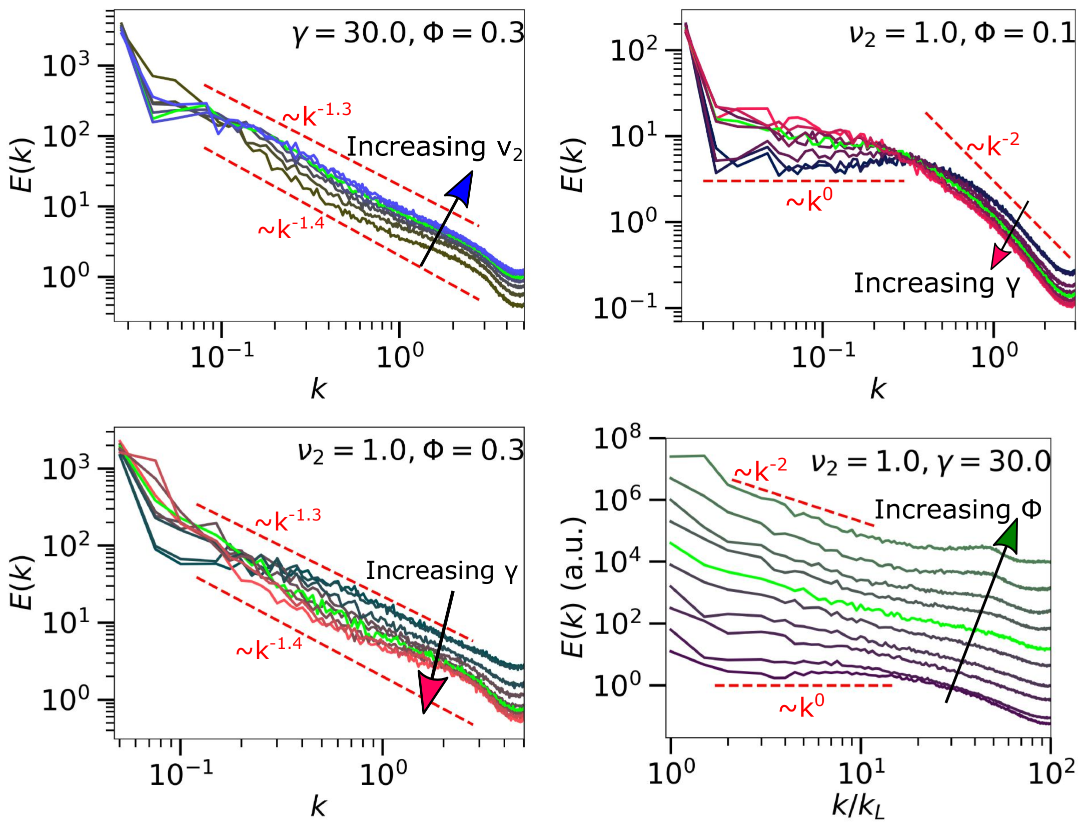

Figure 26: Plots showing the parameter dependence of the energy spectra $E(k)$ as a function of the wavenumber k. ***Upper left:*** Systems of $N = 5000$ particles, area fraction $\Phi = 0.3$ and flow alignment coefficient $\gamma = 30.0$. The other flow alignment coefficient ν_2 is varied in the range $[0.2, 3.0]$, where increasing ν_2 is indicated by increasingly blue graphs. The lime-green graph shows $\nu_2 = 2.0$. For comparison the dotted lines show $\sim k^{-1.3}$ and $\sim k^{-1.4}$ development. ***Upper right:*** Systems with $N = 5000$, $\nu_2 = 1.0$ and $\Phi = 0.3$. The three graphs taking the lowest values of $E(k)$ at low k represent $\gamma = 0.5, \gamma = 1.0$ and $\gamma = 10.0$, the others show $\gamma \in [20, 100]$. The lime-green graph indicates $\gamma = 30.0$, and otherwise increasingly red graphs indicates increasing γ. For comparison k^{-2} and k^0 scaling is plotted. ***Lower left:*** Systems with $N = 1500$, $\nu_2 = 1.0$ and $\Phi = 0.3$. Here the two lowest graphs for small k show the cases of $\gamma = 0.5$ and $\gamma = 1.0$, while the rest show $\gamma \in [5, 100]$. The lime-green graph indicates $\gamma = 30.0$ and the straight lines show $k^{-1.3}$ and $k^{-1.4}$ developments, respectively. ***Lower right:*** Systems with $N = 1500$, $\nu_2 = 1.0$ and $\gamma = 30.0$. The area fraction Φ is evenly distributed in the range $[0.05, 0.50]$ with increasingly green colored graphs indicate higher area fractions. The lime-green line shows $\Phi = 0.3$, and for comparison the straight line show k^0 and k^{-2} scaling. The spectra are plotted as a function of k/k_L in this case, where $k_L = 2\pi/L$, and vertically staggered to make the individual graphs more visible.

with higher ν_2. At large R all these derivatives follow the same trend. These observations confirm that the flocking mechanism makes correlations on a certain scale more dominant, relative to the scales in its vicinity. Thus, the energy spectrum $E(k)$ becomes steeper for k-values below this scale and flatter above, compared to a case where the system does not have such a characteristic length scale.

In the lower left plot of Figure 26 we see that the effect of an increasing γ when $\nu_2 = 1.0$ is very similar to that of decreasing ν_2 when $\gamma = 30.0$ at an area fraction $\Phi = 0.3$. The exceptions are when $\gamma = 0.5$ and $\gamma = 1.0$ where we see that large scale fluctuations are significantly smaller than in the other cases. From the notation we used in Eqs. (30)-(32) we may define a critical length r_c by $A(r_c) = C(r_c)$, where the strength of the aligning and dipolar interactions are equal. Given the reduced units and the r^{-5} decay of the alignment interaction we find that $r_c = \sqrt[3]{\gamma/\nu_2}$. Thus, with $\nu_2 = 1.0$ and $\gamma \leq 1$ this length is shorter than the particle radius. With its rapid decay

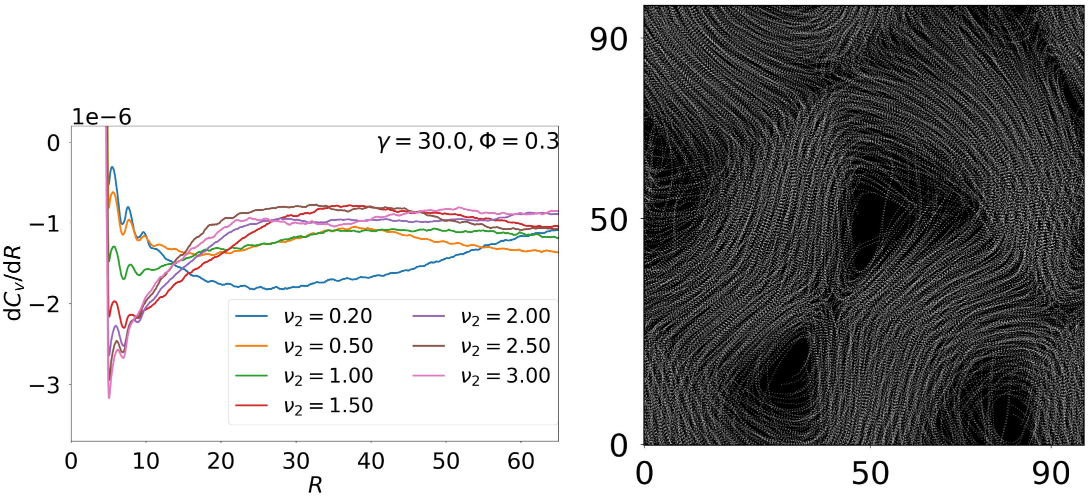

Figure 27: *Right:* Plot of derivatives of the velocity correlation functions C_v with respect to the separation distance R. The graphs represent systems of $N = 1500$ particles with area fraction $\Phi = 0.3$ and flow alignment coefficients $\gamma = 30.0$ and ν_2 as indicated in the plot. The energy spectra of the same system are shown in the upper left plot of Figure 26. *Left:* Streamline plot of system with $N = 1500$ particles, area fraction $\Phi = 0.5$ and flow alignment coefficients $\gamma = 30.0$ and $\nu_2 = 1.0$.

the alignment interaction thus becomes as good as negligible with these γ. This is seen by the fact the the power spectra of $\gamma = 0.5$ and $\gamma = 1.0$ are almost identical. However, already at $\gamma = 5.0$ we see that $E(k)$ rises significantly at small k, and further increment of γ does not seem to alter the spectra to any large degree. With $\gamma = 5.0$ the critical distance $r_c = 1.7$ is still less than a particle diameter. At the characteristic nearest neighbor distance $r = 2.2$ we found in subsection 5.1 the strength of the alignment interaction is about half of the dipolar interaction given $\nu_2 = 1.0, \gamma = 5.0$. However, this is clearly enough to impact the global dynamics of the system.

The upper right plot in Figure 26 shows the same comparison as the lower left, but at an area fraction $\Phi = 0.1$. In this case the graphs representing $\gamma = 0.5$, $\gamma = 1.0$ and $\gamma = 10.0$ show distinct lower values of $E(k)$ than the rest for small k. Thus the lower density means a higher threshold for γ to affect the large-scale fluctuations of the system. Again we see that above this threshold the spectra show very similar behaviour. Compared to the higher density systems we see that the spectra are steeper for large k and flatter for small k. Bearing the discussion on the protuberance in the upper left plot in mind, we know that this indicates a scale at which fluctuations are relatively more dominant than on the surrounding scales. From the flat spectra we observe at low k for the smallest γ we interpret that the rate of change in correlation is the same at all scales which these k represent.

Finally, the lower right plot shows a comparison of the energy spectra at different area fractions Φ with flow alignment coefficients $\nu_2 = 1.0$ and $\gamma = 30.0$. To spectra are vertically staggered and plotted as functions of k/k_L to make the qualitative differences more visible. This plot clearly illustrates that an increasing density leads to steeper energy spectra and therefore relatively more large-scale correlations. From the comparison of the low- and high-density systems in the section above we have seen that an increasing density makes the alignment interaction more dominant, creating long-range correlations within the system. We again emphasize that a steeper spectrum is interpreted as a slower decrease in correlation as the length scale increases. This will then materialize in fluctuations with long wavelengths.

In Figure 27 we have plotted the streamlines of the system with area fraction $\Phi = 0.5$ in the same way that we did for the two systems with lower density in Figure 18 and 23. This clearly illustrates how the increased density leads to long-ranged correlations and global patterns. Compared even to the case of $\Phi = 0.3$ in Figure 18 the global fluctuations are strikingly more dominant in this case. This gives us a good perception on what the increasing steepness of the energy spectra actually tells us about the behaviour of the system. Such fluctuations are reminiscent of observations from ordered state in the Vicsek model [53]. As the alignment term we introduced from the flying XY-model has similar effect as the Vicsek model, one could argue that the same mechanisms are responsible for the fluctuations we observe. However, there is no polar order in the states we are looking at here, and the low density areas appear to be more like vortex centers rather than in between flocks travelling along the same direction. Thus we expect that there are more mechanisms responsible for these fluctuations than just the Vicsek-like interaction.

We have now seen that as long as the flow alignment coefficients γ and ν_2 are within certain ranges that depend on the area fraction Φ, the system appears to exhibit active turbulence with universal scaling at large scales. In the case of $\nu_2 = 2.0$, $\gamma = 30.0$ and $\Phi = 0.3$ we have checked that this is the case. The scaling of the energy spectra $E(k)$ does however also appear to be density-dependent, with an increasing exponent at increasing densities. The question that then rises is what physical mechanisms are responsible for this universal scaling.

The spectra observed by Wensink et. al. [41] in Figure 3 show a distinct peak and a decreasing kinetic energy at large scales. This appears to be a typical result for dry, friction dominated systems with short-range interactions only [45, 85, 98, 99]. This is contrast to the universal scaling observed by Alert et. al. [44] in Figure 4, which is more reminiscent of our results. The fundamental difference between these behaviours is that when you "zoom out" an image of the system by increasing the system size and particle number, you will see that the patterns in these dry systems will become gradually smaller until they cannot be seen. On the contrary, in our system you will see larger structures appear as the system size increases, and therefore an image of say a million particles will display the same patterns as of a hundred thousand. This is of course given that the observed scaling law is actually universal.

It then appears to be the long-range hydrodynamic interactions that are responsible for this universal scaling, compared to dry systems whose interactions are solely short-range. In our model we know that without the alignment interaction alone is capable of creating order on scales well above its own range, and that the dipolar alignment interaction produces disorder on short scales and long-range anti-correlation. Thus the combination of these two interactions evidently facilitates large-scale patterns. As we have seen, if the dipolar alignment interaction dominates the dynamics to much caused by either a small γ or a low density, the energy spectrum becomes flat at large scales. This indicates that dipole interaction alone does not produce any characteristic scale in form of a minima in the velocity correlation function, i.e. no characteristic vortex size. Thus a characteristic length scale in our system indeed owes to the competition between the two alignment interactions. This is also in line with results from Ref. [100]. There it is shown that adding an alignment interaction transforms otherwise stationary patterns into spatiotemporal oscillatory or chaotic ones.

The main difference separating our results from the ones obtained by Alert et. al. is the exponent of the power law on large scales, which they find to be close to 1. We know that a steeper power law implies that fluctuations on large scales become relatively more dominant. Since their macroscopic continuum model is very different from our microscopic particle mode, it is challenging to compare the mechanisms leading to this difference. Yet, we know their model assumes the active fluid to be incompressible. This is clearly a fundamental difference from our system, where we observe large density fluctuations at all densities as we see in e.g. Figure 27. To see how this affects the energy spectra is by no means straightforward, but one can imagine that it is energetically more favourable with long-range correlations if particles can form flocks within the system. By drawing an analogy to statistical physics, we know that formation of domains with different magnetization within a magnet requires energy to create domain walls. If these domains instead are separated by a particle vacuum, such a domain wall energy is not required. Nevertheless, the scale of the density fluctuations we observe in the streamline plots in Figure 18, 23 and 27 indeed appear to be correlated with scale of the correlated flocks in the respective systems. It therefore seems reasonable that the compressibility of the system plays a role in the energy spectra.

Another key difference between the systems is that Alert et. al. use a nematic model, in contrast to our polar system. In nematic systems, chaotic flows appear as a result of active stresses, and a characteristic length arises from competition between this active stress and elastic nematic stress [101]. In our case such a characteristic length must arise from the balance between the two alignment interactions. However, such a length scale appears to be far less distinct in our system. It thus appears that the nematic system to a larger degree facilitates structures at this intrinsic length than our system, but then making the large scale structures relatively less dominant. One could also argue that nematic order is a less strict criterion than polar order, and therefore will produce relatively less correlated structures on large scales. Finally, we note that Alert et. al. adds a local white noise term to their model to account for fluctuations. This might also lead to more local fluctuations and less correlation on larger scales.

As we see, there are a few differences between the model of Alert et. al. and ours that can lead different power law scaling. Most significantly, the assumption of incompressibility and the nematic ordering are in contrast to our system and therefore rationalizes different behaviours. Nevertheless, in both systems non-linear and long-range hydrodynamic interactions play a significant role. Thus, in combination with an ordering mechanism, this appears to be a key factor for the observed scaling of the turbulent behaviour.

6 Conclusion and Outlook

The goal of this work has been to investigate the collective behaviour of a microscopical particle model of an active, polar system with long-range hydrodynamic interactions and a short-ranged alignment interaction. During the progress of the project, particular interest has been caught in whether this model can produce systems that exhibit active turbulence or not, as there appears to be little literature on this specific subject. To facilitate this examination, typical characterization methods from studies of inertial turbulence are introduced and discussed. Most importantly, the energy spectrum $E(k)$. The hydrodynamic interactions between the particles are then introduced on the basis of self-propelling swimmers in a Hele-Shaw cell, and from this the equations of motion are motivated and discussed. Furthermore an alignment interaction from the flying XY-model is presented and incorporated into the model. The studies of the resulting system are focused on the balance between this alignment interaction with strength γ and the alignment along the induced dipolar flows, with an alignment coefficient ν_2.

The main result reported is the observation of active turbulence with universal scaling in the presented model. To the author's knowledge, this has not been demonstrated in particle models of polar systems with long-range, hydrodynamic interactions. To give grounds for this assertion, a system with area fraction $\Phi = 0.3$ and flow alignment coefficients ν_2 and γ is carefully examined. The energy spectrum of this system shows a power law scaling $\sim k^{-\beta}$ with an exponent $\beta \approx 1.3$ on large scales, in contrast to the Kolmogorov scaling with $\beta = 5/3$ in inertial turbulence. The universality of this scaling is verified by simulations of systems with $N = 1500, 5000$ and 15000 particles. From this spectrum we expect to see correlated behaviour of the particles on all scales of the system. Large-scale patterns are confirmed by snapshots of the particle orientations, the stream function $\psi(\boldsymbol{r})$ and a plot of the vorticity field $\omega(\boldsymbol{r})$. Furthermore, we find a non-Gaussian broadening of the normalized probability distribution functions for the velocity increments $\delta v_{\parallel,\perp}(R)$. There is a distinct broadening of these exponential tails as the separation distance R decreases, a hallmark of turbulent behaviour. Finally, we show that there is a transition from a ballistic to a diffusive regime in the time development of the root mean square displacement $\langle\lambda\rangle$, in line with results on other turbulent systems. Connecting these results we conclude that the system exhibits active turbulence.

To illustrate the driving mechanisms of the turbulent behaviour in the system, we compare it with another system with lower area fraction $\Phi = 0.1$ and flow alignment coefficients $\gamma = 30.0$ and $\nu_2 = 1.0$. In this system there is clearly less large-scale patterns, which is supported by the almost flat energy spectrum at large k. On small scales there is also here velocity fluctuations yielding non-Gaussian probability distribution functions for $\delta v_{\parallel,\perp}$, and the vorticity plot indicates at least the same amount of activity. We attribute these differences to the fact higher density appears to make the alignment interaction involving γ relatively more dominant. This leads to highly correlated behaviour on lengths well above the range of this interaction which we observe as flocking in the system. The flocking also appears to strengthen the dipole interaction on large scales.

Finally, the impact from the three key parameters γ, ν_2 and Φ is studied. Plots of the energy spectra where these are varied show that as long as the alignment coefficients γ and ν_2 are within a certain range given by the density, they do not have any major impact on the scaling of $E(k)$. However, at $\Phi = 0.3$ we see that large γ compared to ν_2 leads to a protuberance at large k which we relate to a characteristic flocking size. An increasing area fraction Φ indeed leads to a steeper scaling of the energy spectra. At low area fractions the spectra are more or less flat, while for the highest simulated case $\Phi = 0.5$ the scaling is steeper than k^{-2} at low k. The interpretation of this is that at high densities the large-scale fluctuations become relatively more dominant compared to the ones at smaller scales. The alignment interaction causes correlations well beyond its own range and the motion of the particles throughout the whole system becomes connected to a much larger extent at high densities.

To put our results into context, we compare them with observations of active turbulence in other systems with varying similarity to ours. In general we find that dry systems with short-range interactions typically exhibit a peak of $E(k)$ corresponding to a characteristic length and decaying spectra at large scales. This is qualitatively different from our results, where the spectra increase up to the largest scales. A specific comparison is performed with a continuum model of an active, nematic system is showing universal k^{-1}-scaling at small k. The difference in scaling shows that fluctuations on large scales are more dominant in the polar system studied here than in the nematic one. A likely cause of this is the possibility of density fluctuations in the particle model we study, which at relative high densities favours formation of large-scale coherent flocks compared to an incompressible system. In addition the difference between polar and nematic alignment, and the lack of a noise term in our system are factors that can influence the scaling.

To conclude we state that the active turbulence we observe in this model is a result of the balance between the short-range alignment interaction and the long-range hydrodynamic dipole interaction. The alignment interaction generates coherent flocks larger than its own range given a high enough density. The non-linear dipolar flow interaction in itself causes chaos on all scales, but with the flocking its long-range effect becomes amplified and more ordered. Thus, fluctuations are present on all scales of the system leading to a universal scaling of the energy spectrum.

6.1 Outlook

The results of this work should contribute to a better understanding of active turbulence in general, not only for the system studied here. The fact that density fluctuations appear to have an impact on the scaling of the energy spectrum could be a generic property for active turbulence in microscopical particle models. It would therefore be interesting to see if similar behaviour can arise in other such models. For example could the model we have investigated here modified by replacing the polar alignment interaction from the XY-model with a nematic alignment interaction. Another modification could be to add a noise term. In these report we have focused on the effects of the pure hydrodynamic interactions. With this clarified it is natural to investigate how statistical noise affects this results, as fluctuations are indeed relevant in real life systems.

Within the given model, a natural continuation would be to seek more robust results for the largest systems simulated here with $N = 15000$ particles. We have seen that systems with 1500 and 5000 particles display very similar behaviour, but a confirmation that this is also the case for larger systems would be necessary to give a definitive conclusion on the scaling behaviour. Furthermore, it would be interesting to investigate the phase space $(\nu_1, \nu_2, \gamma, \Phi)$ further, to find the boundaries of the turbulent regime and gain more insight into its underlying mechanisms. For simplicity the ν_1-term has not been considered here, but this could naturally also affect the turbulent behaviour as we know it is capable of producing global order. Finally, we know that the boundary conditions have a strong impact on the behaviour of the system. Therefore, it would also be of interest to see how e.g. circular confinement would affect the results we have found here.

Bibliography

[1] M. Själander, M. Jahre, G. Tufte and N. Reissmann, *EPIC: an energy-efficient, high-performance GPGPU computing research infrastructure*, 2019.

[2] S. Ramaswamy, 'The mechanics and statistics of active matter', Annual Review of Condensed Matter Physics **1**, 10.1146/annurev-conmatphys-070909-104101 (2010).

[3] T. Armstrong-Sly, https://secure.flickr.com/photos/tonyarmstrong/5381370808/.

[4] S. Tuckett, https://www.simontuckett.com/Illustration.

[5] M. Bianchetti, https://unsplash.com/photos/ZuV4bPalclY.

[6] D. Saintillan and M. J. Shelley, 'Active suspensions and their nonlinear models', Comptes Rendus Physique **14**, 10.1016/j.crhy.2013.04.001 (2013).

[7] G. Popkin, *The physics of life*, tech. rep. 7584 (2016), https://www.nature.com/news/the-physics-of-life-1.19105.

[8] A. Bricard, J. B. Caussin, D. Das, C. Savoie, V. Chikkadi, K. Shitara, O. Chepizhko, F. Peruani, D. Saintillan and D. Bartolo, 'Emergent vortices in populations of colloidal rollers', Nature Communications **6**, 10.1038/ncomms8470 (2015).

[9] T. Brotto, J. B. Caussin, E. Lauga and D. Bartolo, 'Hydrodynamics of confined active fluids', Physical Review Letters **110**, 10.1103/PhysRevLett.110.038101 (2013).

[10] M. C. Marchetti, J. F. Joanny, S. Ramaswamy, T. B. Liverpool, J. Prost, M. Rao and R. A. Simha, 'Hydrodynamics of soft active matter', Reviews of Modern Physics **85**, 10.1103/RevModPhys.85.1143 (2013).

[11] J. J. Monaghan and J. B. Kajtar, 'Leonardo da Vinci's turbulent tank in two dimensions', European Journal of Mechanics, B/Fluids **44**, 10.1016/j.euromechflu.2013.09.005 (2014).

[12] R. P. Feynman, R. B. Leighton, M. Sands and E. M. Hafner, 'The Feynman Lectures on Physics; Vol. I', American Journal of Physics **33**, 10.1119/1.1972241 (1965).

[13] I. Eames and J. B. Flor, *New developments in understanding interfacial processes in turbulent flows*, 2011.

[14] V. L'vov and I. Procaccia, 'Hydrodynamic turbulence: a 19th century problem with a challenge for the 21st century', in *Turbulence modeling and vortex dynamics* (2008).

[15] L. Seuront, F. Schmitt, Y. Lagadeuc, D. Schertzer, S. Lovejoy and S. Frontier, 'Multifractal analysis of phytoplankton biomass and temperature in the ocean', Geophysical Research Letters **23**, 10.1029/96GL03473 (1996).

[16] F. Zöllner, *Leonardo da Vinci, 1452-1519: sketches and drawings* (2004).

[17] F. H. Champagne, 'The fine-scale structure of the turbulent velocity field', Journal of Fluid Mechanics **86**, 10.1017/S0022112078001019 (1978).

[18] N. K. Johnson and L. F. Richardson, 'Weather Prediction by Numerical Process', The Mathematical Gazette **11**, 10.2307/3603284 (1922).

[19] B. Ryden, *Lecture notes in astronomy 825 - radiative gas dynamics, chapter 7* (The Ohio State University, Department of Astronomy, 2011), http://www.astronomy.ohio-state.edu/~ryden/ast825/.

[20] A. N. Kolmogorov, 'The local structure of turbulence in incompressible viscous fluid for very large Reynolds numbers', Proceedings of the Royal Society of London. Series A: Mathematical and Physical Sciences **434**, 10.1098/rspa.1991.0075 (1991).

[21] A. N. Kolmogorov, Doklady Akademii Nauk SSSR **32** (1941).

[22] A. N. Kolmogorov, Doklady Akademii Nauk SSSR **30** (1941).

[23] A. N. Kolmogorov, Doklady Akademii Nauk SSSR **31** (1941).

[24] U. Frisch, *Turbulence, the Legacy of A. N. Kolmogorov* (Cambridge University Press, 1995).

[25] G. L. Eyink and K. R. Sreenivasan, 'Onsager and the theory of hydrodynamic turbulence', Reviews of Modern Physics **78**, 10.1103/RevModPhys.78.87 (2006).

[26] L. Onsager, Physical Review **68** (1945).

[27] L. Onsager, Nuovo Cimento, Suppl. **6** (1949).

[28] Z. S. She, E. Jackson and S. A. Orszag, 'Scale-dependent intermittency and coherence in turbulence', Journal of Scientific Computing **3**, 10.1007/BF01065179 (1988).

[29] A. Vincent and M. Meneguzzi, 'The spatial structure and statistical properties of homogeneous turbulence', Journal of Fluid Mechanics **225**, 10.1017/S0022112091001957 (1991).

[30] J. Mathieu and J. Scott, *An Introduction to Turbulent Flow* (Cambridge University Press, 2000).

[31] G. Boffetta and R. E. Ecke, 'Two-Dimensional Turbulence', Annual Review of Fluid Mechanics **44**, 10.1146/annurev-fluid-120710-101240 (2012).

[32] T. Riste, *Fluctuations, Instabilities, and Phase Transitions* (1975).

[33] A. Groisman and V. Stelnberg, 'Elastic turbulence in a polymer solution flow', Nature **405**, 10.1038/35011019 (2000).

[34] V. Steinberg, 'Elastic Turbulence: An Experimental View on Inertialess Random Flow', Annual Review of Fluid Mechanics **53**, 10.1146/annurev-fluid-010719-060129 (2021).

[35] F. Radjai and S. Roux, 'Turbulentlike fluctuations in quasistatic flow of granular media', Physical Review Letters **89**, 10.1103/PhysRevLett.89.064302 (2002).

[36] J. Dunkel, S. Heidenreich, K. Drescher, H. H. Wensink, M. Bär and R. E. Goldstein, 'Fluid dynamics of bacterial turbulence', Physical Review Letters **110**, 10.1103/PhysRevLett.110.228102 (2013).

[37] C. Dombrowski, L. Cisneros, S. Chatkaew, R. E. Goldstein and J. O. Kessler, 'Self-concentration and large-scale coherence in bacterial dynamics', Physical Review Letters **93**, 10.1103/PhysRevLett.93.098103 (2004).

[38] A. Sokolov, I. S. Aranson, J. O. Kessler and R. E. Goldstein, 'Concentration dependence of the collective dynamics of swimming bacteria', Physical Review Letters **98**, 10.1103/PhysRevLett.98.158102 (2007).

[39] H. P. Zhang, A. Be'er, E. L. Florin and H. L. Swinney, 'Collective motion and density fluctuations in bacterial colonies', Proceedings of the National Academy of Sciences of the United States of America **107**, 10.1073/pnas.1001651107 (2010).

[40] V. Schaller, C. Weber, C. Semmrich, E. Frey and A. R. Bausch, 'Polar patterns of driven filaments', Nature **467**, 10.1038/nature09312 (2010).

[41] H. H. Wensink, J. Dunkel, S. Heidenreich, K. Drescher, R. E. Goldstein, H. Löwen and J. M. Yeomans, 'Meso-scale turbulence in living fluids', Proceedings of the National Academy of Sciences of the United States of America **109**, 10.1073/pnas.1202032109 (2012).

[42] A. Sokolov and I. S. Aranson, 'Physical properties of collective motion in suspensions of bacteria', Physical Review Letters **109**, 10.1103/PhysRevLett.109.248109 (2012).

[43] Y. Sumino, K. H. Nagai, Y. Shitaka, D. Tanaka, K. Yoshikawa, H. Chaté and K. Oiwa, 'Large-scale vortex lattice emerging from collectively moving microtubules', Nature **483**, 10.1038/nature10874 (2012).

[44] R. Alert, J. F. Joanny and J. Casademunt, 'Universal scaling of active nematic turbulence', Nature Physics **16**, 10.1038/s41567-020-0854-4 (2020).

[45] R. Alert, J. Casademunt and J.-F. Joanny, *Active turbulence*, 2021, https://arxiv.org/abs/2104.02122.

[46] D. C. Champeney, *A handbook of Fourier theorems* (Cambridge University Press, 1987).

[47] G. B. Arfken, H. J. Weber and F. E. Harris, *Mathematical Methods for Physicists, Chapter 20* (San Diego: Elsevier Science & Technology, 2011), https://www.sciencedirect.com/book/9780123846549/mathematical-methods-for-physicists.

[48] D. Nishiguchi, 'Active turbulence', in *Order and fluctuations in collective dynamics of swimming bacteria: experimental exploration of active matter physics* (Springer Singapore, Singapore, 2020), pp. 85–96, https://doi.org/10.1007/978-981-32-9998-6_4.

[49] S. Mukherjee, R. K. Singh, M. James and S. S. Ray, *Anomalous diffusion and lévy walks distinguish active turbulence*, 2021, https://arxiv.org/abs/2105.07872.

[50] J. Toner, Y. Tu and S. Ramaswamy, *Hydrodynamics and phases of flocks*, 2005.

[51] J. Toner and Y. Tu, 'Flocks, herds, and schools: A quantitative theory of flocking', Physical Review E - Statistical Physics, Plasmas, Fluids, and Related Interdisciplinary Topics **58**, 10.1103/PhysRevE.58.4828 (1998).

[52] A. U. Oza, S. Heidenreich and J. Dunkel, 'Generalized Swift-Hohenberg models for dense active suspensions', European Physical Journal E **39**, 10.1140/epje/i2016-16097-2 (2016).

[53] T. Vicsek, A. Czirk, E. Ben-Jacob, I. Cohen and O. Shochet, 'Novel type of phase transition in a system of self-driven particles', Physical Review Letters **75**, 10.1103/PhysRevLett.75.1226 (1995).

[54] H. Chaté, F. Ginelli, G. Grégoire, F. Peruani and F. Raynaud, 'Modeling collective motion: Variations on the Vicsek model', European Physical Journal B **64**, 10.1140/epjb/e2008-00275-9 (2008).

[55] H. Chaté, F. Ginelli and R. Montagne, 'Simple model for active nematics: Quasi-long-range order and giant fluctuations', Physical Review Letters **96**, 10.1103/PhysRevLett.96.180602 (2006).

[56] G. Grégoire, H. Chaté and Y. Tu, 'Moving and staying together without a leader', Physica D: Nonlinear Phenomena **181**, 10.1016/S0167-2789(03)00102-7 (2003).

[57] M. Aldana, V. Dossetti, C. Huepe, V. M. Kenkre and H. Larralde, 'Phase transitions in systems of self-propelled agents and related network models', Physical Review Letters **98**, 10.1103/PhysRevLett.98.095702 (2007).

[58] F. Ginelli and H. Chaté, 'Relevance of metric-free interactions in flocking phenomena', Physical Review Letters **105**, 10.1103/PhysRevLett.105.168103 (2010).

[59] M. Nagy, I. Daruka and T. Vicsek, 'New aspects of the continuous phase transition in the scalar noise model (SNM) of collective motion', Physica A: Statistical Mechanics and its Applications **373**, 10.1016/j.physa.2006.05.035 (2007).

[60] F. D. Farrell, M. C. Marchetti, D. Marenduzzo and J. Tailleur, 'Pattern formation in self-propelled particles with density-dependent motility', Physical Review Letters **108**, 10.1103/PhysRevLett.108.248101 (2012).

[61] A. Bricard, J. B. Caussin, N. Desreumaux, O. Dauchot and D. Bartolo, 'Emergence of macroscopic directed motion in populations of motile colloids', Nature **503**, 10.1038/nature12673 (2013).

[62] M. E. Cates and J. Tailleur, 'Motility-Induced Phase Separation', Annual Review of Condensed Matter Physics **6**, 10.1146/annurev-conmatphys-031214-014710 (2015).

[63] L. Caprini, U. Marini Bettolo Marconi and A. Puglisi, 'Spontaneous Velocity Alignment in Motility-Induced Phase Separation', Physical Review Letters **124**, 10.1103/PhysRevLett.124.078001 (2020).

[64] M. R. Shaebani, A. Wysocki, R. G. Winkler, G. Gompper and H. Rieger, 'Computational models for active matter', Nature Reviews Physics **2**, 10.1038/s42254-020-0152-1 (2020).

[65] E. Lushi, H. Wioland and R. E. Goldstein, 'Fluid flows created by swimming bacteria drive self-organization in confined suspensions', Proceedings of the National Academy of Sciences of the United States of America **111**, 10.1073/pnas.1405698111 (2014).

[66] E. M. Purcell, 'Life at low Reynolds number', American Journal of Physics **45**, 10.1119/1.10903 (1977).

[67] M. B. Miller and B. L. Bassler, 'Quorum Sensing in Bacteria', Annual Review of Microbiology **55**, 165–199 (2001), http://www.annualreviews.org/doi/10.1146/annurev.micro.55.1.165.

[68] A. C. Edmunds, L. F. Castiblanco, G. W. Sundin and C. M. Waters, 'Cyclic Di-GMP modulates the disease progression of erwinia amylovora', Journal of Bacteriology **195**, 10.1128/JB.02068-12 (2013).

[69] A. Cheng Hou Tsang and E. Kanso, 'Flagella-induced transitions in the collective behavior of confined microswimmers', Physical Review E - Statistical, Nonlinear, and Soft Matter Physics **90**, 10.1103/PhysRevE.90.021001 (2014).

[70] S. Bhattacharya, J. Bławzdziewicz and E. Wajnryb, 'Far-field approximation for hydrodynamic interactions in parallel-wall geometry', Journal of Computational Physics **212**, 10.1016/j.jcp.2005.07.015 (2006).

[71] A. Lefauve and D. Saintillan, 'Globally aligned states and hydrodynamic traffic jams in confined suspensions of active asymmetric particles', Physical Review E - Statistical, Nonlinear, and Soft Matter Physics **89**, 10.1103/PhysRevE.89.021002 (2014).

[72] N. Liron and S. Mochon, 'Stokes flow for a stokeslet between two parallel flat plates', Journal of Engineering Mathematics **10**, 10.1007/BF01535565 (1976).

[73] T. Beatus, R. H. Bar-Ziv and T. Tlusty, 'The physics of 2D microfluidic droplet ensembles', Physics Reports **516**, 10.1016/j.physrep.2012.02.003 (2012).

[74] W. C. Poon, 'From Clarkia to escherichia and janus: The physics of natural and synthetic active colloids', in Proceedings of the international school of physics "enrico fermi", Vol. 184 (2012).

[75] A. C. H. Tsang and E. Kanso, 'Circularly confined microswimmers exhibit multiple global patterns', Physical Review E - Statistical, Nonlinear, and Soft Matter Physics **91**, 10.1103/PhysRevE.91.043008 (2015).

[76] G. P. Alexander and J. M. Yeomans, 'Dumb-bell swimmers', EPL **83**, 10.1209/0295-5075/83/34006 (2008).

[77] G. B. Jeffery and L. N. G. Filon, 'The motion of ellipsoidal particles immersed in a viscous fluid', Proceedings of the Royal Society of London. Series A, Containing Papers of a Mathematical and Physical Character **102**, 161–179 (1922), https://royalsocietypublishing.org/doi/10.1098/rspa.1922.0078.

[78] K. T. Wu, J. B. Hishamunda, D. T. Chen, S. J. DeCamp, Y. W. Chang, A. Fernández-Nieves, S. Fraden and Z. Dogic, 'Transition from turbulent to coherent flows in confined three-dimensional active fluids', Science **355**, 10.1126/science.aal1979 (2017).

[79] A. Bricard, J. B. Caussin, N. Desreumaux, O. Dauchot and D. Bartolo, *Supplementary information, Emergence of macroscopic directed motion in populations of motile colloids*, tech. rep. (2013), https://www.nature.com/articles/nature12673.

[80] F. M. White, *Fluid Mechanics, Sixth Edition: Chapter 8* (McGraw-Hill, 2008).

[81] J. D. Weeks, D. Chandler and H. C. Andersen, 'Role of repulsive forces in determining the equilibrium structure of simple liquids', The Journal of Chemical Physics **54**, 10.1063/1.1674820 (1971).

[82] K. E. Andreassen, *Active matter states of self-propelled dipolar particles*, 2019, https://ntnuopen.ntnu.no/ntnu-xmlui/handle/11250/2634437.

[83] A. Lefauve and D. Saintillan, *Supplemental Material: Discrete Particle Simulation Method*, tech. rep. (2014), https://journals.aps.org/pre/abstract/10.1103/PhysRevE.89.021002.

[84] M. Aldana, H. Larralde and B. Vazquez, 'On the emergence of collective order in swarming systems: a recent debate', International Journal of Modern Physics B **23**, 3661–3685 (2009), https://doi.org/10.1142/S0217979209053552.

[85] R. Großmann, P. Romanczuk, M. Bär and L. Schimansky-Geier, 'Vortex arrays and meso-scale turbulence of self-propelled particles', Physical Review Letters **113**, 10.1103/PhysRevLett.113.258104 (2014).

[86] K. H. Nagai, 'Collective motion of rod-shaped self-propelled particles through collision', Biophysics and Physicobiology **15**, 10.2142/biophysico.15.0{_}51 (2018).

[87] B. Guinard and A. Korman, 'Intermittent inverse-square Lévy walks are optimal for finding targets of all sizes', Science Advances **7**, 10.1126/sciadv.abe8211 (2021).

[88] D. W. Sims, E. J. Southall, N. E. Humphries, G. C. Hays, C. J. Bradshaw, J. W. Pitchford, A. James, M. Z. Ahmed, A. S. Brierley, M. A. Hindell, D. Morritt, M. K. Musyl, D. Righton, E. L. Shepard, V. J. Wearmouth, R. P. Wilson, M. J. Witt and J. D. Metcalfe, 'Scaling laws of marine predator search behaviour', Nature **451**, 10.1038/nature06518 (2008).

[89] T. H. Harris, E. J. Banigan, D. A. Christian, C. Konradt, E. D. Wojno, K. Norose, E. H. Wilson, B. John, W. Weninger, A. D. Luster, A. J. Liu and C. A. Hunter, ‘Generalized Lévy walks and the role of chemokines in migration of effector CD8 + T cells’, Nature **486**, 10.1038/nature11098 (2012).

[90] S. Wolf, E. Nicholls, A. M. Reynolds, P. Wells, K. S. Lim, R. J. Paxton and J. L. Osborne, ‘Optimal search patterns in honeybee orientation flights are robust against emerging infectious diseases’, Scientific Reports **6**, 10.1038/srep32612 (2016).

[91] H. Kellay and W. I. Goldburg, ‘Two-dimensional turbulence: A review of some recent experiments’, Reports on Progress in Physics **65**, 10.1088/0034-4885/65/5/204 (2002).

[92] H. H. Wensink and H. Löwen, ‘Emergent states in dense systems of active rods: From swarming to turbulence’, Journal of Physics Condensed Matter **24**, 10.1088/0953-8984/24/46/464130 (2012).

[93] J. C. Maxwell, ‘ V. Illustrations of the dynamical theory of gases. —Part I. On the motions and collisions of perfectly elastic spheres ’, The London, Edinburgh, and Dublin Philosophical Magazine and Journal of Science **19**, 10.1080/14786446008642818 (1860).

[94] C. P. Sanjay and A. Joy, ‘Friction scaling laws for transport in active turbulence’, Physical Review Fluids **5**, 10.1103/PhysRevFluids.5.024302 (2020).

[95] X. L. Wu and A. Libchaber, ‘Particle diffusion in a quasi-two-dimensional bacterial bath’, Physical Review Letters **84**, 10.1103/PhysRevLett.84.3017 (2000).

[96] L. Giomi, ‘Geometry and topology of Turbulence in active nematics’, Physical Review X **5**, 10.1103/PhysRevX.5.031003 (2015).

[97] L. N. Carenza, L. Biferale and G. Gonnella, ‘Multiscale control of active emulsion dynamics’, Physical Review Fluids **5**, 10.1103/PhysRevFluids.5.011302 (2020).

[98] V. Bratanov, F. Jenko and E. Frey, ‘New class of turbulence in active fluids’, Proceedings of the National Academy of Sciences of the United States of America **112**, 10.1073/pnas.1509304112 (2015).

[99] R. C. Coelho, N. A. Araújo and M. M. Telo da Gama, ‘Propagation of active nematic-isotropic interfaces on substrates’, Soft Matter **16**, 10.1039/c9sm02306b (2020).

[100] F. Bonelli, G. Gonnella, A. Tiribocchi and D. Marenduzzo, ‘Spontaneous flow in polar active fluids: the effect of a phenomenological self propulsion-like term’, European Physical Journal E **39**, 10.1140/epje/i2016-16001-2 (2016).

[101] S. P. Thampi and J. M. Yeomans, ‘Active turbulence in active nematics’, 10.1140/epjst/e2015-50324-3 (2016), http://arxiv.org/abs/1605.00808%20http://dx.doi.org/10.1140/epjst/e2015-50324-3.

[102] S. Tülü, ‘Vortex dynamics in domains with boundaries’ (2011), http://library.iyte.edu.tr/tezler/doktora/matematik/T000958.pdf.

Appendix

A Circular domain with hydrodynamic image dipoles

subsectionAppendix A The alternative to the periodic boundary conditions is to specify the border of the domain with belonging boundary conditions. As Tsang and Kanso we will do this for a circular domain [75]. Here to do not take the γ-term into account. First, we model the interaction between the swimmers and the boundary walls by

$$V_{\mathrm{bound}}(z'_n) = -\frac{\epsilon}{v_s}\left(\frac{1}{|d|}\right)^{13} \frac{\overline{z}'_n}{|z'_n|} \tag{54}$$

similar to the Lennard-Jones interactions in Eq. (44). With a radius R of the circular domain, $d = (R/r_0 - |z'|)\mathrm{e}^{\mathrm{i}\theta}$ is the shortest vector between a swimmer at $z = |z|\mathrm{e}^{\mathrm{i}\theta}$ and the boundary. This interaction is enough to confine the swimmers within the circular domain, but it does not account for the hydrodynamic effects the confinement. Thus, if we only applied this, we would describe a situation where the fluid flows unaffected through the boundary while the swimmers would be confined by e.g. an electric potential or similar. To take the boundary into account for the fluid flow as well, we will use the Milne-Thomson circle theorem [102]. This is an analog to the method of image charges to model the electric potential in electrostatics. In effect we simply add a swimmer outside the boundary for each swimmer inside to ensure no fluid flow across the boundary. As we saw in relation to Eq. (36), the complex stream function induced by a swimmer at z_0 is $\phi(z) = \frac{v_s\sigma}{2\pi}\mathrm{e}^{\mathrm{i}\alpha}/(z - z_0)$. The Milne-Thomson circle theorem says that the modified stream function $\phi^{\mathrm{circ}}(z) = \phi(z) + \overline{\phi(R^2/\overline{z})}$ while have zero imaginary part at $|z| = R$, which is equivalent to circular boundary of radius R. The motion of a swimmer a swimmer n is then given by

$$\frac{\mathrm{d}\overline{z'_n}}{\mathrm{d}t'} = \mathrm{e}^{-\mathrm{i}\alpha_n} + \mu \sum_{i\neq n}^{N} \frac{\mathrm{e}^{\mathrm{i}\alpha_i}}{(z'_n - z'_i)^2} - \mu \sum_{i=1}^{N} \frac{\mathrm{e}^{-\mathrm{i}\alpha_i}(R^2/\overline{z}'^2_i)}{(z'_n - R^2/\overline{z}'_i)^2} + V'(z'_n) + V_{\mathrm{bound}}(z'_n), \tag{55a}$$

$$\begin{aligned}\frac{\mathrm{d}\alpha_n}{\mathrm{d}t'} =& \mathrm{Re}\left[\nu_1 2\mathrm{i}\mathrm{e}^{2\mathrm{i}\alpha_n}\left(\sum_{i\neq n}^{N} -\frac{\mathrm{e}^{\mathrm{i}\alpha_i}}{(z'_n - z'_i)^3} + \sum_{i=1}^{N} \frac{\mathrm{e}^{-\mathrm{i}\alpha_i}(R^2/\overline{z}'^2_i)}{(z'_n - R^2/\overline{z}'_i)^3}\right)\right] \\ &+ \mathrm{Re}\left[\nu_2 \mathrm{i}\mathrm{e}^{\mathrm{i}\alpha_n}\left(\sum_{i\neq n}^{N} \frac{\mathrm{e}^{\mathrm{i}\alpha_i}}{(z'_n - z'_i)^2} - \sum_{i=1}^{N} \frac{\mathrm{e}^{-\mathrm{i}\alpha_i}(R^2/\overline{z}'^2_i)}{(z'_n - R^2/\overline{z}'_i)^2}\right)\right]\end{aligned} \tag{55b}$$

in a circular confinement if we let $R \to R/r_0$. Again we emphasize that this is a reproduction of the method of Tsang and Kanso [75]. Note that for each of the three coefficients μ, ν_1, ν_2 a new term has been added compared to Eqs. (43a) and (43b). These terms effectively describe a swimmer positioned at $R^2/\overline{z}'_i$ with orientation $\pi - \alpha_i$.

In Figure 28 we see three examples of collective behaviours in a system confined by a circular border. To the left we have a clustering behaviour where $\nu_2 = -1$, in the middle a swirling behaviour where $\nu_2 = 3.0$ and to the right an ordered circular motion where $\nu_2 = 0.0$. In all cases $\nu_1 = 0.3$.

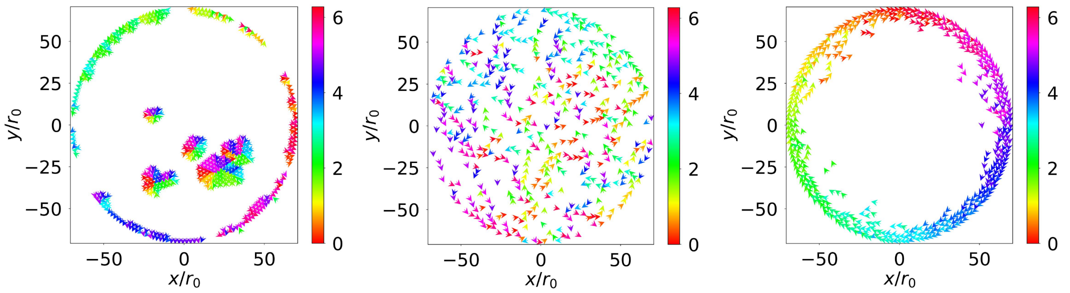

Figure 28: Collective behaviours of system in circular confinement.